2010

Modeling thermal phenomena and searching for new thermally induced monitor signals in large sale gravitational wave detectors

Rupal Shashikant Amin
Louisiana State University and Agricultural and Mechanical College

MODELING THERMAL PHENOMENA AND SEARCHING FOR NEW THERMALLY INDUCED MONITOR SIGNALS IN LARGE SCALE GRAVITATIONAL WAVE DETECTORS

A Dissertation

Submitted to the Graduate Faculty of the
Louisiana State University and
Agricultural and Mechanical College
in partial fulfillment of the
requirements for the degree of
Doctor of Philosophy

in

The Department of Physics and Astronomy

By
Rupal Amin
B.S., Florida Institute of Technology, 1999
M.S., University of Florida, 2002
May 2010

To my

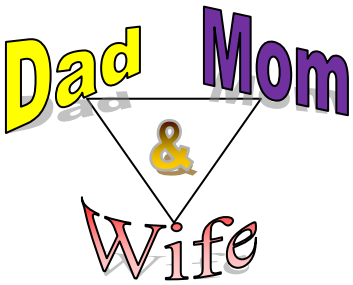

Acknowledgements

This is perhaps the most awkward part of a thesis. There are so many people who you want to thank and others who you would like to erase from the timeline. Perhaps the latter comment was a bit extreme.

First, I would like to thank my parents and my wife's parents and of course my wife for helping me pursue a few of my interests. I would also like to thank my huge family who have been waiting patiently even though they do not understand the gravity of what I do. Next in line would be a couple of people I am glad I met so long ago. These two guys know how to get me angry and pat me on the back at the same time. They are my advisor Joseph Giaime and his former advisor Rai Weiss. I have always had multiple advisors before. In undergrad, I had the Honorable Ryan Raffalle, Hamid Rassoul, and Mark Moldwin. In my master's program, I had David Tanner and David Reitze. But Joe and Rai, geez, these two gave me a mixture of feelings. Either way, I am grateful to have met them. I was just too bad that I got to meet them so late in my graduate career.

Of course there is the humble TCS team, starting with Honorable Phil Willems. Whoever said people from Caltech were stuffy and conceited never met Phil. He has been one of the nicest research scientists I have known and one of the few who kept tabs on me when Joe was busy administrating LIGO Livingston. Aidan Brooks. Hmmm? Virginio Sannabelle and Mohana? Oh, boy. Thanks for all the help you given with the electronics. Carl Adams and Chris Guido, thanks for picking up the loose ends when I had to start graduating. Cheryl and Danny, I am glad to have known you even if it was only through the weekly telecons. Cheryl, you have a terrific sense of humor. I hope it starts a worldwide plague. As for Mike Smith and Dave Ottaway, I really ought to take you both out and slap you one. The tables we inherited gave Aidan, Carl, Cheryl, Danny, and I no end of back aches. I hope you both success.

As for the distinguished technical crew of Livingston, you know who you are. Thanks. Thanks for all the support, putting up with me, the talks about nothing, your faith or lack thereof in me. I am glad that none of you guys had a frown when I walked into the control room or your offices. (Gary, Harry, Rich, Doug, Willie, Jeremy, Ericka, Dan, Danny, Joe, Radar, Tom, Rus, Bonnie, Allen, Dwayne, Shannon, Igor, Kinsel, Nolting, Amber, Derrick, Mike)

As for Hiro Yamamoto, Brian O'Reilly, Rich Abbott, Gregg Harry, Dave Ottaway, Dave Hosken, Rich Mittleman, Fritschel, Daniel Sigg, Lisa, Keith, Peter King, Andreas Freise, Josh S., and Jan Harms, I think I owe you guys a coffee or a beer. You always threw me a hand. Even if it was a naïve question I asked or ran you beyond your knowledge limits. I hope I can help you guys out as many times as you have helped me.

For the professors at LSU, Gonzalez, O'Connell, Dowling, Chan (yes, Chan), Johnson, I render a most sincere thank you. Gonzalez—the perpetually smily professor, O'Connell—if I had not entered experiment, you might have been the next choice, Dowling—looney, goodness smart, taught me all about "proof by intimidation", Chan—a rare breed, Johnson—full of questions, he made me think. This is possibly the second tightest and friendliest department I have seen. Geaux Tigers.

To my classmates and co-misery mates [Chad, Jake, Jeff, Andy, Ryan], thanks for sticking around.

To the others I may have forgotten a simple thank you.

Table of Contents

Abbreviations

TCS	Thermal Compensation System
ACIGA	Australian Consortium for Interferometric Gravitational-wave Astronomy
AM	Amplitude Modulation
AR	Anti-reflective
ASC	Angular Sensing and Control
BS	Beamsplitter
BSC	Beam Splitter Chamber
CO	Carbon Monoxide
CO_2	Carbon Dioxide
EGO	European Gravitational-wave Observatory
EOM	Electro-Optic Modulator
ETM(x,y)	End Test Mass (LIGO arm retro-reflector) for x or y arm
EX (EY)	End station on X(Y)-arm
FI	Faraday Isolator
FEA	Finite Element Analysis (used interchangeably with FEM)
FEM	Finite Element Method/Model
FINESSE	Frequency domain INterferomEter Simulation SoftwarE
FP	Fabry-Perot cavity
GEO	German-English Observatory (also British-German Observatory)
GW	Gravitational Waves
HAM	Horizontal Access Module
HG	Hermite-Gauss (typically refers to a rectangular symmetric basis)
HR	Highly Reflective
IOO	Input/Output Optics
ISC	Instrument Sensing and Control
ITM(x,y)	Input Test Mass (LIGO 4 km arm input coupler) for x or y arm
LG	Laguerre-Gauss (typically refers to a circularly symmetric basis)
LHO	LIGO Hanford Observatory
LIGO	Laser Interferometer Gravitational-wave Observatory
LLO	LIGO Livingston Observatory
LSC	Length Sensing and Control
LVC	LIGO Virgo Science Collaboration
LVEA	Large Vacuum Enclosure Area
MC	Mode Cleaner
Nd:YAG	Neodymium Yttrium Aluminum Garnet [lasing crystal; also used to acknowledge the LIGO main laser light]
ODE	Ordinary Differential Equation
OL	Optical Lever
OPL	Optical Path Length
OSA	Optical Spectrum Analyzer
OSEM	optical (shadow) sensor/electro-magnet
PDE	Partial Differential Equation
PM	Phase Modulation
PMC	Pre-Mode Cleaner
PRC	Power Recycling Cavity
PRM	Power-Recycled Michelson
QPD	Quadrant Photodiode
RF	Radio Frequency (typically > 50 kilohertz)
RM	Recycling Mirror

SiO_2	Silicon dioxide, fused silica, fused quartz
$Ta_2 O_5$	T antalum Pentoxide, the dielectric mirror material used for LIGO HR coatings
TAMA	The Japanese gravitational-wave detector in the Tama region of Tokyo
TEM	Transverse Electromagnetic Mode [frequency]
TM	Test Mass
UHV	Ultra-High Vacuum
VEA	Vacuum Enclosure Area
WFS	Wavefront Sensor
ZnSe	Zinc Selenide, material comprising CO_2 laser optics

Abstract

The Laser Interferometer Gravitational-wave Observatory (LIGO) array's 4 km detectors have transitioned from an initial configuration (iLIGO) to an enhanced configuration (eLIGO) [1]. Both configurations relied on high circulating laser powers to achieve sensitivity goals between 150 Hz and 8 kHz. These power levels were sufficient to induce thermally driven focal affects in the primary optics. Since the detectors were designed to achieve maximum sensitivity when laser light was optimally coupled (mode matched) into the antenna, small deviations in focal parameters influenced performance. A laser based thermal compensation system (TCS) was installed for use in both configurations to counteract excessive or insufficient thermal lensing. Consequently a toy model has been studied to search for detector derived parameters that might be used to monitor the focal state of the two most affected optics. Additional thermal behaviors induced by the TCS were investigated and modeled.

1 Introduction

1.1 Gravitational Waves

Gravity is the fundamental force with which people are most familiar. For the most part, this force has been taught to be static and unchanging. Newton's law developed in the 17th century tells students that gravity could be modeled as a force that falls off in strength with the square of the distance.

In the early 20th century, Albert Einstein suggested a new theory of gravity to explain experiments conducted during the late 1800s and early 1900s. This new theory called general relativity expanded Newton's force by converting gravity from action at a distance to a phenomena characterized by the curvature of the 4-dimensional curvature of spacetime. In this theory, a simple premise abounds, matter and energy tells spacetime how to curve and the curvature of spacetime tells matter and energy how to move. As a mathematical artifact spacetime could no longer be represented as a scalar value with no direction. General relativity's gravity is fully described as by a 4x4 tensor [matrix] quantity [2].

One of the primary distinguishing features of general relativity from its predecessor theory was the prospect of time dependent variations from the locally flat spacetime, gravitational waves. These oscillations, derived in the early 20th century come in two varieties of polarization due to their tensor like representation, plus (+) and cross (X). Physically these waves are generated by objects possessing a time changing non-spherical mass distribution. More precisely this is called a time changing quadrupole moment. This can be thought of as a sphere with a bump on the side or two spheres orbiting each other. Therefore, sources for gravitational waves can be widely varied in theory. Anything from a meter stick turning end over end to a binary neutron star system can generate gravitational waves. Gravitational waves are estimated to travel through the universe at the speed of light (c). Most astrophysically generated gravitational wave frequencies are expected to be in the lower acoustic band (≈50 Hz to 5 kHz). According to general relativity, these waves interact with the local universe by an alternating stretching in one transverse direction and a compression in the orthogonal direction. As measured by freely floating test masses, gravitational waves change the separation distance between the test masses. The change in separation distance divided by the mean separation distance is called strain. However, gravitational waves of astrophysical origin can be estimated interact with Earth bound detectors at such a minute level that Einstein dismissed the possibility of measuring them altogether [2, 3].

In the mid-1970s, Hulse and Taylor discovered the first binary pulsar, PSR B1913+16. Precise timing measurements over three decades showed a decaying orbit size. After a large effort to determine the source of the orbital decay, general relativity's prediction of gravitational waves fit most precisely. The Hulse-Taylor binary was predicted to merge in approximately 300 million years. Close to the point of merger, the amplitude of the gravitational wave is expected to achieve rise dramatically and reach a level directly measurable by sophisticated displacement detectors on Earth devised in the late 20th century [2, 3].

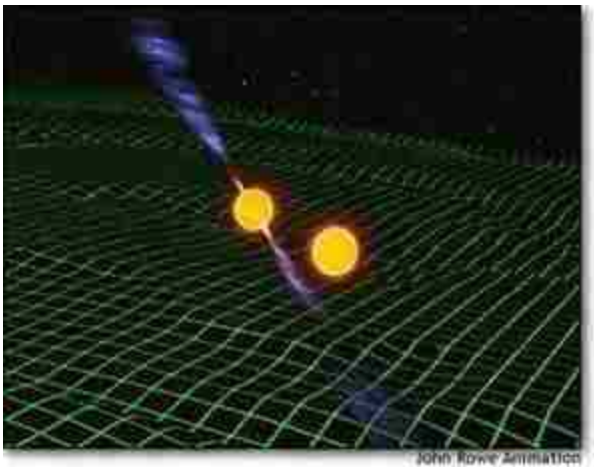

Figure 1-1: A depiction of a binary pulsar system. As these stars orbit each other, their orbital energy is converted to gravitational waves. These waves are shown as ripples in the fabric of spacetime represented by ripples in the green mesh. Picture credit: John Rowe (animation@rowes.com.au)

1.2 Laser Interferometer Gravitational-wave Observatory

The Laser Interferometer Gravitational-wave Observatory (LIGO) is one of several detector groups worldwide planning on demonstrating the existence of gravitational waves and mapping their astronomical sources. A LIGO detector functions on the principle of a laser-based Michelson interferometer and takes advantage of the Michelson's ability to sense differential displacements between its end mirrors and beamsplitter. Michelson arms differing in length generate phase differences in the travelling light fields. Upon interference, the output brightness can be fully constructive or destructive if the waves arrive in-phase or fully out of phase with each other respectively. If all environmental noises could be mitigated, the only source of differential motions would come from the projection of gravitational waves' strain onto an interferometer's arm lengths. Assuming a simple sinusoidal gravitational wave in the correct polarization impinges on a Michelson interferometer, than a sensitive enough Michelson interferometer whose mirrors were freely suspended would show a sinusoidal fluctuation in the brightness at the output port [4].

LIGO is comprised of a detector array split between Hanford, Washington (LHO) and Livingston, Louisiana (LLO). Each site consists of three large experiment bays called vacuum enclosure areas, VEAs. The largest bay at the vertex of the "L" arrangement is called the large vacuum enclosure area or LVEA. The buildings are separated by nearly 4 km. At Hanford a second set of VEAs sit 2 km away from the LVEA to contain a half-size interferometer that shares the larger 4 km interferometer's vacuum envelope. This distance forms the basic arms of Michelson interferometer needed in measuring gravitational waves. Such measures are not enough to reduce environmental noise from destroying sensitivity. To reduce the amount of acoustic and atmospherically induced noise the detectors are enclosed in vacuum envelopes comprised of low out-gassing 304L stainless steel. Large mirrors playing the role of freely falling test masses are suspended by simple pendulums whose longitudinal resonant frequency is roughly 1 Hz. These pendulums are further isolated from both natural and artificial ground motion through large active/passive seismic isolation stages. To prevent correlations from local ground

and atmospheric disturbances, the LIGO array is separated by nearly 3000 km. To improve displacement sensitivity of the interferometers, resonant Fabry-Perot cavities are situated in the Michelson arms [4].

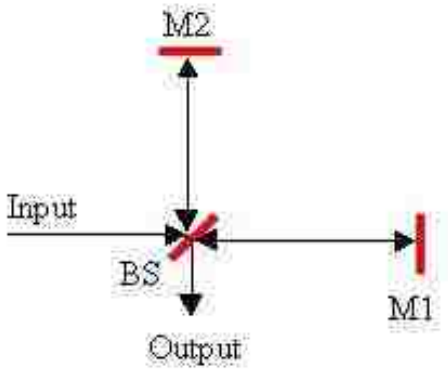

Figure 1-2: A cartoon of a simple Michelson with identical arm lengths. Light enters at the input port on the lower left. The light splits into two beams at the beamsplitter. Reflected light travels to mirror M2 on the y-arm. Transmitted light travels to mirror M1 on the x-arm. Upon reflection, both beams recombine at the beamsplitter. Interfered light passed out of the Michelson at the output port.

Figure 1-3: Aerial photos of the LIGO array. Left: The LIGO Livingston detector in Livingston, LA (LLO). Right: The LIGO Hanford detectors in Hanford, WA (LHO). The end station experiment buildings were positioned 4 km away from the corner station. The buildings at the mid-point of the LHO arms contain end mirrors for the 2 km gravitational wave detector. Identical buildings at LLO are empty.

Since this dissertation's experiments occurred during a transition period between improvements in detector configuration, each configuration is represented in this dissertation by acronyms "iLIGO" and "eLIGO." iLIGO or Initial LIGO operated between 2000 and 2007. Between 2005 and 2007, iLIGO detectors reached their prescribed sensitivity goals; both sites operated all three detectors in their full configuration for 2 calendar years collecting astronomical data [3]. In October 2007, iLIGO started incorporating four upgrades. These were installed in hopes to improve overall sensitivity [1]. The upgrades slightly changed the operating parameters and gravitational wave readout scheme. None of the primary optics or the infrastructure was altered. This improved version of LIGO is referred to as Enhanced LIGO or eLIGO.

1.3 Initial LIGO

Initial LIGO depended on a continuous wave 10 W Nd:YAG laser producing 1064 nm light to resonate in the interferometer and reduce shot noise to an amenable level. Shot noise is a quantum mechanical based error in which an imperfect sensor cannot recognize the exact number of particles impinging on it. The error corresponds to the square root of the number of objects (particles) counted. An additional improvement to reduce shot comes from the iLIGO operating point and the topology of the interferometer. iLIGO ran in completely destructive interference with respect to the central (carrier) wavelength. A partially transmissive mirror situated at the injection port of the Michelson interferometer reflected light back into the interferometer. The combination of destructive interference and the extra mirror permitted iLIGO to achieve sensible optical power levels. This four mirror Michelson is named a (resonant) power recycled Michelson interferometer [4].

In addition to the 1064 nm laser light, four additional frequencies were added to the main beam that eventually interacted with the interferometers. These additional frequencies were inserted using radio frequency (RF) electro-optic phase modulators (EOMs). Each phase modulator effectively added two additional frequencies and reduced the central (carrier) light by the magnitude of the RF optical excitation. These additional frequencies were used in an expanded version of the Pound-Drever-Hall locking scheme to control various length and alignment degrees of freedom in iLIGO's detectors. For the 4 km detectors, the primary phase modulated RF "sideband" was set at approximately $24.5\ \mathrm{MHz} \pm \frac{\mathrm{c}}{1064\ \mathrm{nm}}$. A second set of sidebands were placed at $61.2\ \mathrm{MHz} \pm \frac{\mathrm{c}}{1064\ \mathrm{nm}}$ [4].

Each LIGO detector was designed with six primary optics and a variety of auxiliary optics. The primary optics or core optics were built from low absorption fused silica from Heraus and Corning. Each large optic was fabricated as cylinders 25 cm wide and 10 cm thick. The beamsplitters were fabricated with 5 cm thicknesses. The curved optical faces of the mirrors were coated with a highly reflective multi-layer thin film comprised of alternating quarter wavelength layers of tantalum pentoxide and fused silica. The flat surfaces of the large optics are coated with similar materials to generate an anti-reflective coating. The optics were given a slight wedge (2 degrees) to prevent intra-optic interference and provide pickoff light beams for sensors and diagnostics [4].

The general configuration for the iLIGO 4 km detectors is shown in Figure 1-4. The two kilometer detector at LHO used additional pointing mirrors to direct light into its arms. Laser light was generated and initially filtered in a stage called the pre-stablized laser (PSL) table. Light then transmitted through additional filter stages and three EOMs before being correctly sized and focused [mode matched] by a reflective 3 mirror telescope in the input/output optics (IOO) stage. Laser light entered the interferometer through the recycling mirror (RM) on the lower left. The laser light was then split by a 50/50 beamsplitter (BS) and directed towards the 4 km resonant Fabry-Perot cavities. A single input test mass and end test mass formed a Fabry-Perot cavity. The light circulated in the cavities for approximately 1 ms before returning to the beamsplitter to interact with the laser light from the counterpart arm. This delay allowed the light time to interact with passing gravitational waves and accumulate induced phase differences. If the light fields arrived in phase, the recombined light travels upstream and was reflected by the RM back for recirculation. The cavity formed by the two ITMs, the BS, and RM was called the power recycling cavity or power recycled Michelson (PRM). The various

lengths of iLIGO were engineered to allow the carrier to circulate throughout the interferometer; the primary RF modulation was allowed to enter and resonate within the PRC. An intentional asymmetry in distance between the ITMs permitted the 24.5 MHz sidebands to transmit to the antisymmetric port. None of the lengths in iLIGO correspond to resonances for the 61.2 MHz sidebands. The designations RSB and NRSB refer to the resonant and non-resonant sidebands respectively [4].

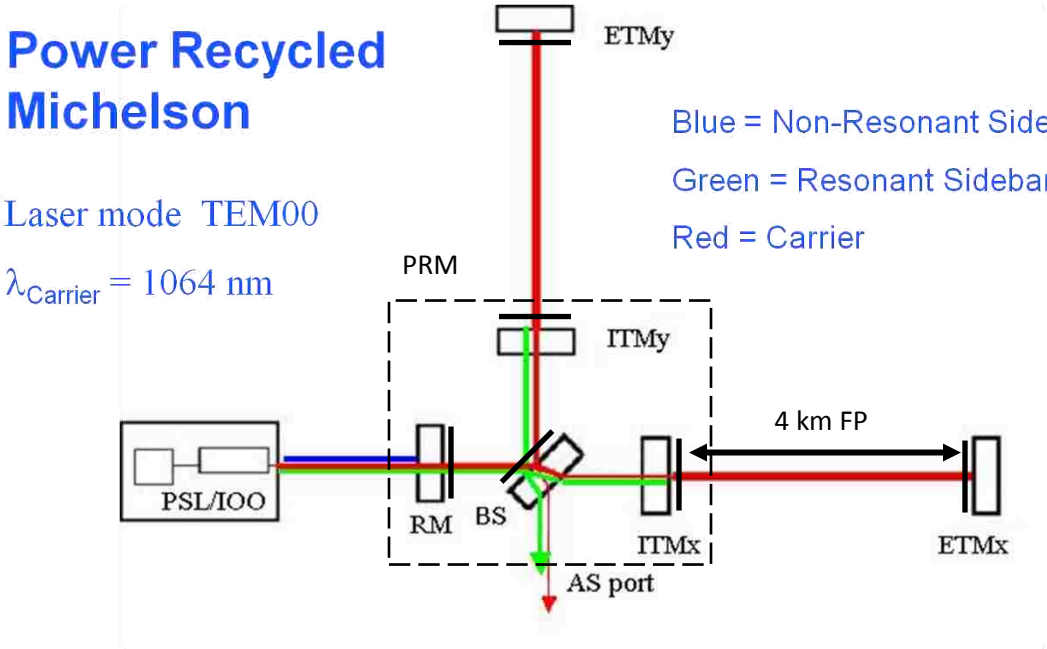

Figure 1-4: A schematic layout of the LIGO detector. Laser light leaves the pre-stabilized laser (PSL) and passes through a set of filter cavities, electro-optical modulators, and input/output optics (IOO). The IOO chain applies radio frequency (RF) sidebands for Pound-Drever-Hall locking of miror distances. Carrier light passes through the recycling mirror (RM) and to the beamsplitter (BS). Half of the light is directed to each Fabry-Perot arm cavity comprised of an ITM and an ETM. Carrier light returning to the beamsplitter is destructively interfered. Carrier light returning up towards the PSL/IOO block is reflected by the RM back to the BS. Sideband light escapes at the antisymmetric (AS) port along with carrier modulated by gravitational waves. These six mirrors from the LIGO resonator. The subscripts x and y refer to the coordinate axis on which they lie. The additional line adjacent the mirrors indicate which side is highly reflective. PRM = Power Recycled Michelson. FP = Fabry-Perot cavity.

iLIGO's interferometer length degrees of freedom were broken into four terms and controlled by four sensors at three output ports. These were the differential Fabry-Perot arm length (DARM), the common Fabry-Perot arm length (CARM), the differential "short" Michelson length (Mich), and the common power recycling cavity length (PRC or PRM). Sideband light transmitting or reflecting from these various ports formed local oscillators on respective photodiodes. As carrier light transmitted from these ports an RF optical beat could be detected by a photodiode. The RF photocurrent could then be demodulated with the appropriate phase and frequency to ascertain information regarding the interferometer's behavior. The all important differential degree of freedom of the arm cavity lengths was sensed at the antisymmetric port. The AS photodiode (ASPD) arrays signal was demodulated at 24.5 MHz in the quadrature phase with respect to the 24.5 MHz RF source to generate the differential arm (DARM) error signal. This scheme was also called the heterodyne readout. The beamsplitter pickoff light was used to sense the differentia or "short" Michelson length changes between the ITMs and the BS. This signal was also detected by a photodiode whose signal was quadrature phase demodulated at 24.5 MHz. The common displacement of the ITMs was sensed through the in-phase demodulation of the same BS

signal. The common arm cavity motion was sensed through the 24.5 MHz in-phase demodulation of the light reflected by the RM. The 61.2 MHz sidebands were used in later iLIGO to sense the PRM's resonant condition. This light was separated from the injected light using a commercially available Faraday isolator. Additional details about these signals and the elaborate control loops that use them were recorded in [5].

A detector under full length and angular control was called a "locked" interferometer. This was attributed to the notion that the detector was being actively held at the operating point. Laser power build up in this state reached a peak as a function of length and angle degrees of freedom.

Most signal acronyms in LIGO and this dissertation are formed by the port and the demodulation quadrature. For instance, ASi refers to the antisymmetric port light demodulated in-phase with 24.5 MHz source signal [5]. On a few occasions in this dissertation, RF signals that are demodulated at 61.2 MHz are compounded with a "2" after the port name.

In summary, LIGO ran in the initial configuration for 2 calendar years resulting in the best displacement sensitivities on record for a large gravitational wave observatory. The Figure 1-5 shows the amplitude spectral density for strain noise as a function of frequency. The solid line represents the sensitivity level for detection as prescribed by the science requirement document (SRD). The initial LIGO noise curve was limited by three primary terms. From 10 Hz to 40 Hz, the detector's noise curve was dominated by the vibrations transmitting through the seismic isolation system. This level differed between LHO and LLO due to geology. Noise between 40 Hz and 150 Hz was generated by a combination of sources including thermal, static charge build up on the test masses, and inadvertent contributions due to the length control loops. Above 150 Hz, the noise curve was dominated by the shot noise limited sensing of the Fabry-Perot cavity lengths [1, 3, 4].

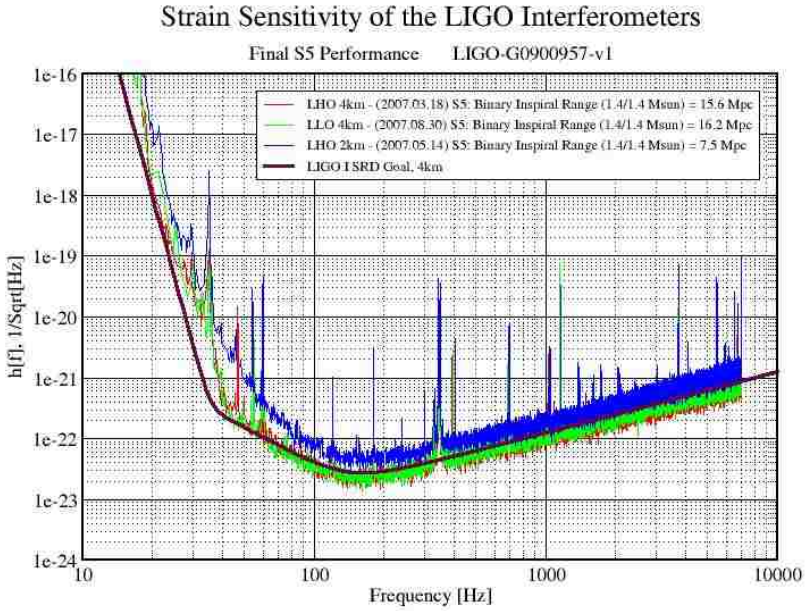

Figure 1-5: Official calibrated strain curves for the LIGO detectors.

1.4 Enhanced LIGO

Between October 2007 and April 2009, the iLIGO 4 km detectors received equipment upgrades for various subsystems. These upgrades not only aimed at improving the sensitivity of the LIGO array by 2-3 times but were also pathfinder projects for the second generation LIGO detectors, Advanced LIGO. The enhancements only affected the PSL, IOO, readout, and TCS. No other mechanical or optical infrastructures were affected. As a result, the core optics and the majority of the auxiliary optics were left alone [1].

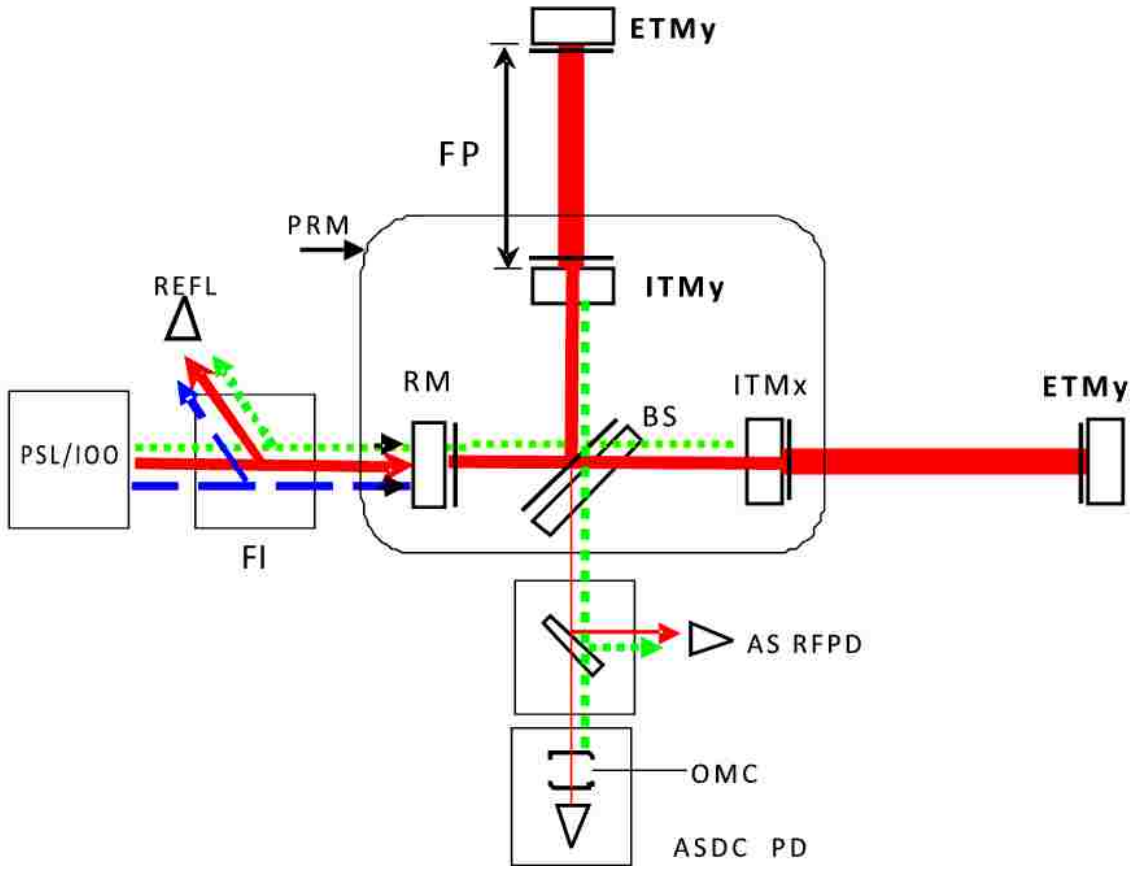

Figure 1-6: A schematic layout of the Enhanced LIGO interferometer. The primary upgrades in this schematic are the improved pre-stabilized laser (PSL), the second generation Faraday isolator (FI), the output mode cleaner (OMC), and the auxiliary heating lasers (not shown). The power recycled Michelson (PRM) portion of the interferometer is boxed. The 4 km Fabry-Perot cavities comprised of the ETMs and ITMs are labeled FP. AS RFPD refers to the radio frequency photodiodes. ASDC PD refers to the AS DC photodiode used to collect transmitted carrier light from the OMC.

To improve the shot noise limited sensitivity, the PSL's laser was increased from 10 W to 50 W. The IOO Faraday isolator was replaced with a design which could tolerate 100 W of laser radiation without incurring excessive thermal aberrations. The differential arm readout was altered from a RF frequency demodulation scheme to a direct intensity (DC) measurement of the carrier (DC readout). This was abetted by imposing a small differential offset in the ETM positions and adding an output filter cavity or output mode cleaner (OMC) to the antisymmetric port. The picometer scale offset moved the eLIGO detectors off the iLIGO dark fringe. The filtered carrier light leaking from the AS port would now theoretically be linearly proportional to differential disturbances on the arm cavities. The DC level of carrier light became the new differential arm error signal as opposed to the previous RF based signal. To

further mitigate acoustic noise at the antisymmetric port sensing table, the photodiodes and OMC were placed inside the vacuum envelope. A new generation active internal or in-chamber seismic isolator (ISI) was placed beneath the output table to filter ground motion. Finally, the TCS was fitted with more powerful 35 W CO_2 laser with an intensity stabilization systems to reduce intensity fluctuations that may perturb mirror positions. More efficient CO_2 projectors were installed to provide nearly 50 % of the 35 Watts available if needed during eLIGO commissioning and operations.

In April 2009, the eLIGO array began its most recent astronomical observation period called "science run 6" or S6. This run was intended to continue until the decommissioning and the Advance LIGO detector installation begins. Current sensitivity levels exceeded the SRD slightly in the shot noise dominated regime temporarily. Injected power levels as of November 2009 were recorded at roughly 8 W injected into the vacuum system. This power was similar to that used in iLIGO. At increased power levels, an increased number of sensing glitches were present from a large number of sources. One of these sources was suspected to be induced by an improper focusing of the input beam into the Fabry-Perot arm cavities at expected eLIGO power levels.

1.5 Introduction to the Problem

In both detector configurations, large circulating powers were required to maintain shot noise limited strain sensitivity. Noted in chapter 3, the number of photons on the beamsplitter is inversely proportional to the phase (displacement) measurement accuracy. Since the mirrors were made of fused silica, it was inevitable for the mirrors absorb some PSL laser energy. Inside the vacuum system, the mirrors had no effective means to remove the resultant heat buildup. Manners of conduction were not permissible due to fused silica's thermal conductivity and the poor contact made by the steel music wire using as pendulum suspensions. As heat accumulates in the mirrors, heat gradients generated by through thermal diffusion and net radiative flux drive a variety of thermally induced aberrations [6-8]. The dominant one being the thermal gradient induced change in the index of refraction, the thermal lens [6]. The mirrors most susceptible to this issue were the ITMs due to their position as input couplers to the arm cavities. Their highly reflective (HR) surfaces interacted with multikilowatt power of the arm cavities. The substrates transmitted hundreds of Watts at the iLIGO operating point.

The ITMs in iLIGO were curved to compensate for the thermal lensing at full design power [4, 9]. The iLIGO detector was designed to achieve maximum sensitivity when optimally mode matched to the injected laser light. Unfortunately the design complicated operations below the design power[10]. Compounding matters, each ITM presented a unique absorption values that often did not correspond with design requests. This injected the freedom of differential lensing. To improve operations below design power and contend with non-ideal absorption values, an auxiliary laser based heating subsystem was installed. This thermal compensation system, TCS, used 8 W carbon dioxide based lasers to project far infrared radiation onto the ITMs of each iLIGO detector. Two heating patterns were implemented to compensate for improperly heated mirrors. A central spot was used for under-heat conditions. An annulus pattern was used to "cool" overheated mirrors. Detector derived monitoring signals permitted commissioning teams to tune the TCS to optimize the detectors' performance [8, 11, 12]. This was deemed sufficient for the 2005-2007 astronomy data run, "S5."

Figure 1-7: An photograph of a TCS laser table taken at Livingston Observatory. The orange box contains a 35 W CO_2 laser that is shaped into a spot or an annulus and projected onto the ITM 15 m away via the vertical lauch tube. The steel tube adjacent the TCS bench is the vacuum envelope. The green pedestal at 10 o'clock is an optical lever pier.

eLIGO's configuration and operating parameters complicated issues for thermal lens monitoring signals. Akin to the breakdown of length degrees of freedom, the ITMs focal values could be referred to in both common and differential modes. Common mode refers to the sum of the focal lengths divided by two. Differential focal length refers to the difference in focal lengths divided by two. The new readout scheme prevents the differential focal signal from being sensed by removing the RF sidebands. Increased PSL power insinuates the collective or common focal lens. The increased power pressed the both differential and common focal monitoring signals into unexplored regimes. In these regimes, the monitoring signals ceased behaving in a linear fashion.

Therefore, it was practical to both study an interferometer's behavior during the transition period as well as develop a toy thermal model to search for alternate monitoring signals. When these signals presented a desirable nature, feedback calibrations were investigated. This would provide means to return eLIGO detectors to a state of optimal mode matching at nearly any power. The theory and results of these measurements and models were recorded in this dissertation.

2 Thermal Aberrations

2.1 Introduction

When high power lasers intersect glass, thermally induced effects occur irrespective of the glass's purity. The effects are not altogether unwanted; they are frequently exploited to improve performance at high optical powers such as those seen in high power laser heads[13]. However, when these effects push LIGO's detectors into non-optimal operating regimes, sensitivity to gravitational waves is lost. This chapter covers the theory of thermal lensing and its effects on LIGO. It is followed by models of the effects to a gravitational-wave detector.

2.2 Theory

2.2.1 Thermal Aberrations

When materials heat up, their properties differ across the object depending on the local temperature. In optical hardware, heat gradients result in optical wavefront aberrations. Examples of wavefront aberrations are defocusing, astigmatism, or even depolarization. These aberrations, or changes to the optical path length (OPL), change the laser wavefront shapes and electromagnetic field distributions in some cases. Characteristically the optical path length can be written as four terms [14].

$$OPL = OPL_{innate} + \Delta OPL_{thermal} + \Delta OPL_{expansion} + \Delta OPL_{stress}\,. \tag{2.1}$$

Now we examine each optical path length quantities separately.

The first term represents how a medium changes the optical path length.

$$OPL_{innate} = nL_0. \tag{2.2}$$

Here n is the index of refraction and $L_0$is the physical length of the medium. Although this term is not thermally dependent, it is by far the largest physical term in optical path length changes.

$$\Delta OPL_{thermal}\,(\vec{r}) = \frac{dn}{dT} L \Delta T(\vec{r}). \tag{2.3}$$

The largest thermal term for many materials is the aberration due to the thermally dependent index of refraction, thermal lensing. In the equation above, $\frac{dn}{dT}$ represents the thermo-refractive coefficient. This is the derivative the index of refraction with respect to temperature. L is the length of the material, and $\Delta T(\vec{r})$ is the temperature distribution as a function of coordinate.

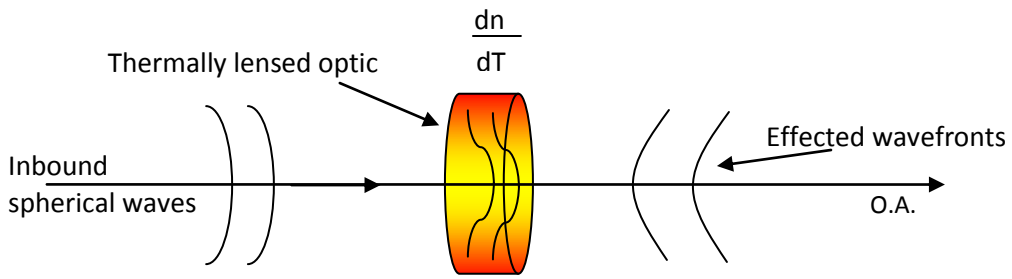

Figure 2-1: Representation of a thermal lens affecting incoming spherical wavefronts from the left. Intensity distributions and resulting wavefronts are altered after passing through the thermal lens. O.A. represents the Optical Axis or axis of light propagation.

As a material heats up, its electronic response expressed classically as the susceptibility tensor, χ_{mn}, changes [15]. This means that the electrons responsible for interacting with the electromagnetic fields will phase retard, or differentially slow, the passing wave. For some crystals, heat gradients cause thermal lenses that are larger in one axis compared to another. This results in an astigmatic lens. Generally, thermal lenses generate higher order mode distortions that cannot be repaired using simple spherical lens telescopes. Instead to counteract this thermal lens, a counter-thermal lens using materials with an opposite $\frac{dn}{dT}$ is capable of nearly removing this effect.

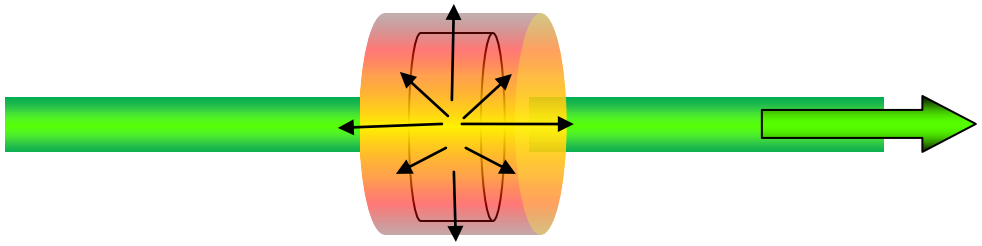

Figure 2-2: The green line indicates a laser beam passing through a cold optic outlined in black. Heating results in non-uniform expansion as indicated by the increased size on axis. The yellow region receives more heat than the medium's perimeter.

Thermal expansion is possibly the best known thermal effect outside the field of optics.

$$\Delta OPL_{expansion}\ (\vec{r}) \approx 2\alpha_{exp}\, n\omega \Delta T(\vec{r}), \tag{2.4}$$

where α_{exp} is the expansion coefficient; ω is the laser spot size (radius); *n* is the index of refraction; and $\Delta T(\vec{r})$ is the radial temperature distribution. As an optic heats up colder regions outside the heated region restrains uniform expansion. This changes the effective OPL as the optical faces expand differentially into the beam-line [14]. For mirrors, the heated region may be modeled analytically as a hemisphere whose radius equals the spot size. Non-uniform heat distributions, such as those in LIGO, result in mirror surface deformation. Delicate changes to resonator surfaces readily influence high precision measurement.

Finally we have stress induced effects to the OPL, ΔOPL_{stress}. The approximate effect on OPL is noted in references, [6], [14], and [16].

This effect is far smaller in comparison to thermal lensing for isotropic materials such as fused silica. For other crystalline materials, this may not be so. However, for the purposes of LIGO type optics this term is neglected [6, 14, 16]. Typical magnitudes of the above coefficients are listed in Table 2-1.

Table 2-1: Optical coefficients for fused silica.

Fused Silica	
L (typical LIGO core optic thickness) [cm]	10
k_{th} [W/mK]	1.38
dn/dT [1/K]	1×10^{-5}
α_{exp} [1/K]	0.5
ρ_{12}	0.27
n	1.45
Absorption ratio for LIGO [%]	1-5 ppm

2.2.2 How Optics Absorb Light

Thermally induced effects require a thermal gradient to invoke the aforementioned optical aberrations. This statement leads to a simple question, "How do pure optics absorb energy and heat up?" A detailed presentation is given in references [15] and [16].

As laser radiation passes through a dielectic material, charges within the material respond by momentarily polarizing the medium. This polarization is important in this context since it defines the index of refraction. Since in a non-conductive material's electrons are bound, we can model the electrons as a damped harmonic oscillator. The damping term comes from the nature of dielectrics, electrons are bound to follow paths called Brillouin zones [17].

The presence of this damping term leads to the polarization always possessing a real and imaginary term. At the resonant frequency, polarization is purely imaginary. The resonant frequency represents the region where a medium's absorption coefficient increases dramatically. Practically, the material at resonant frequencies becomes opaque.

The influence of polarization is more precisely defined by a 3x3 susceptibility matrix. Solving the Maxwell wave equation for electric fields allows one to solve for the wave vectors in terms of the susceptibility. Ultimately, the wave vectors are complex. The imaginary term becomes known as the absorption coefficient. This is what results in optically heating irrespective of how pure or transmissive the material may be [15, 16].

2.2.3 Representation of the Thermal Aberration on Laser Fields

In this section, the method by which aberrations affect laser wavefronts is shown. This section culminates in a toy equation, and the scheme presented is valid for nearly any level of thermal aberration granted one knows how to correctly express the induced phase shift. Since LIGO's laser spatial distributions are Gaussian in structure, this presentation is given in the Hermite-Gauss basis.

One begins with a fundamental Hermite-Gauss laser whose characteristics are derived in references [18], [19], [20], [21], and [22]. Due to the theory of superposition, one can express laser light fields as a combination of terms.

$$Light\ Field = \sum (\ Amplitudes \cdot Longitudinal\ frequencies \cdot Transverse\ Field\ Distributions).$$

2.5

Readers may be more familiar with the first two terms than the third. The amplitude term carries information about how much energy is conveyed through space. The longitudinal frequency corresponds to the frequency of wave front arrival. This is what one means by "red", "green", "blue", and "infrared." The third term details the field or intensity distribution. For example, a poorly designed flashlight will non-uniformly illuminate a piece of paper. Whereas a better one may have uniform illumination appropriate for reading. Transverse field distribution represents such a thing.

A purely Gaussian laser field drops in strength from the propagation axis with a Gaussian distribution and has no zero crossings. In the one dimensional Hermite-Gaussian (a rectangular symmetric) basis, the electric field distribution (strength as a function of one transverse spatial coordinate "x") is represented as follows:

$$U_0(x,z) = \left(\frac{2}{\pi}\right)^{\frac{1}{4}} \sqrt{\frac{1}{\omega(z)}} e^{-\frac{x^2}{\omega^2(z)} - \frac{ikx^2}{R(z)}}.$$

2.6

where:

$$R(z) = \left(z + \frac{{z_R}^2}{z}\right);$$

$$w(z) = \omega_0 \sqrt{1 + \left(\frac{z^2}{{z_R}^2}\right)}.$$

Here $\omega(z)$ represents the beam spot size [radius], *k* is the scalar wavenumber in the direction of propagation, and $R(z)$ is the wavefront radius of curvature. z_R represents the one half the collimation distance also known as the Rayleigh range. ω_0 equals the narrowest radius in a Gaussian beam also called the beam waist. z is the direction of propagation. Electric field amplitudes only serve as multiplying factors. Therefore, I shall leave them out to focus on the distribution.

At the field's waist, the focal point in the laser beam, the equation 2.7 simplifies in one dimension to

$$U_0(x,0) = \left(\frac{2}{\pi}\right)^{\frac{1}{4}} \sqrt{\frac{1}{\omega_0}} e^{\frac{x^2}{{\omega_0}^2}}.$$

2.7

The subscript zero indicates waist values. As the laser passes through the thermal aberration the electric field profile obtains a phase shift [16, 19, 23].

$$U_{aber} = U_0 e^{-k\Delta OPL_{thermal}} .$$

2.8

The affected beam can be represented as an infinite sum of Hermite-Gauss modes using the initial beam as the working basis.

$$U_{aber} = \sum_{n=0}^{\infty} c_n H_n \left(\frac{\sqrt{2}x}{\omega(z)}\right) U_0.$$

2.9

Here $H_n \left(\frac{\sqrt{2}x}{\omega(z)}\right)$ represents the normalized physicist's Hermite polynomial, and c_n refers to numerical weights in the infinite sum. The objective of the sum is to describe the distribution of laser light intensity. These weights can be determined by calculating the overlap integral between the thermally effected "mode" and the individual field distributions comprising the sum.

$$c_n = \int_{-\infty}^{\infty} {U_{aber}}^* U_n dx.$$

2.10

In this equation, U_n are the plethora of Hermite-Gauss field distributions in U_0's basis. Summing the most heavily weighted terms in this infinite sum yields a solution representative of the thermally altered field for one dimension. A second identical aberrated field can be built for the y-axis. The final two dimensional field representation is generated by merely multiplying the two axis specific fields together.

The result of a lens, a telescope, and simple propagation through space can be represented in this same fashion. One only needs to alter the phase factor. This case is even valid with absorption since absorption cases may present distributed field attenuation.

2.2.4 Consequences to Sensitivity

Initial LIGO's sensitivity could be compromised when the detector's optical parameters deviated from design parameters. According to reference [6], among these parameters were as follows:

A. Decrease PRM carrier power gain;
B. Decrease arm cavity circulating power;
C. Decrease PRM SB power gain;
D. Increase contrast defect.

The first two issues essentially affect the same point. Reducing amounts of laser power circulating in iLIGO-like interferometers reduces the shot noise limited phase sensitivity (see section 3.1). For a simple Michelson, this uncertainty is written as a function of frequency in reference [6].

$$\delta\Phi_{shot}(f) = \frac{d\Phi}{dP_{AS}}\delta P_{AS}$$

$$= \sqrt{\frac{2hc}{\lambda P_{BS}}}.$$

2.11

Here $\frac{d\Phi}{dP_{AS}}$ represents the derivative of optical phase with respect to power measured at the anti-symmetric port, AS, h is Planck's constant, c is the speed of light in a vacuum, λ is the wavelength of the light in the interferometer, and P_{BS} is the power intersecting the beamsplitter.

The reader should notice that the function is inversely dependent on light levels. More power interacting at the beamsplitter, P_{BS}, increases phase sensitivity. Circulating laser power in the arm cavities exceeds the light levels on the beamsplitter by more than ten times. Again, high laser powers are required in a Fabry-Perot cavity to accurately measure mirror displacement [6].

A second interpretation of this function indicates shorter wavelength laser light improves phase sensitivity. For the LIGO group, shorter wavelengths in the visible region are not used since the solid state infrared Nd:YAG lasers are suitably stable and do not suffer problems observed with visible or UV lasers such as optic deterioration.

The phase uncertainty can be converted into a differential displacement spectrum for a simple Michelson interferometer by multiplying by the wavenumber.

$$\delta x_{shot}(f) = \frac{1}{8\pi}\sqrt{\frac{2hc\lambda}{P_{BS}}}.$$

2.12

Here $\delta x_{shot}(f)$ represents the fluctuations in position as a function of frequency [6].

Since gravitational wave detectors are calibrated in units of strain, it is reasonable to convert the displacement spectrum to a strain spectrum. This operation is performed by multiplying the displacement by the inverse of the half arm-length, L.

$$\delta h_{shot}(f) = \frac{2\sqrt{2}\delta x}{L}$$

$$= \frac{1}{2L}\frac{\lambda}{2\pi}\sqrt{\frac{2h\nu}{P_{BS}}}.$$

2.13

The above equation only holds for a Michelson detector.

In the introduction, the author mentioned the arm cavities were installed to increase phase sensitivity. This occurs by increasing the time for the carrier to interact with the gravitational wave. A rough means to include the arm cavity's contribution to a iLIGO-like configuration is shown in equation 2.14 [6].

$$\delta h_{shot}(f) \propto \frac{1}{L\mathbb{G}_{arm}} \frac{\lambda}{2\pi} \sqrt{\frac{2h\nu}{P_{PRM,c}}} \qquad \textbf{2.14}$$

where:
$P_{PRM,c}$ is the total carrier light power in a power recycled Michelson cavity;
$\mathbb{G}_{arm}$ is the arm optical power gain.

In summary, loss of arm cavity carrier power reduces the precision of measuring arm length change, power loss in the PRM leads to precision loss of phase difference information. This is non-trivial since gravitational-wave induced displacements must be read of as phase differences between the two resonant arm cavities.

An improved approximation is derived in chapter 2 of reference [6] for the iLIGO interferometers. The ultimate equation multiplies dependencies on the light levels of the 24.5 MHz (resonant) sidebands as well as carrier light that leaks from the AS port. The dependency on sideband power inside the PRM refers to the ability to control length perturbations. The dependency on carrier leakage refers to the amount of carrier light randomly leaking from the AS port.

Sidebands in both variants of LIGO used sidebands as a means of controlling the auxiliary degrees of freedom (CARM, Mich, PRC, alignment). Deviations in their respective control loops could interfere with LIGO's ability to control the difference in arm length [5]. Loss of sideband power therefore immediately hinders the precision of the length and angular stabilization loops [6].

Contrast defect refers to the amount of carrier light leaking from the AS port due to imperfections in the interferometer when set to fully destructive interference. One source of contrast defect is the differences in mirror reflectivity. This results in beams of unequal intensity interfering at the beamsplitter. Light leaks out the AS port at the darkest interference. As thermal aberrations affect a perfectly tuned apparatus, the contrast defect increases due to beam overlap dissimilarities. In eLIGO-type detectors, contrast defect generated carrier light that transmits through the OMC can increase shot noise.

2.2.5 Counteracting Thermal Aberrations

A few theoretical means to counteract thermally induced aberrations have been studied in the past. Each one had its advantages and disadvantages especially when operating within high precision device such as LIGO. This section explains the principles behind the each thermal compensation variant.

Since the thermal lensing term dominated iLIGO core optics, a passive optic could have provided one solution. This solution assumed no pathological thermal expansion in the mirror or compensatory hardware noted below. Combining equations 2.1, 2.3, and 2.8 the distortion could be written as follows:

$$U_{aber} = U_0 e^{-k\frac{dn}{dT}\Delta T(x,y)L}.$$

2.15

An opposite thermal lens using materials with a thermo-refractive coefficient of opposite sign can mitigate the phase term in equation 2.15. Assuming that the absorption coefficients of the two materials are similar in magnitude, the corrective material slab length can be computed as shown in equation 2.16

$$\left(\frac{dn}{dT}\Delta T(r)L\right)_{material\ 1} - \left(\frac{dn}{dT}\Delta T(r)L\right)_{material\ 2} = 0.$$

2.16

The above equation also implies that the thermal distributions must be similar to each other. Below a simplified scheme using lenses is shown.

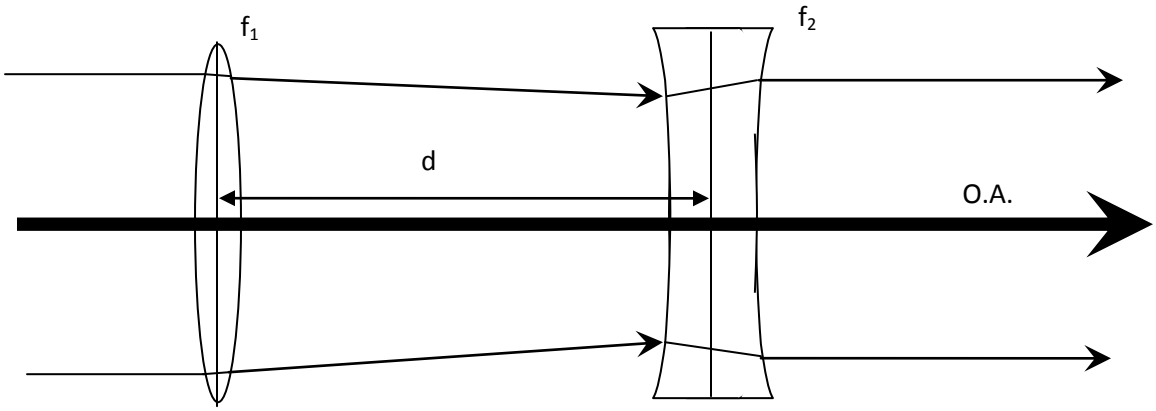

Figure 2-3 Illustration demonstrating how to correct a simple spherical lens. Lens f_1 has a positive focal length. Lens f_2 has a negative focal length. "d" is the distance between lenses.

If the distance, d, in Figure 2-3 is small compared to the lenses focal lengths, the negative lens (f_2) can perfectly compensate the converging lens. Here I make use of the thin lens equation;

$$\frac{1}{f_1} + \frac{1}{f_2} - \frac{d}{f_1 f_2} = \frac{1}{f_{total}}.$$

2.17

The two focal lengths equal and opposite yield a result of zero diopters (no change). Ideally the corrective and offensive media would be close to each other to reduce complications due to the Gouy phase shift and beam expansion [16].

This means of compensating wavefront distortions was not deemed acceptable for iLIGO or eLIGO core optics. It would have foremost added thermal noise fluctuations to the detector. The installation of the compensating glass would have required vacuum incursions as well as extra suspension hardware. Finally, the compensatory glass would have added extra optical losses. This scheme was deemed suitable for eLIGO's Faraday isolator.

Another means of counteracting both thermal lensing and thermal expansion was described in R. Lawrence's 2003 MIT thesis [6]. This method involved the addition of resistive ring heaters (toasters) suspended near the anti-reflective side of the ITMs. If most of the heating occured in a mirror's coating, the highly reflective surface naturally heated faster and beyond that of the substrate. The ring heater was intended to drive an annular thermal lens into the anti-reflective surface of an ITM originating from the edges. Essentially a counter lens could be placed centimeters away from the self-induced lens. Although this method of compensation would have been ideal, vacuum incursions would have been required to install the system and possibly maintain it. Such a device is being prototyped for Advanced LIGO.

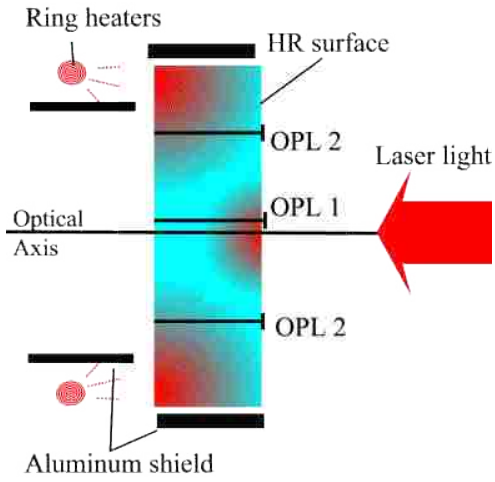

Figure 2-4: A cartoon of ring heating compensation (side profile). The arm cavity beam generates a hot spot at the center of the HR surface. Resistive ring heaters generate an annular thermal lens on the AR surface. When the resulting optical path length (OPL) for the central path (OPL 1) equals the OPL in the outer regions (OPL 2), the ITM's thermal lens is nulled.

Reference [7] explored a third option involving auxiliary heating lasers. A CO_2 based laser would be used to inscribe a thermal aberration that mitigates the self-induced lens similar to the ring heaters. The laser system was also designed to project two (transverse) spatial patterns, central and annular. This added the capacity to centrally heat LIGO's optics should their absorption coefficients levels fall below the expectation. CO_2 based lasers were utilized since fused silica is highly absorptive at 10.6 micron wavelengths. The thermal compensation system (TCS) was to be installed outside the vacuum envelope. Projection optics were to route the 10.6 micron light onto the high reflective surface of the input test masses. The primary drawback to this scheme laid its inability to quickly and efficiently counteract positive thermal lenses [9]. Another drawback laid in the interaction of the CO_2 laser light directly with the highly reflective surface of the ITM. The 10.6 micron radiation added to the thermal noise on the surface of the test mass [6, 12], which increased the mirror's position noise. This in-turn could decrease the gravitational-wave signal to noise ratio.

Selection and implementation of the above counteraction methods required ease of implementation and thermal lens mitigation capacity. Use of a material with a negative thermally dependent index of refraction would have increased thermal noise and added lossy materials to the interferometer. It also would have added weight to the optical payload (another mirror suspension) already hanging from a seven stage isolation system. Ring heaters would have demanded an incursion into the vacuum system. Venting an ultra high vacuum system is expensive and time consuming. Their proximity could have also

induced static charging issues on the ITMs. Therefore, incorporating a CO_2 projection system was desirable. Using laser light as a heater, the laser head and projection optics was located outside the vacuum system at an available viewport. The radiation noise issues were reducible via laser intensity control loops.

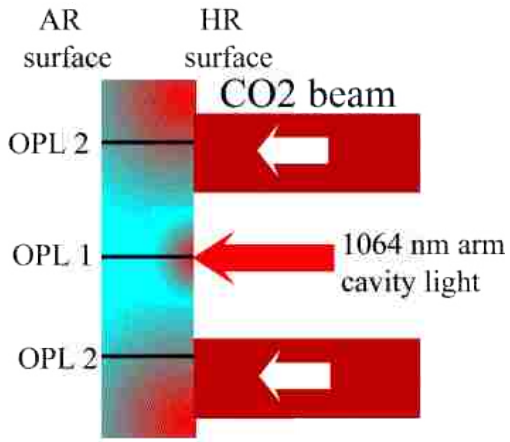

Figure 2-5: An illustration of the CO_2 laser induced compensation (side profile). The arm cavity light forms a central hot spot on the HR surface of an ITM. The CO_2 laser light in the annulus pattern forms a heated ring region. This equalizes the optical path lengths of the central path and outer paths. In a perfectly mode matched interferometer, this is called an optimally compensated lens.

As noted in the introduction, the TCS laser projectors installed in iLIGO and were upgraded for eLIGO. The use of a ring heater and laser heater hybrid was being designed during the writing of this dissertation.

2.2.6 Problem Due to Design Curvature

In the introduction, it is mentioned that the ITMs were excessively curved, "pre-curvature," to counteract the anticipated thermal lensing at iLIGO's operating power. This excessive "pre-curvature" generated difficulties at circulating powers too low to thermally load the ITMs. These difficulties are quantified in chapter 5 and can be initially expressed using stability analysis of the two cavities involved in the interferometer [19].

Cavity stability parameter, g, simply requires the product of each mirror's g -factor falls between 0 and 1 [15, 18-22, 24-26]. Beyond this regime the confinement equations indicate that a resonator has no reproducible transverse mode. This means light escapes laterally around the bounding mirrors instead of passing through them.

LIGO Livingston's arm cavities' stability parameter can be readily calculated using the following equation.

$$g_n = 1 - \frac{L}{\rho_n}, \tag{2.18}$$

where

L : geometrc length of the cavity,

ρ : radius of curvature of the nth mirror.

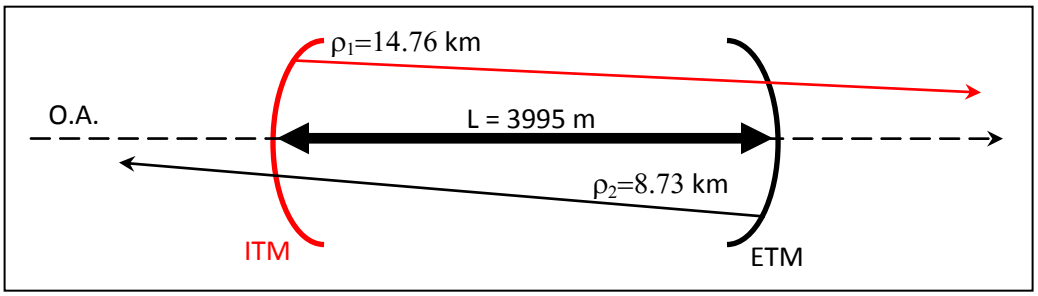

Figure 2-6: A depiction of a LIGO arm cavity. The distance between the two mirrors is slightly less than 4 km. The end test mass, ETM, has a 60 % shorter focal length than the input test mass, ITM.

$$g_{ITMx} = 0.7293.\ g_{ITMy} = 0.7249$$

$$g_{ETMx} = 0.5424.\ g_{ETMy} = 0.5419.$$

$$g_{ITMx}\,g_{ETMx} = 0.3956.\ g_{ITMy}\,g_{ETMy} = 0.3928.$$

2.19

This yields a stability parameter of 0.40. Such a result implies that the arms cavities are geometrically incapable of sustaining multiple transverse modes when on the fundamental resonance. A stability parameter equal to 0 or 1 permits transverse modes to circulate unhampered.

The results for the cold PRM were quite different. Recall Figure 1-4 outlines the four mirrors involved in the PRM, the RM, BS, and two ITMs. The average length of the power recycled Michelson is roughly 9 m. Here the average length is taken by taking the means between the ITMs and their respective face of the BS before adding to the RM to BS length. Since the PRM has three mirrors with one that shared optic, the RM, we can use average the radius of curvature of the ITMs to find the PRM's stability parameter.

$$g_{RM}\,g_{ITM} = \left(1 - \frac{L_{PRM}}{\rho_{RM}}\right)\left(1 - \frac{L_{PRM}}{\rho_{ITM}}\right),$$

$$\approx 1.003.$$

2.20

The result is greater than 1, an unstable solution. While unstable cavities are useful in particular areas of laser engineering, they are not welcome in LIGO. Next let us compute on what branch of instability the PRM lies. This can be performed by calculating the ray trace matrix for one round trip. The magnitude of the half-trace, "m", yields the answer.

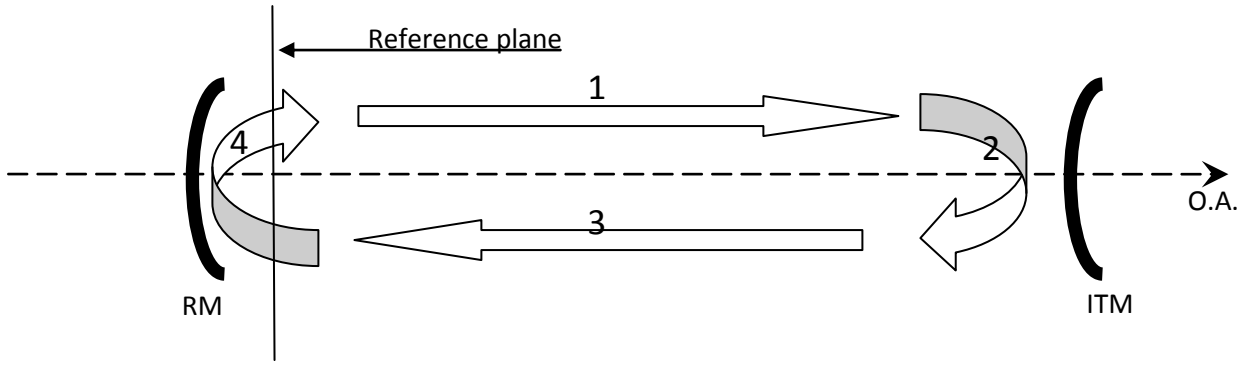

Figure 2-7: An illustration showing the direction of ray trace matrix calculation and the direction of field propagation within the power recycling cavity. O.A. indicates the optical axis. RM and ITM refers to the recycling mirror and input test mass respectively.

$$M_{tot} = \prod_s M_s \ ; \tag{2.21}$$

$$M_{tot} = \begin{pmatrix} A & B \\ C & D \end{pmatrix}. \tag{2.22}$$

$$M_{RM} M_d M_{ITM} M_d = \begin{pmatrix} 1 & 0 \\ \frac{2}{15.78\ km} & 1 \end{pmatrix} \begin{pmatrix} 1 & 9.004\ m \\ 0 & 1 \end{pmatrix} \begin{pmatrix} 1 & 0 \\ \frac{-2 \times 1.44963}{14.76\ km} & 1 \end{pmatrix} \begin{pmatrix} 1 & 9.004\ m \\ 0 & 1 \end{pmatrix}. \tag{2.23}$$

$$m = \frac{1}{2}(A + D),$$

$$= 1.0029 \tag{2.24}$$

Again the "m" originates from self-consistency equations [19]. An m > 1 indicates a resonator in the positive branch of instability. Physically this means circulating light fields never pass through a focus. Divergent fields within such cavities will continue to diverge until they leak around their mirrors. From the calculated m, one can determine how much the beam expands on each round trip. From the consistency equations, one can computer λ [19].

$$\lambda_{a,b} = m^2 \pm \sqrt{m^2 - 1}. \tag{2.25}$$

The results for both λ_a and λ_b differ from unity by 8 percent. Therefore, the beam contained in the cold iLIGO PRM expanded 8 percent each round trip. During iLIGO studies, the resonant (24.5 MHz) sidebands were shown to possess different spatial profiles and different centroid positions in the PRM (see chapter 6 and reference [10]).

The results of this brief analysis indicate that the PRM had a dramatically different behavior when compared to the arm cavity. These analyses are based on actual best known LLO mirror curvatures and distances. Therefore, small perturbations in cavity parameters from heating are important. This presents the necessity for a thermal compensation package at sub-design powers, and the need to monitor the ITM focal behavior.

3 Applications to Interferometers

During the design construction of iLIGO, it was known that multi-kilometer scale detectors required thousands of Watts circulating in the arm cavities. This chapter briefly outlines analytic predictions of thermal responses in interferometer optics which serve as analytic benchmarks in chapter 5.

3.1 Recap of Required Powers

The largest motivation for requiring large circulating powers originated from the shot noise limited sampling. Laser light used in both configurations of the LIGO detectors was assumed to follow Poissonian statistics. This model states that the error in the average number of particles counted in a given time equals the square root of that number. The LIGO detectors were ultimately counting experiments for light particles (photons). Increased amounts of light were simple means of mitigating shot noise. There is another reason for LIGO's high arm powers. Intuitively, the precision of mirror position cannot be sampled continuously using quantized particles such as photons. Therefore, presenting large numbers of photons in a near constant stream provides enough samples to simulate nearly continuous mirror position sampling. In both LIGO configurations, this applies to the distance between the ITMs and the ETMs.

One naïve means of computing the number of photons necessary interacting on a simple Michelson detector's beamsplitter is shown as follows. Gravitational waves originating 60 million lightyears away in the Virgo galactic cluster are expected to arrive at Earth with a strain root-means square (RMS) amplitude of 10^{-22} [2, 27]. The arm size of a simple Michelson detector required to detect a gravitational wave at 100 Hz is roughly 800 km [16]. Since 3200 km (2 detectors worth) of contiguous isolated land is not often for sale, we assume that the light bounces between the arms 200 times. The phase difference between the two arms is computed as shown.

$$\begin{aligned}\Delta\varphi &= \delta\varphi_x - \delta\varphi_y, \\ &= 4\pi\frac{L}{\lambda_0}Bh, \\ &= 4\pi\left(\frac{4000\ \mathrm{m}}{1064\ \mathrm{nm}}\right)(200)(10^{-22}), \\ &\sim 10^{-9},\end{aligned} \tag{3.1}$$

where:
B: the number of bounces,
h: strain,
L: arm length,
λ_0: light wavelength.

Next the (Heisenberg) number-phase uncertainty relationship is used [28].

$$\Delta N \Delta \varphi \geq 1.$$

3.2

Here:
ΔN : variance in the number of particles
$\Delta \varphi$: variance in the phase of particles.

The value ΔN corresponds to (Poissionian) uncertainty in photon number (shot noise). The average number corresponding to this shot noise is the uncertainty number squared.

$$\Delta N = \frac{1}{\Delta \varphi}.$$

$$N = \Delta N^2,$$

$$\sim 10^{18} \text{ photons}.$$

3.3

The sample time needed to measure one cycle of a 100 Hz gravitational wave is 0.01 seconds. This sample time affects the power associated with this many photons.

$$P = \frac{N h \upsilon}{\tau}$$

$$\sim 100 \text{ W}.$$

3.4

Where:
h : Planck's constant,
υ : optical frequency,
τ : sample time.
This argument has been called the energetic calculation by K. Thorne in a 2001 lecture series [27]. Other contrivances must be added to complete this argument such as the operating point of the simple Michelson at the half-fringe or 50 % constructive interference point and the ability for a perfectly efficient photodiode to handle at least 50 W of continuous laser light.

An equally simple approximation can be made for the power within a 4 km arm cavity from this point. The approximate power gain of a Fabry-Perot cavity can be approximated by $1/(1 - T_{input\ \ coupler})$. Here the input coupler is the ITM.

$$T_{\text{input coupler}} = 0.97.$$

3.5

$$P_{\text{circ}} \approx \frac{P_{\text{Beamsplitter}}}{\left(1 - T_{\text{input coupler}}\right)}$$

~ 1000 W.

3.6

This emphasizes the amount of power flowing through the ITMs as well as reflecting off its high reflective coating.

The actual LIGO detectors used a slightly different operating scheme to advance shot noise limited sensitivity at the sensing photodiodes. In theory, arm cavity circulating power gain is nearly 5 kW per every 1 Watt injected at the recycling mirror. This is the equivalent of many industrial cutting and welding lasers.

3.2 Analytical Description of Hot Fabry-Perot Based Interferometers

Chapter 2 indicated thermal aberrations were functions of thermal distributions. These distributions may be expressed in a pair of analytic approaches. The first method assumes time independent low and uniform absorption throughout the large mirrors. The second analytic approach assumes higher optical intensities interacting with the substrate and coating of a finite mirror. The second approach is used as an analytic benchmark in this dissertation.

3.2.1 Time Independent, Low Absorption Limit, Infinite Mirrors

Both configurations of LIGO could be held in either fully locked states with all mirrors controlled or with only a few pertinent mirrors aligned. Instances when the ITMs and BS were aligned and controlled were called locked Michelson states. Instances when the ITMs, BS, and RM were aligned and controlled were called locked PRM states.

An interferometer in either state applied heat from the anti-reflective (AR) surface of the mirror. A temperature distribution originally used for purely radial heat flow in a long Faraday optic may be applied here as the ITMs followed the assertion of weak absorption, small radiative interactions, primarily radial heat flow, and static heat loading.

The heat diffusion equation written as

$$\nabla^2 \mathrm{T}(\vec{\mathrm{r}}) + \frac{\mathrm{q}}{\kappa} = \frac{1}{\mathrm{D_{th}}} \frac{\partial \mathrm{T}}{\partial \mathrm{t}}.$$

3.7

Where:

q: heat source distribution,
$\mathrm{D_{th}}$: thermal dispersion coefficient,
κ: thermal conductivity,
$\mathrm{T}(\vec{\mathrm{r}})$: position dependent temperature.

The static case can be re-written as

$$\nabla^2 T(\vec{r}) + \frac{q}{\kappa} = 0.$$

3.8

Continuing the assumption that the PSL light is the only heat source we come to the same result noted for heat solutions in Faraday isolator studies [16, 23]. Since the glass is intended to be transparent, the heat source is uniform throughout the substrate. The source can be modeled as a Gaussian beam multiplied by the absorption coefficient α.

$$q(r) = \frac{4\alpha P}{\pi\omega^2} e^{-\frac{2r^2}{\omega^2}}$$

3.9

where P is the power passing through the substrate, ω is the spot size on the mirror, and r is the radial coordinate. Since the Michelson lock results in the beam passing the substrate twice, the heat source above has a factor of 4 rather than a factor 2. Combining equations 3.8 and 3.9 in cylindrical coordinates we acquire the following solution to the temperature distribution.

$$\frac{1}{r}\frac{\partial}{\partial r}\left(r\frac{\partial}{\partial r}\right)T = -\frac{1}{\kappa}\frac{4\alpha P}{\pi\omega^2} e^{-\frac{2r^2}{\omega^2}}.$$

$$\left(r\frac{\partial}{\partial r}\right)T = -\frac{1}{\kappa}\frac{4\alpha P}{\pi\omega^2}\int r\sum_{n=0}^{\infty}(-1)^n\frac{\left(\frac{2r^2}{\omega^2}\right)^2}{n!}dr.$$

$$T(r) = \frac{\alpha P}{\pi\kappa}\sum_{j=1}^{\infty}\frac{(-1)^j\left(\frac{2r^2}{\omega^2}\right)^j}{jj!} + T_0.$$

$$\Delta T(r) = \frac{\alpha P}{\pi\kappa}\sum_{j=1}^{\infty}\frac{(-1)^j\left(\frac{2r^2}{\omega^2}\right)^j}{jj!}.$$

3.10

The details between step two and three are recorded in reference [16]. With only the Michelson or PRM on at 10 W to 30 W resonance thermal lensing is not great enough to induce problems. Nevertheless, this approximation is suitable for regions where beam sizes are far smaller than the optic they are passing through [16].

3.2.2 High Power Analytic Solutions for Finite Mirrors

P. Hello and J.-Y. Vinet constructed an analytical model for thermal aberrations and thermo-elastically induced distortion. The model extends the preceding solutions by incorporating the linearized radiation boundary condition, two dimensional time dependent thermal gradients, and is valid for larger beam sizes encountered in practical interferometers. This model separated the coating dissipation from the absorption in the substrate.

Fundamentally the model solves the Fourier heat equation (thermal diffusion equation) for both the static and transient cases. The latter is solved for a zero to thermally loaded case. Hello-Vinet chose to separate the case of bulk absorption and coating absorption to determine how each affected the thermal lens developed in a gravitational wave detector's optic.

This steady state model begins with the heat diffusion equation rewritten in terms of specific heat, C, optical material density, ρ, and thermal conductivity, κ.

$$\kappa \nabla^2 T = C\rho \frac{\partial T}{\partial t}.$$

3.11

Radiativity is written as

$$F = \sigma\left(T^4 - {T_{ext}}^4\right),$$

3.12

where σ is the Stefan-Boltzman constant, and T_{ext} is the external environment temperature.

This condition is linearized by Taylor expanding radiativity at the external temperature. The radiation condition becomes

$$F = 4\sigma' {T_{ext}}^3 \delta T.$$

3.13

Here, δTdescribes the minute difference in temperature. This expression is true for small temperature deviations above ambient levels, $\frac{T - T_{ext}}{T_{ext}} \ll 1$. The new static solution can be written as a sum of the auxiliary and particular equations, $T = T_{ext} - T_\infty$. Boundary conditions for the mirror barrel surface are

$$-\kappa \frac{\partial T_\infty(a, z)}{\partial r} = 4\sigma T_{ext}^3 T_\infty(a, z).$$

3.14

The HR and AR surface condition is written below respectively.

$$-\kappa \frac{\partial T_\infty\left(r, -\frac{h}{2}\right)}{\partial z} = \epsilon I(r) - 4\sigma T_{ext}^3 T_\infty\left(r, \frac{-h}{2}\right),$$

3.15

$$-\kappa \frac{\partial T_\infty\left(r, \frac{h}{2}\right)}{\partial z} = \epsilon I(r) - 4\sigma T_{ext}^3 T_\infty\left(r, \frac{h}{2}\right),$$

3.16

where ϵ refers to the material dependent emissivity.

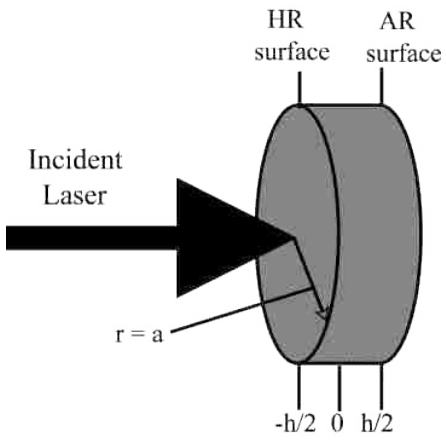

Figure 3-1: A sketch of the Hello-Vinet model. High power laser light is incident on the mirror's highly reflective (HR) coating. The mirror has a radius equal to "a" and a thickness equal to "h."

The solution to these boundary conditions is noted in Hello and Vinet's aberrations document [29]. The results are written in terms of the Dini series. General transient solutions are found using similar boundary conditions with the appropriate initial conditions. Here the important characteristic time equals $\frac{\rho C\, a^2}{\kappa}$. This denotes the approximate amount of time for heat to diffuse through a hemispherical volume on the HR side.

Heating by bulk absorption in the weakly absorbing and steady state condition is described analytically by the heat diffusion equation augmented by Beer's law [15, 19, 21, 22].

$$\mathrm{C}\rho\frac{\partial \mathrm{T}}{\partial \mathrm{t}} - \kappa\nabla^2\mathrm{T} = \alpha I(r). \qquad \textbf{3.17}$$

The solutions for thermo-elastic effects are found using similar assumptions about temperature profiles found in reference [29]. Results from both of these papers were used as benchmarks for numerical finite element simulations in chapter 5.

4 Numerical Packages and Tools

In this section, a pair of numerical tools is introduced. The first tool is a commercial FEM program used heavily in this dissertation's thermal analysis. The second tool is an in-house modeling software for determining the behavior of laser fields inside complex resonators. The need for these tools draws out of a necessity to quickly determine the approximate effects of complex phenomena not easily solved via analytical approaches.

4.1 COMSOL: Finite Element Analysis Tool

The most recent models of the LIGO mirrors are constructed in COMSOL, a commercially available finite element analysis/modeling (FEA or FEM) software from COMSOL Inc. [30]. This software's core is based on a partial differential equation toolbox provided by The Mathworks Inc.'s software MATLAB [31]. COMSOL's focal point is its capability to model multiple forms of physics simultaneously. For example, a piece of metal influenced by a time evolving magnetic field can be simulated to determine the induced heat load.

Modeling problems in COMSOL begins with the construction of a two-dimensional or three-dimensional geometry that defines physical boundaries of object to be modeled. The geometry can also be imported from an affiliated CAD program. If an object is singular, only its physical boundaries need to be drawn. If the objects are not embedded in a vacuum environment, a bounding box is typically installed to later represent the surrounding medium. More complex objects are drawn in sections and are mated using COMSOL's boundary identification. For example, a coffee cup sitting on a desk would have a shared area referred to as a "contact pair." This would allow the cup bottom to heat up through friction when slid across the desk. A camshaft comprised of 12 welded sections would be treated as a having "identity pairs." The composite camshaft parts do not grind against each other, but they can heat at different rates and share heat conduction surfaces.

The next series of steps involves the user indicating which materials are used and their location. Materials can be chosen from the COMSOL library or installed by the user. COMSOL permits the user to provide different materials for both the boundary and the substrate of an object. This provides the ability to model macroscopic objects with thin film coatings.

After picking materials, the user may install his/her own constants or use the library. COMSOL provides the most general governing partial differential equations for the various forms of physics. Boundary conditions and governing equations for the substrates and boundaries may be modified at the user's choosing. Parameters relying on phenomena internal to an object are also permitted to be encoded. Otherwise, default equations and constants are available.

The group of objects is next mapped using a mesh of nodes. The nodes represent the "elements" where physical evaluations are conducted. This motivates the term "finite element analysis/modeling." Depending on the number of objects, dimensions, and configurations a various methods of meshing are available. The uniform triangular mesh is chosen most often for this dissertation's simulations. If a more accurate simulation is required, a mesh's node density can be uniformly increased. Mesh size (density) is limited only by the available memory space and user patience. Therefore, whenever

possible it users may wish to exploit symmetries in the problem to reduce the number of dimensions. If precision is irrelevant in certain parts of a model compared to others, an adaptive of free mesh can be utilized. In this meshing scheme, the density of mesh points may be altered as the user sees fit.

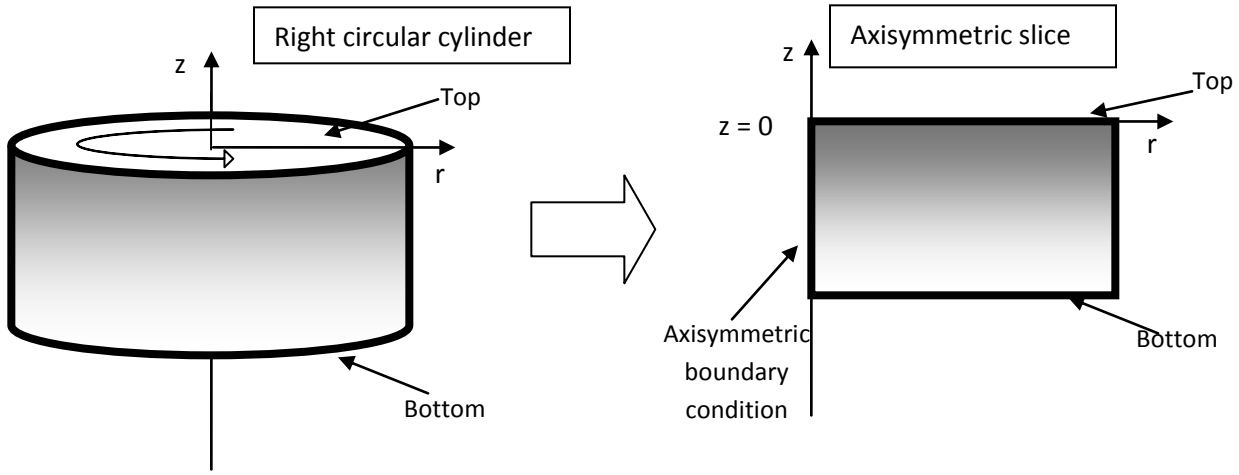

Figure 4-1: A diagram showing the reduction in degrees of model space. Switching from 3 dimensions to 2 dimensions increases the likelihood of an FEM's convergence for axisymmetric solutions. The picture on the left is an representation of a right circular cylinder. Should a problem be completely symmetric about the z axis, the problem can be represented as a 2 dimensional slice (right).

Next COMSOL requests the type of solution to be pursued. This asks whether the solution to be searched is static or transient, an eigenmode, or parametric. For transient and eigenmode solutions, animations can be created showing evolving behavior.

Finally, the solver is invoked. This first involves replacing the governing partial differential equations (PDEs) with ordinary differential equations. These ordinary differential equations are replaced during calculation by representative difference equations. The problem now becomes a matrix problem in which all nodes are represented. The matrix represents the set of linear equations affecting each node as well as its interactions with neighboring nodes. The default solver uses either the default SPOOLES direct approach; nine other solvers are available should this approach fail [30]. COMSOL also utilizes parallel processing algorithms. Therefore, multi-core processors are an advantage. Solutions can be plotted in a variety of methods depending on choice. For this dissertation, the used schemes are the color scheme and structural deflection.

For thermal problems as seen in this dissertation, the general FEM heat equation is written as follows:

$$\rho C\left(\frac{\partial T}{\partial t}+\left(\vec{u}\cdot\vec{\nabla}\right)T\right)=-\left(\overrightarrow{\nabla}\cdot\vec{\mathrm{q}}\right)+\boldsymbol{\tau}\colon\mathbb{S}\frac{T}{\rho}\frac{\partial\rho}{\partial T}(\mathfrak{A})+Q. \qquad \textbf{4.1}$$

$$\mathfrak{A}=\frac{\partial p}{\partial t}+\left(\overrightarrow{\mathrm{u}}\cdot\vec{\nabla}\right)p.$$

Here q stands for heat flux, ρ refers to material mass density, C stands for specific heat, Q equals the heat sources not included, u is the fluid velocity term, p is the fluid pressure term, and $\boldsymbol{\tau}\colon\mathbb{S}$ is the viscous stress tensor being multiplied by the strain rate tensor. Assuming that a solid exists in a vacuum, the

convection term and pressure term are irrelevant. In a system where vibrations do not result in heat, the strain and stress heat term can be removed. For a static solid, the Fourier heat equation is pertinent.

$$\vec{\nabla}T + \frac{q}{\kappa} = 0.$$

4.2

The resulting heat equation is shown below.

$$\rho C \frac{\partial T}{\partial t} + \vec{\nabla} \cdot \left(-\kappa \cdot \vec{\nabla}T\right) = Q.$$

4.3

Subscripts for each mesh node are left out of the equation for clarity since this equation affects every node in a thermal simulation.

For structures that may be in vacuum or convectively isolated, radiative boundary conditions are permitted. The outgoing radiative heat flux, radiosity, is comprised of a reflected term added to a black body emission term.

$$J = r_c G + \epsilon \sigma_{SB} T^4.$$

4.4

Where J is the radiosity; r_c is reflectivity; G represents the incoming heat flux; ϵ is emissivity; σ_{SB} is the Stefan-Boltzmann constant; and T is the material temperature. Since heat flux is the difference of incoming radiation and the radiosity. Since COMSOL treats reflectivity as related to that of ideal gray bodies, one minus the reflectivity equals the absorptivity as well as the emissivity. This is a simplification performed by COMSOL. Heat

$$q = (1 - \rho)G - \epsilon \sigma T^4;$$

$$= \epsilon (G - \sigma T^4).$$

If an object is surrounded by an infinite thermal bath, then the heat flux can be rewritten as follows:

$$q = \epsilon \sigma \left({T_{amb}}^4 - T^4 \right)$$

Where T_{amb} is the temperature of the thermal bath. Other objects involved in radiative heat analyses complicate the radiosity term through mutual irradiance. This is the incoming heat from other objects within the simulation. Radiosity is now written as shown below.

$$J = \rho (G_m + F_{amb}\, \sigma T^4) + \epsilon \sigma T^4.$$

4.5

Here G_m represents the mutual radiation arriving from other objects; the F_{amb} represents the "ambient view factor" or amount of "view from each point covered by ambient conditions" [30]

4.1.1 A Brief on Mesh Difference Formalism

The principle of FEM is to solve PDE's that could exist on complex domains, discontinuous domain, non-smooth transitions, or in regimes where variable precision is adequate. The method does not actually solve the PDE. In fact, FEM removes PDEs in favor of ordinary differential equations (ODEs) thereby yielding an approximation of the solution [30]. While this method may not yield exact solutions, it is often a means to quickly model a problem with complications. Further information regarding the full nature of COMSOL FEM processes can be found in the user manual hard copy or online at www.COMSOL.com [30]

4.2 Frequency-domain INterferomEter Simulation SoftwaRE (FINESSE)

Modeling the impact of a lens on a beam can be handled quite easily using Gaussian propagation techniques [19]. Modeling an axial Fabry-Perot cavity also can be done analytically and yield understandable results. However, the interaction of multiple resonators, with multiple longitudinal frequencies and transverse modes can become overwhelming. This type of book keeping is best left to numerical simulations. The program FINESSE version 0.99.8 is being built and maintained by Andreas Freise of the University of Birmingham, U.K. [32, 33]The present release is available at http://www.gwoptics.org/finesse/. Previous versions have been used to model interactions of the GEO and Virgo detectors [32, 33]

In order to model the interaction of fields in a complex resonator without overloading computer memory or over complicating the program, a few assumptions are made. The first assumption is that all objects in FINESSE are governed by linear relations. For example, laser gain media, aperture induced diffraction patterns, harmonic generators, and diffraction gratings are not possible. Second, FINESSE does not support polarization. Third frequency shifts are not explicitly computed. This entails Doppler induced sidebands due to mirror motions. All FINESSE based models are assumed to follow paraxial analysis used explicitly for Gaussian beam propagation such as those specific to the first two generations of interferometric gravitational wave detectors. Finally since Gaussian basis are typically spoken of in terms of Hermite (rectangular symmetry) and Laguerre (cylindrical symmetry) modes, FINESSE unconditionally restricts this choice to the Hermite basis [19-21].

A supplemental assumption states the laser's center frequency (the carrier) is 1064 nm. This assumption can be altered using the FINESSE configuration file. Another supplemental assumption states that the user must determine how many higher order modes to track. Excessive numbers of modes may not be productive, however too few may not yield valid results. When the user provided limit is exceeded, the energy going to modes beyond the limit are discarded from the model.

All optics, sources, and sensors are given component type designations. Each component is surrounding by one to four linking nodes depending on the component. These nodes tell FINESSE the overall layout of a group of optics.

Users begin by drawing the optical configuration and choosing reference names for optical components and their respective nodes with pen and paper. This diagram is then encoded into a layout text file using the aforementioned FINESSE specific encryption. At the end of the layout file, the user

specifies what variables are to be manipulated and how they are to be plotted. Once the layout file is complete, FINESSE is invoked.

The program initially checks the file for anomalies such as disconnected optics and incorrectly specified components. FINESSE then fabricates an interferometer matrix, $\mathbb{M}_{IFO}$, composed of local interaction matrices that govern each optic. A few local interaction matrices are shown in appendix B. The interferometer matrix is applied in the following manner:

$$\mathbb{M}_{IFO}\overrightarrow{x_{sol}} = \overrightarrow{x_{RHS}}. \qquad \textbf{4.6}$$

The right hand side vector, $\overrightarrow{x_{RHS}}$, contains all of the light sources. The solution vector, $\overrightarrow{x_{sol}}$, contains the output signals for each photodiode. Since the matrix is sparse, FINESSE uses the SPARSE matrix package to compute the solution vector [34]. If this does not yield results, the KLU matrix package can be invoked either automatically or as a forced option [35]. The results are assembled to generate a MATLAB readable file to display results [33]. An event log that contains user requested aspects is also generated. If an optical layout relies on modulation generated frequencies, FINESSE solves a separate interferometer matrix for each frequency. This merely improves computation time. The reader should note that FINESSE's base package does not provide for sideband on sideband modulation. Therefore a pair of first order phase modulators can only result in four new frequencies being added to the laser field. Results involving the interaction of frequencies are computed after the matrices are solved.

In order for FINESSE to successfully keep track of fields inside a resonator, two schedules for length are kept. The first schedule is the user imposed macro–length. Multi-centimeter to kilometer separations typically describes optical layouts. This number primarily accounts for beamsize, confocal phase (Gouy shift), and sideband interactions. It is also regarded as always being appropriate for carrier resonance unless otherwise indicated by the user. The second schedule tracks the microscopic tuning lengths at sub-wavelength resolution. This is typically written as a tuning phase in degrees. Three hundred sixty degrees equals one wavelength of carrier light. FINESSE also has options to turn off the automated resonance condition for the macroscopic lengths.

Modulators added to the layout file may be specified as being frequency, phase, or amplitude modulators with various options regarding modulation. These include modulation depth, order, and modulation frequency. Photodiodes can be paired with multiple mixers to generate demodulated signals. Unrealistic amplitude detectors can also be implemented to detect the absolute electric field amplitude of various frequencies and transverse modes. Spatial mode analysis also exists within the FINESSE architecture. This provides the ability to "look" at intensity patterns arriving at various ports. None of the photosensors in FINESSE are destructive.

When beams are not mode matched to optics or resonators that they intersect, FINESSE computes the TEM coupling coefficients. These coefficients describe how an initial Gaussian-beam parameter, q, is represented by the new beam parameter's basis. The example in the FINESSE manual writes this as an infinite series solution [36].

$$u_{nm}(q_1)e^{i(\omega t-kz)} = \sum_{n',m'} k_{n,m,n',m'} u_{n'm'}(q_2)\, e^{i(\omega t-kz')}$$

4.7

Here $u_{nm}(q_1)$ is an orthonormal Hermite-Gauss field injected into an optic. $u_{n'm'}(q_2)$ are the modes that represent the injected beam in the new portion of the beamline. This solution is essentially the representation given in chapter 2 with the exception of the extra indices used to track cross higher order mode contributions. The coupling coefficients $k_{n,m,n',m'}$ are computed by integrating overlap integrals over the surface of a phase front. Below, $\sin(\gamma)$ is added to demonstrate how misalignments in angle would be handled in FINESSE. γ represents the angle offset between the primed and unprimed modes' optical axes[33, 36].

$$k_{nmn'm'} = e^{i2kz'sin^2\left(\frac{\gamma}{2}\right)} \iint dx'dy' u_{n'm'} e^{ikx'sin\gamma}\, u^*_{nm}.$$

4.8

This strategy does become computationally expensive with large numbers of higher order modes. However, it does outline the method used by FINESSE. A faster approach is actually employed by FINESSE. This approach takes advantage of mismatch parameters detailed in reference[36] to partially solve the above integral.

Most interferometric gravitational wave detectors utilize electronic servos to keep their degrees of freedom within the resonance condition. FINESSE is capable of simulating simple servos based on a model derived discriminant. The extent of servo simulation, however, is only limited to optical responses. FINESSE does not include or have the capacity to simulate pendulum mechanics or the actual electronics. Therefore, the most simplistic integrator type servos are simulated. The accuracy of the servo motion is set by the user. A calibration test for a degree of freedom yields the derivative of power to optical phase. This derivative is referred to as "optical gain" in the realm of gravitational wave interferometry. The accuracy of a servo in power units can then be computed by the root mean square motion times the calibration. If FINESSE's servo subroutines exceed the user specified accuracy thresholds, the servo is considered to have failed. All failed servo points are noted in the event log as per user request.

Since FINESSE performs calculations in the frequency domain, the servos do not alter mirror positions in a time evolving fashion. Rather zero finding algorithms search try to keep the servoed signal within user provided accuracies by moving controlled optics before recalculating fields and the servo signal. If the servo subroutines determine that the user provided optical gain is too large or too small, an autogain function is invoked to alter the optical gain in hopes of improving the likelihood of finding a solution. For simulations that require multiple servos, FINESSE provides the option to run the servos in parallel or in a turn-by-turn fashion. The decision is based on computational stability. Further details for servos are found in FINESSE's manual[33].

On occasions when users wish to design non-ideal, non-library optics, FINESSE's newest package adds this ability. Optics (mirrors or glass slabs) can be granted two dimensional phase maps to study thermal

lensing. Reflectivity and absorption maps can be added to evaluate non-uniform mirror coatings. The notation for a user implemented transmission phase map is shown in equation 4.9.

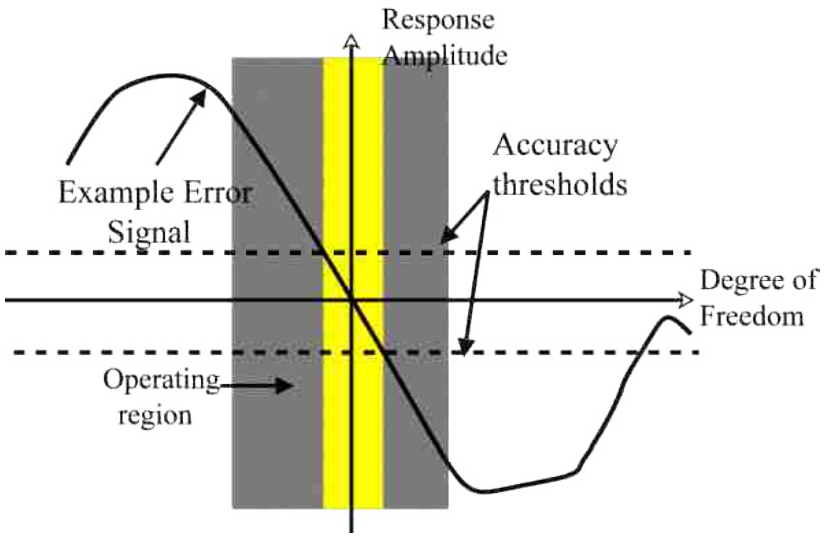

Figure 4-2: A cartoon representation of a discriminant signal useful in FINESSE. The signal crosses zero as a linear function. The region highlighted in yellow is the operating region where the servo remains within user prescribed accuracy thresholds. The error (discriminant) signal remains linear throughout the gray region. In this region, FINESSE would not need to recompute the optical gain.

$$A(x,y) = e^{-i2k(n_1-n_2)B(x,y)}. \tag{4.9}$$

Reflection phase maps are similar and are shown.

$$A(x,y) = e^{i2kn_1B(x,y)}. \tag{4.10}$$

The n_1 and n_2 are the index of refraction before and after the surface map respectively; k refers to wavenumber; and $B(x,y)$ is the user entered phase map represented as a matrix of real numbers in a text file. This feature is invaluable for studying thermal effects on the iLIGO interferometer in this dissertation.

5 ITM and Interferometer Modeling Construction

This chapter discusses the construction of two simulations using tools mentioned in chapter 4. The first simulation discussed is the development of a representative FEM model of the ITMs that agrees with Hello and Vinet's analysis. The analytic comparison code was written by P. Willems of California Institute of Technology's LIGO Lab in 2007. The FEM's primary purpose is elaborated in chapter 6. The second model used FINESSE to develop a model of the full interferometer. Optical components of the interferometer and FINESSE packages were tested separately and are shown in this chapter.

5.1 ITM FEM Physical Parameters

On a few occasions within this dissertation, the basic parameters for an ITM have been outlined. Table 5-1 presents the physical parameters representing an ITM. The Lamé coefficients are gleaned from reference [37]. Lamé parameters are two parameters used in linear elasticity theory of solids.

Table 5-1: A table of material parameters for a fused silica test mass. Notice the thermal dependence of the Young's modulus and Poisson ratio. These values were obtained from fitting experiment results carried out in Rome, Italy.

Parameter Name	Value
Geometry	Right Circular Cylinder
Diameter	0.25 m
Thickness	0.10 m
Density	2203 kg
Specific Heat	740 J/(kg K)
Emissivity	0.89
Thermal expansion coefficient	0.55 ppm/K
Thermal conductivity	1.38 W/(m K)
Index of refraction	1.44963
Young's modulus	$E=E_0+E_1T+E_2T^2$
E_0	$6.760244875\cdot10^{10}$ Pa
E_1	$2.545\cdot10^{7}$ Pa/K
E_2	$-2.195\cdot10^{4}$ Pa/K^2
Poisson's ratio	$v=v_0+v_1T+v_2T^2$
v_0	0.1411124157
v_1	$1.0231\cdot10^{-4}$ 1/K
v_2	$-8.4388\cdot10^{-8}$ 1/K^2
Lamé coefficient 1	$1.56 \times 10^{10}\,\mathrm{J\,m^{-3}}$
Lamé coefficient 2	$3.13 \times 10^{10}\,\mathrm{J\,m^{-3}}$
Environment Temperature	300 K
Laser radius at LLO ITM	0.0387 m

Physically the ITMs are not right circular cylinders. Their highly reflective surfaces are spherically curved at approximately 14 km giving them a micron level meniscus. This spherical "defect" can be

reproduced in most computer aided modeling (CAD) programs. Since COMSOL cannot directly import CAD models with such a small meniscus, the COMSOL converters replace the true mirror form with right circular cylinders without errors. Later in this dissertation, the lack of a spherical "defect" is shown to be irrelevant.

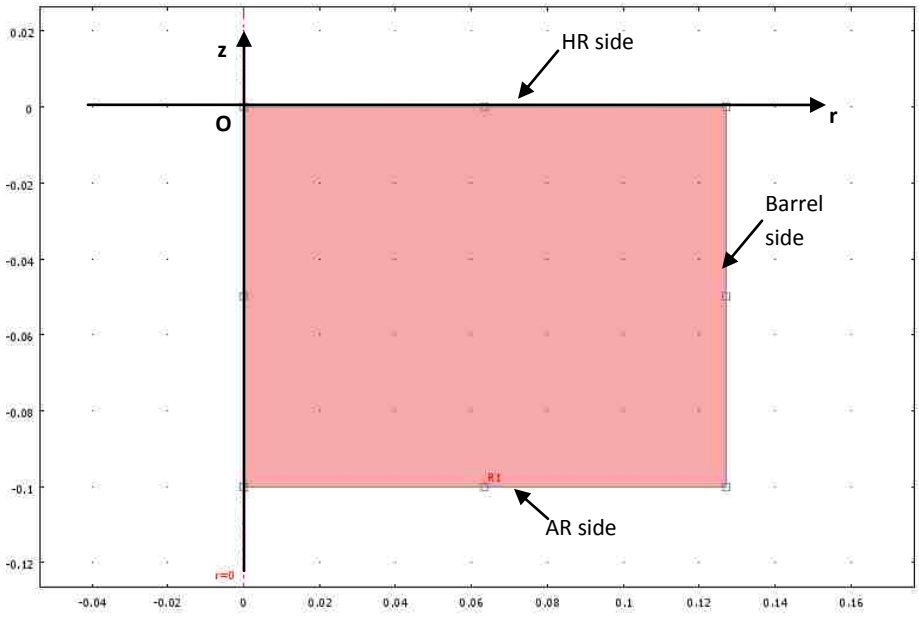

Figure 5-1: A radial cross section view of the COMSOL model. The horizontal axis represents the radial coordinate. The vertical axis describes mirror thickness. Coordinate z = 0 and r = 0 are located at the center of the highly reflective surface. HR and AR represent the highly reflective and anti-reflective coated faces.

The coordinate scheme for the COMSOL model is plotted in Figure 5-1. The axisymmetric model profile was chosen to improve FEM solver precision and likelihood of convergence as mentioned in chapter 4. Respectively, the Hello-Vinet model coordinate origin rests in the center of the mirror (see Figure 3-1). Neither model presented attempts to simulate stress induced by suspension wires or wire stand-offs.

Since iLIGO and eLIGO incorporated only Gaussian laser modes, the FEM heat source was also set to match the Nd:YAG beam both on the HR surface as well as within the substrate. Figure 5-2 plots the consistency between the static Hello-Vinet solution with only surface heating and its counterpart FEM. Figure 5-2 plots temperature versus radial coordinate. The solid curves represent the analytic solution at the highly reflective surface, mid-optic, and the anti-reflective surface. The dotted lines represent estimations generated by the FEM solution throughout the material. From this plot, one can conclude that the FEM corresponds to the theoretical surface diffusion almost identically.

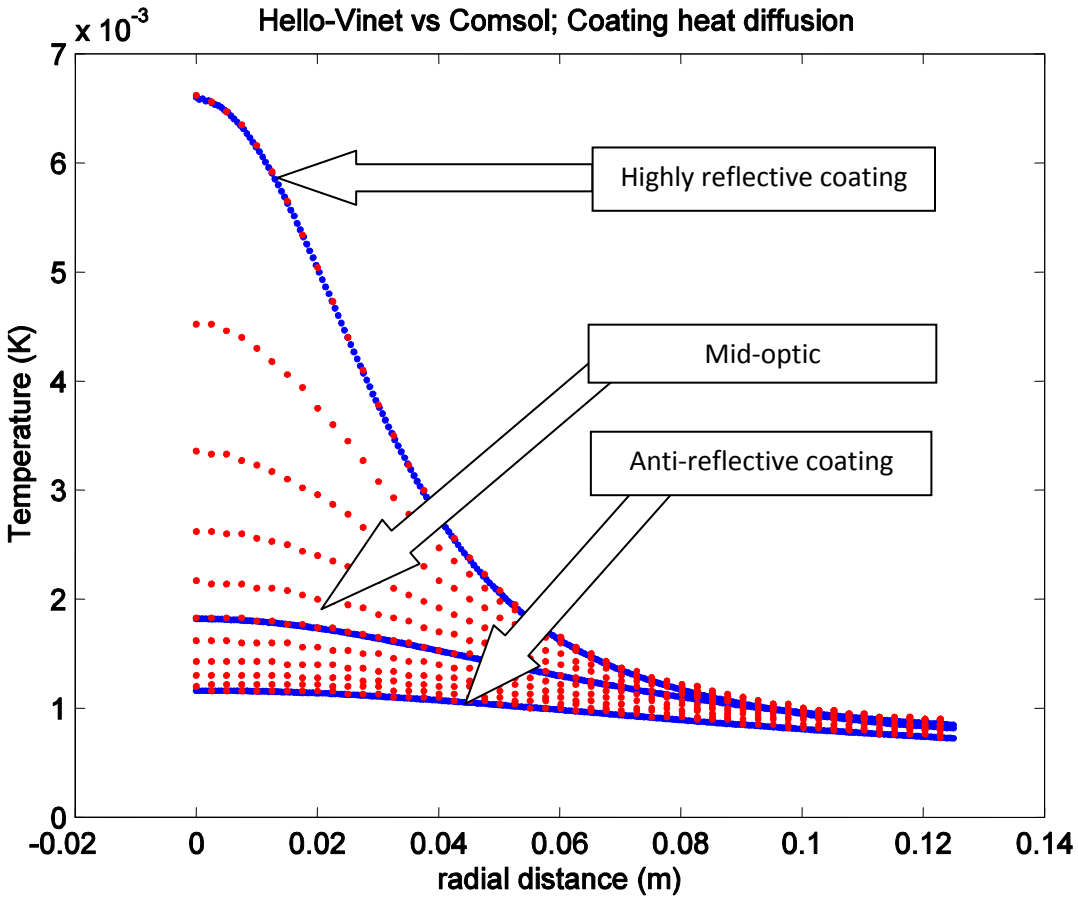

Figure 5-2: A benchmark test comparing COMSOL's FEM solution to Hello-Vinet's analytic model for substrate heating. The abscissa marks the radial distance from the center of the optic. The ordinate marks temperature variations from 300 K, the ambient temperature. Analytic model simulations are plotted in blue. FEM solutions are plotted in red. The three analytic solutions plotted correspond to the high reflective coating, mid-optic, and the anti-reflective coating. FEM curves overlap nearly identically.

5.2 Transient Deformation

The preceding curves in Figure 5-2 demonstrated the equivalence in calculating a static thermal diffusion wave. The next stage tests transient solutions. Figure 5-3 displays a thermal wave propagating after 2.4 million seconds. Based on the static result, the curves should perfectly overlap. What is of consequence is the FEM's ability to compare satisfactorily with an analytical means in this regime. The FEM should progressively solve the thermal gradient with environmental interactions.

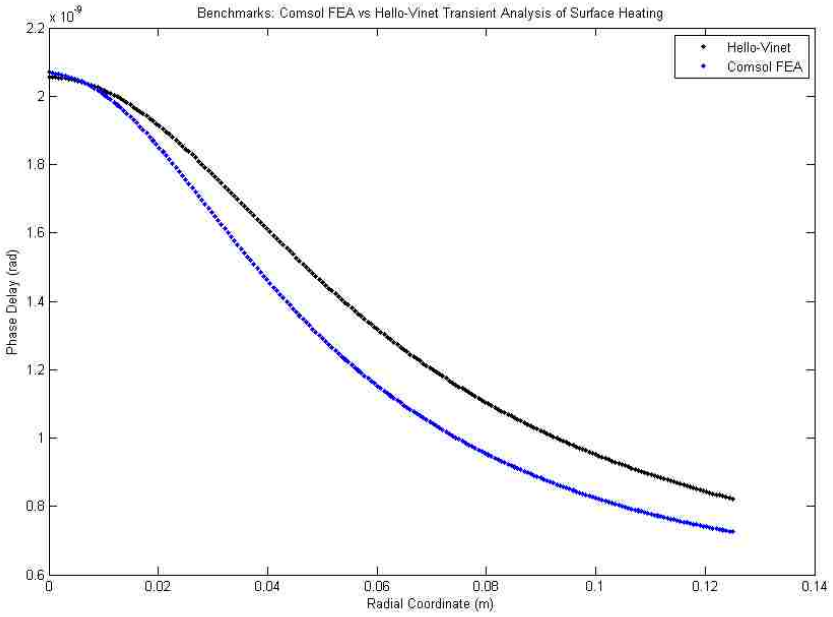

Figure 5-3: A comparison of transient heating induced phase delays using FEA and Hello-Vinet algorithms. The abscissa represents the radial coordinate of the optic. The ordinate represents the thermally induced phase delay in units of radians. The discrepancy comes from a square root of two missing in the Hello-Vinet model's simulation.

The discrepancy in the above comparison is believed to be due a missing square root of 2 in the analytical model. Since the analytical code was never updated, the extent of improvement remains to be determined. Figure 5-4 plots the ratio of the two solutions and indicates that the largest discrepancy rounds to 16 percent.

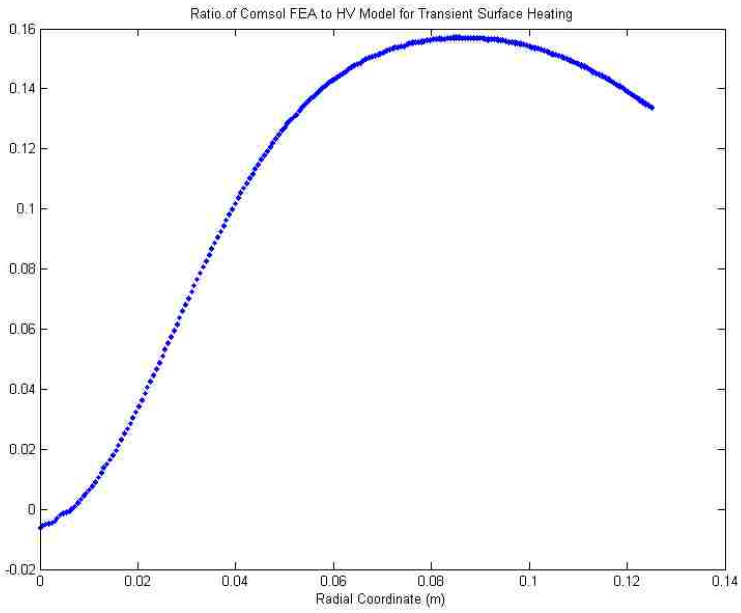

Figure 5-4: Ratio of FEM to analytic model discrepancy. Phase delay error does not exceed five percent within irradiated region.

5.3 HR Surface Deformation

The next benchmark compares how the numerical program simulates highly reflective surface deformation, Figure 5-5. We immediately see that the deformation computed by the FEM matches the analytical solution to within a couple percent. The slight overestimate near the center is due to empirically measured thermally dependent Young's and Poisson ratios in the FEM.

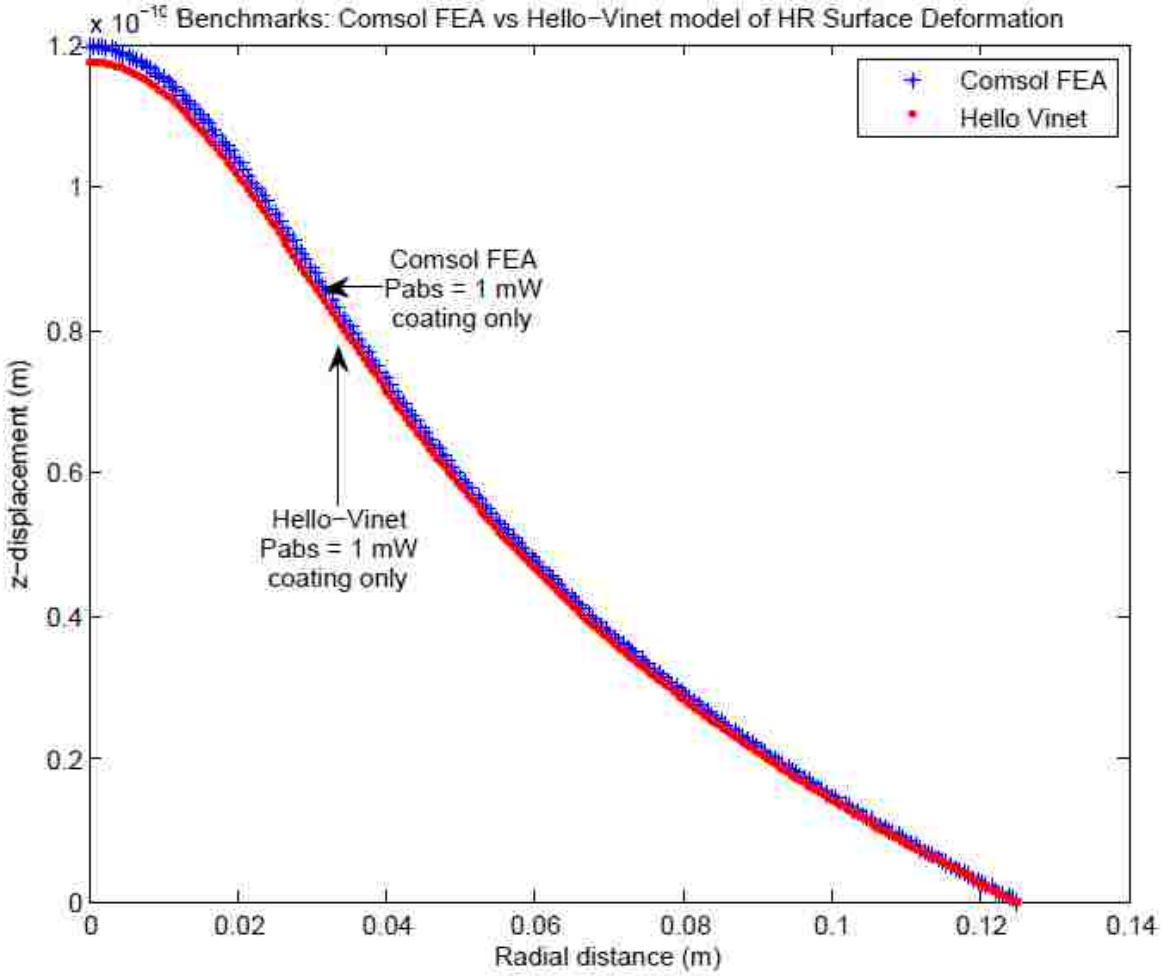

Figure 5-5: A plot comparing the highly reflective surface deformation solutions. . The abscissa charts the radial coordinate of the optic. The ordinate charts the surface displacement along the optical axis. The FEM result is presented in blue. The analytic result is presented in red. The FEM overlaps the analytic solution to within a couple percent

Similarly, a comparison between the anti-reflective surface deformations can be drawn. Unfortunately, in this case there is a larger discrepancy. Figure 5-6 tells indicates how poorly the FEM correlates to analytical model. This is not an outright failure of the FEM. The reader should note the order of magnitude of deformations is ~ 1 Angstrom. This may have also been the result of material pinning to the coordinate grid. The lack of flex could also be motivated by the use of different Poission ratio and Young's modulus for both the FEM and analytic model. This point has not been resolved. Rather the FEM successfully indicates the lack of deformation at the anti-reflective surface. Figure 5-6 indicates that the bowing due to the induced thermal gradient would cause a magnitude lower bowing in the optic.

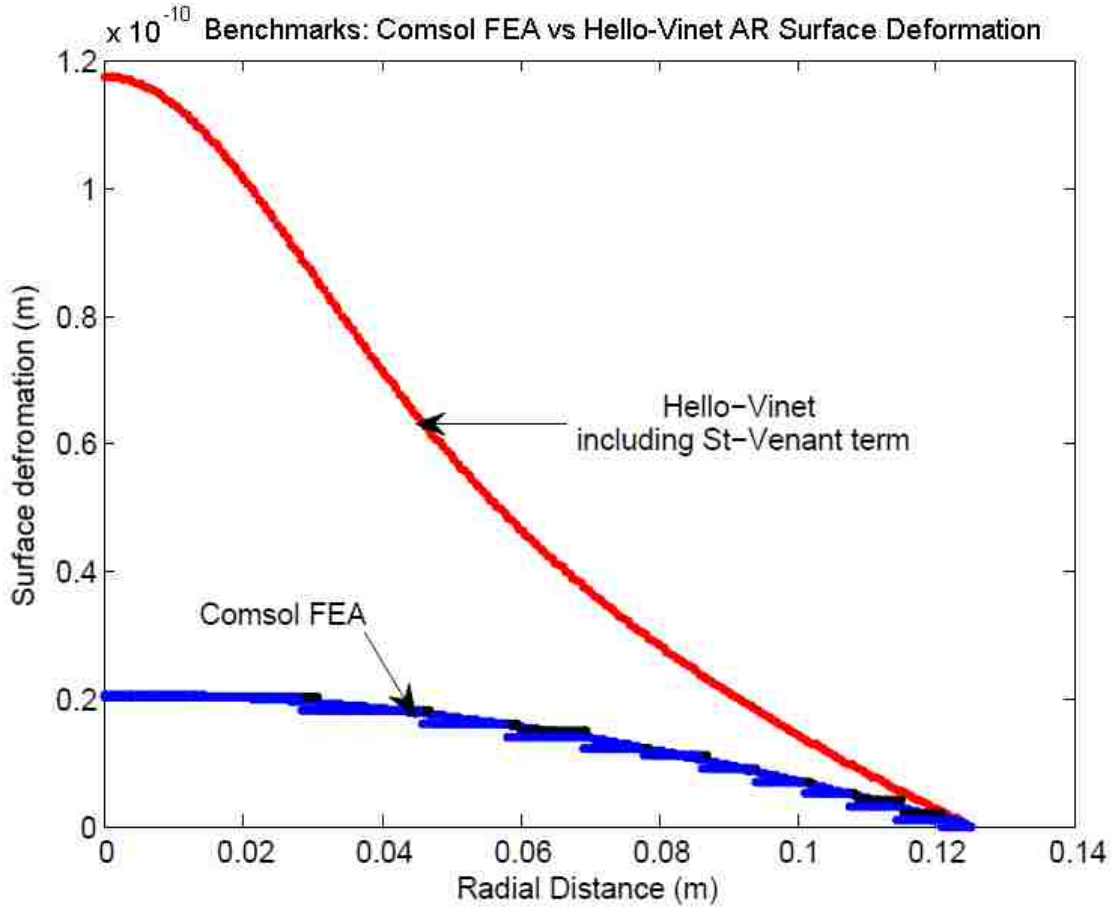

Figure 5-6: The deformation of the anti-reflective surface of a nominally sized LIGO optic. The ordinate indicates the displacement of the mirror's anti-reflective surface. The abscissa indicates the radial coordinate. It is noteworthy that the FEA lags the analytical model by an angstrom. Due to the minuteness of curvature, the antireflective distortion is irrelevant.

5.4 Body Mode Frequency Comparison

A comparison was performed using the COMSOL FEM, the Ideas FEM package, and the measured resonance lines of the ITMs. The first column in Table 5-2 shows estimates from a FEM build using Ideas [38]. Column two lists eigenfrequencies from the author's COMSOL FEM. Column three shows data taken at the Livingston detector. Discrepancies between the FEMs and measurement were believed to be the result of accounting failures for mirror suspension, the slight wedging, mass subtleties, and possibly different solution schemes.

Table 5-2: Comparison of two simulations versus actual body mode frequencies.

Mode name	Ideas model (Hz)	COMSOL (Hz)	Meas (Hz)
saddle/butterfly	6641	6823	7056
drumhead	9299	9536	9325
breathing	14489	14488	14367

5.5 Interferometer Components in FINESSE

This subsection tests basic operationality of interferometer components built in FINESSE. The first set of examples test FINESEE's beam parameter propagation capacity. This is followed by the simulation of Fabry-Perot cavities and their principles of operation. Then results of FINESSE's evaluation of a simple Michelson interferometer are shown. Finally, a model of a power recycled interferometer is constructed and evaluated for congruence with measurements.

5.5.1 Choosing the Frequency Domain Model

A question arises whenever choosing between frequency domain models and Fourier transform models. The question asks whether or not the frequency domain based models are appropriate for use in modeling phase front aberrations. This question effectively needs to be specified further by asking the level of detail we need and the level of detail we imagine we need. Colloquially this was also phased, "how patient are you?" A Fourier domain program such as the "Stationary Interferometer Simulator" ("SIS") and its predecessors broke optics into 128 sample bins in the vertical and horizontal directions across the face of an optic [39]. This provides "SIS" the ability to resolve one-tenth of a centimeter scale phenomena. This is fair for small surface feature effects like those caused by poor mirror grinding or excessive point heating. Frequency domain programs, however, must have the "maximum modal" order set prior to computation. The results for using too few modes can results in poor sampling.

Effectively, thermal effects propagate throughout the bulk of a material as long as the "hot" spot remains of reasonable size. Therefore, a heated zone 2.5 centimeters in size will eventually grow in size. To sample the initial effects of an annulus with a 2.5 centimeter thickness, frequency domain simulators will require a "maximum mode" number of $n + m = 39$. A maximum mode number of 12 yields a spatial resolution of approximately 4.45 centimeters, while a maximum mode number of 8 has a resolution of nearly 5.5 centimeters. On the opposite side of the spectrum 1 centimeter resolution would require a maximum mode number of 240.

Thermal effects need at least at maximum modal number equal to 8. Increasing this number to 12 will improve results and increase computation time between 5 to 8 fold. Forty modes in FINESSE will drastically increase simulation time to overnight timescales.

FINESSE presents another aspect than just performance time. FINESSE is capable of computing transfer functions attributed to the modeled optics. Neither SIS nor its predecessors are able to determine how fields behave when excited by an optic. This feature was tested by the Virgo group in Cascina, Italy although results have not been posted.

5.5.2 Beam Propagation

Begin first with proofs of FINESSE lenses ability and the capacity for transmissive phase maps. All Gaussian lasers can be described by a beam parameter, "q." Further details regarding this parameter are in appendix A . This beam parameter is a ratio of the laser beam waist squared and the light's wavelength.

$$q_0 = \frac{i\pi\omega_0^2}{\lambda}.$$

5.1

Ultimately this represents one half the collimation distance of the laser beam, the "Rayleigh range." Once a beam parameter has been determined for a light source, it can be propagated through a set of optics comprised of lenses, mirrors, free space, fiber optics, and even active optical components. Such computations involve simple two dimensional matrices. Called "ABCD" matrices, they are applied to the beam parameter as follows:

$$q_1 = \frac{Aq_0 + B}{Cq_0 + D}.$$

5.2

The representation of most optical elements can be found in references [15, 20, 21, 24] and [19]. More detailed lists may be found in references[15], [19], and [24]. Nonetheless, the solution for a simple free space propagation, documented in numerous resources is reproduced here.

$$q_1 = q_0 + L.$$

5.3

Where:
L = the distance of free space propagation,
q_0 = the Gaussian beam parameter expressed at the waist,
q_1 = the Gaussian beam parameter expressed following the affect of the matrix.
The beam spot size can be computed from the beam parameter following Fox and Li's prescription noted in reference [19] and many other resources [4, 15, 18, 20, 21, 24].

$$\omega(z) = \omega_0 \sqrt{1 - \left(\frac{z - z_0}{z_R}\right)^2}.$$

5.4

Where:
z_0 = the waist initial position on the z-axis coordinate,
z = the distance of propagation,
z_R = the Rayleigh range,
ω_0 = waist size,
$\omega(z)$ = beam spot size (radial size).

Figure 5-7 plots a simple comparison between analytical beam propagation and the result of FINESSE under identical assumptions.

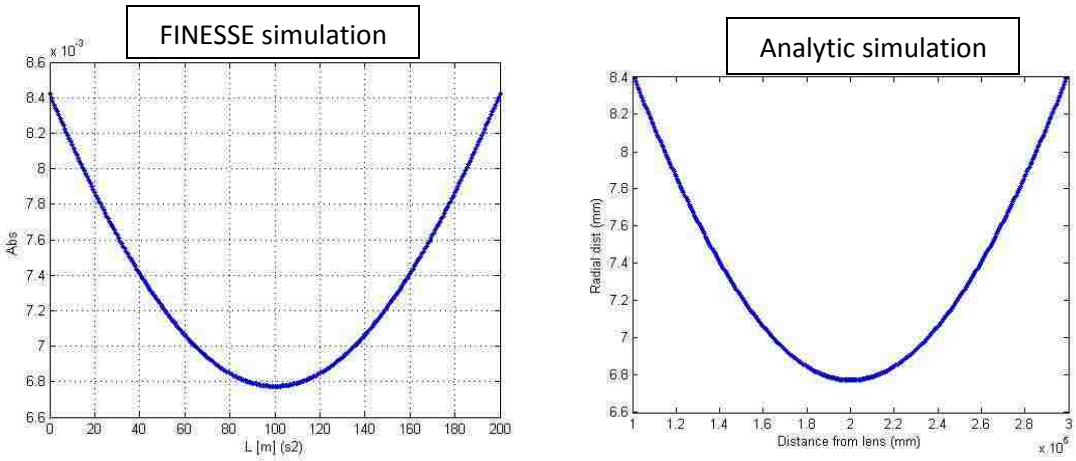

Figure 5-7: Side by-side comparison of FINESSE basic beam propagation to analytical beam propagation using beam parameters. One can see with that the two figures are identical. The ordinate stands for distance from an optic. The abscissa stands for spot size in meters on the left and millimeters on the right. The right plot was displaced by 1 meter. Both lines overlap each other perfectly when the plots be superimposed.

The method for plotting a phase map on a beam is given a cursory explanation in chapter 4. Remember this is the same formalism used for a spherical lens's acting on a beam. A Gaussian beam that is propagated several kilometers should remain Gaussian. A lens acting on such a beam should effect the amplitude distribution but leave the Gaussian envelope intact. Furthermore, a standard spherical lens provides a quadratic phase delay [19]. Replicating the phase map of a spherical lens and applying it to a slab of glass should generate the same effect. Below Figure 5-8 and Figure 5-9 confirm FINESSE's phase map capacity.

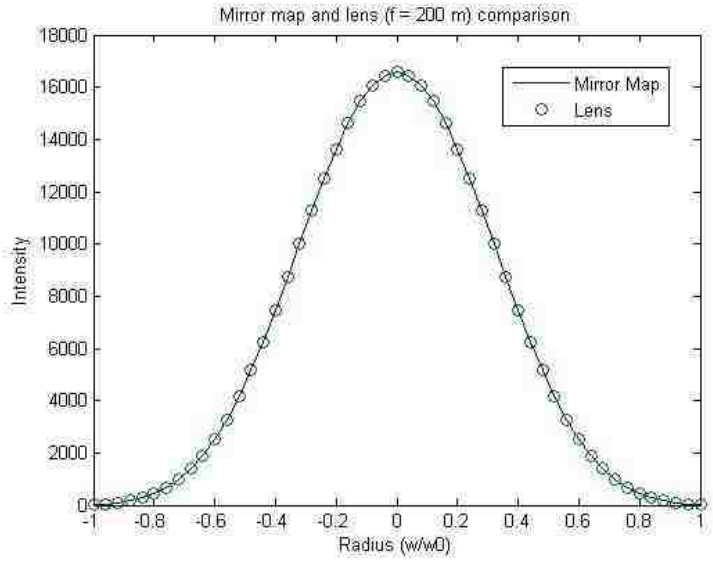

Figure 5-8: Demonstration of equivalence. The abscissa indicates beam spot radius with respect to the original waist. The ordinate indicates beam intensity in Watts per square centimeter. The circles indicate the intensity profile of a beam that has propagated through a 200 m lens. The solid line indicates the same beam propagated through a flat slab of glass, a transparent "mirror." This slab is granted the phase delay characteristics of a 200 m lens. Subtraction between the two curves yields zero to within numerical precision.

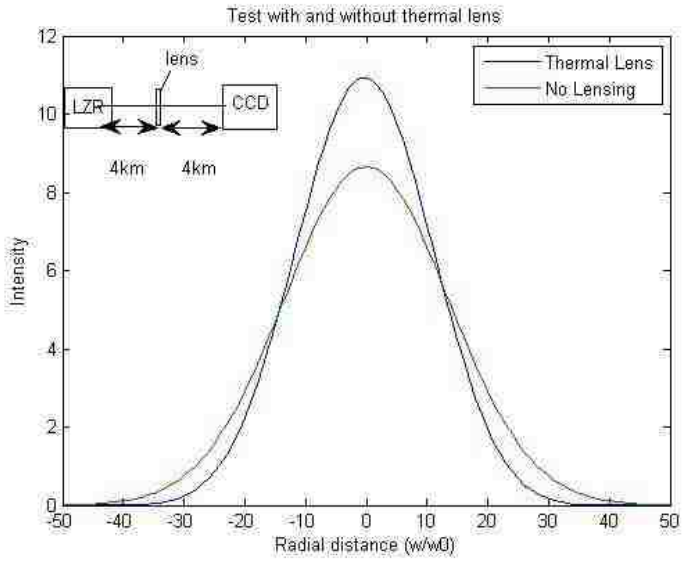

Figure 5-9: Effects of a positive lens or phase map on a propagated beam. The abscissa indicates relative radial distance. The ordinate indicates intensity in Watts per square centimeter. The green curve plots the intensity pattern of a un-lensed beam. The blue curve indicates that a phase delay mimicking a positive lens correctly tightens the pattern.

5.5.3 Fabry-Perot Interferometers Fringe Response

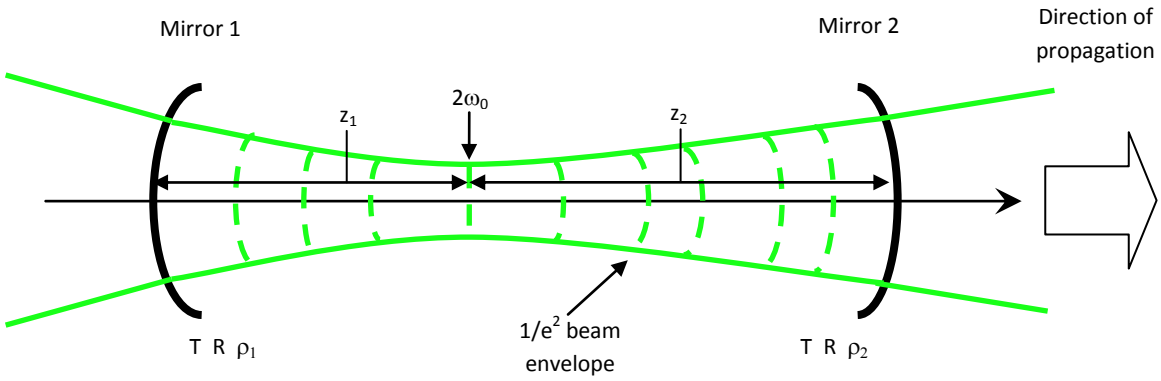

Figure 5-10: A diagram of a Fabry-Perot interferometer. The interferometer (resonator or cavity) is comprised of two mirrors that contain light between them. Mirror 1 and mirror 2 have the same transmission and reflection coefficient, T and R respectively. The mirrors have curvatures ρ_1 and ρ_2. Curved mirrors resulting in stability parameters below 1 permit field containment. The beam envelope is classically noted as the e^{-2}. ω_0 represents the beam waist, the point of narrowest focus. z_1 and z_2 represent the distance from the waist to each mirror. Light fields on resonance reflect between the mirrors and regenerate their wavefront profiles exactly upon each pass. Because the light field moves from left to right mirror 1 is called the input coupler. Mirror 2 is called the output coupler.

At this juncture, the simulated LIGO base components are assembled and tested beginning with the Fabry-Perot arm cavities. The basic physics of an axial Fabry-Perot interferometer (Figure 5-10) is described in references [15, 18-22, 24, 25]. More detailed discussions regarding the physics of suspended Fabry-Perot cavity dynamics can be found in reference [40]. Again, FINESSE does not include all the dynamics discussed in the aforementioned dissertation. FINESSE focuses on the static and dynamic effects on light due to passive optics. Therefore, a simple Fabry-Perot interferometer can be

readily simulated assuming infinite mirrors and infinitely stable mirror mounts only available in computer space.

An axial Fabry-Perot interferometer is comprised of two mirrors both of which are curved in such a fashion as to contain light in both a longitudinal and transverse sense. The round trip distance between these mirrors equals an integer number of wavelengths. This ensures constructive interference. The cavity stability parameter dictates a cavity's transverse containment and is first introduced in chapter 2 equation 2.18. FINESSE computes the Gaussian beam parameter, if a cavity is stable. A laser using this target q will be perfectly mode matched to the Fabry-Perot cavity. An injected laser field consisting of a central carrier frequency and first order phase modulated sidebands can then be propagated into the cavity. Moving one of the mirrors results in an optical frequency or a fringe sweep.

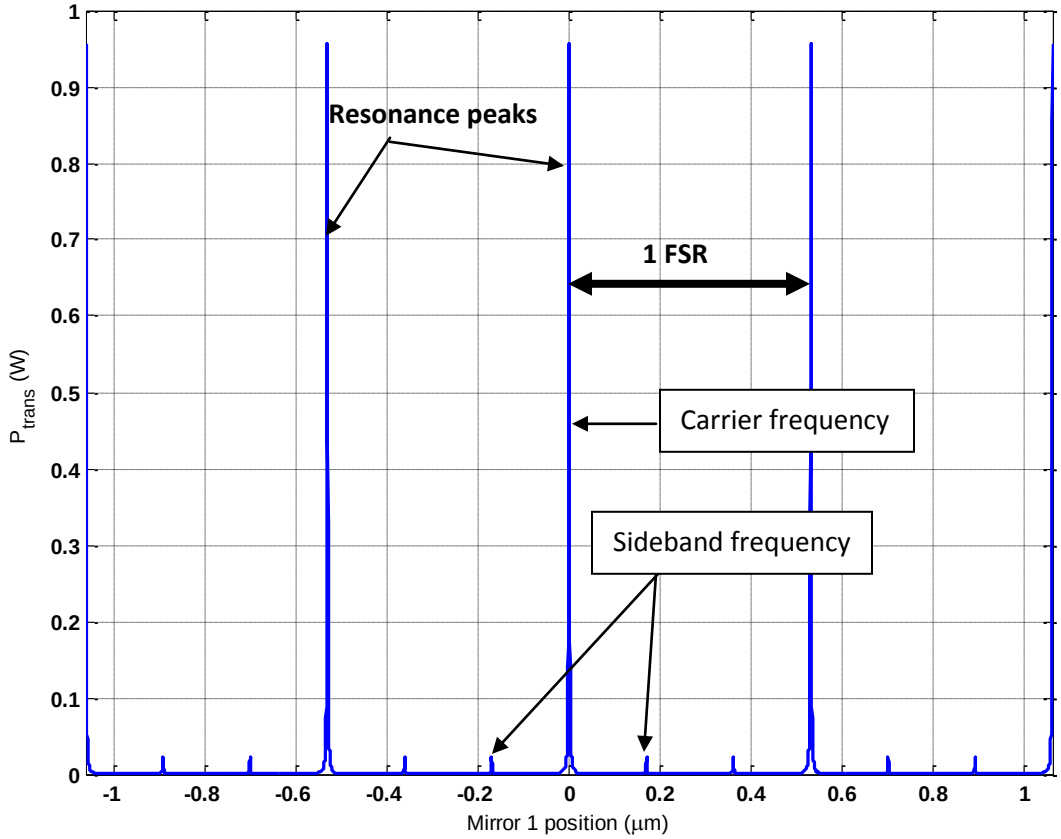

Figure 5-11: A simulation of transmitted light intensity through a flat-curved Fabry-Perot interferometer fringe sweep. The vertical axis indicates power transmitted through the rear mirror. The horizontal axis represents mirror 1's position in micrometers. Each identical resonance peak is separated in longitudinal frequency by 1 free spectral range (FSR). The FSR corresponds to the beat frequency of the cavity due to light circulation time, $c/(roundtrip\ distance)$. The large peaks correspond to the central light field which has phase modulated sidebands (smaller peaks) impressed on it. The injected beam was mode matched to the Fabry-Perot cavity resulting in only three peaks per FSR.

Figure 5-11 plots the transmission of a Fabry-Perot interferometer whose input mirror and output mirror had identical reflection and transmission values. One Watt was being injected into the interferometer; the vertical axis represents transmitted power. The horizontal axis describes output

mirror's position. Mirror position was be converted into cavity beat frequency units, by $\frac{\lambda}{2} = 1\ \mathrm{FSR}$. Horizontal positions of the peaks indicate particular modal excitations similar to **Error! Reference source ot found.**. Three peaks are visible per FSR because the input laser light has phase modulated sidebands impressed on it. Fringe sweeps are methods of determining the frequency and transverse content of the light injected. One should notice that a simple Fabry-Perot cavity always has a symmetric fringe/dispersion pattern.

5.5.4 Phase Discriminant Based Length Control

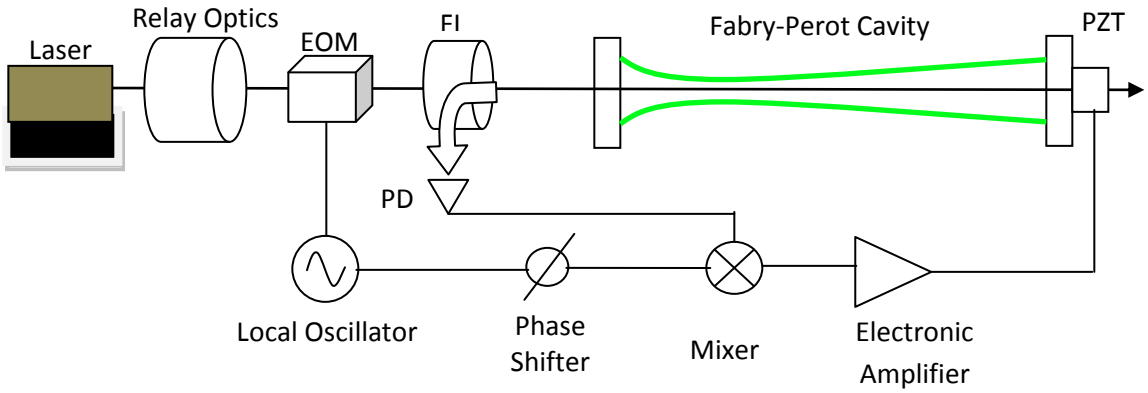

Figure 5-12: A diagram of a simple Pound-Drever-Hall locking scheme. The laser sends nearly monochromatic light into a set of relay optics that focus light into a electro-optic modulator (EOM). The EOM modulates the phase of the laser light. This induces the sidebands, the additional laser colors. If the Fabry-Perot cavity resonant with the carrier, the sidebands reflect off the first mirror. A Faraday isolator (FI) acts like an optical diode and routes reflected light to a photodetector (PD). The reflected light consisting of the sideband light and the carrier light reflected off the front mirror result in an amplitude modulated photocurrent. This electrical signal is mixed with the orginal drive signal from the local oscillator (LO) to create an error signal. An amplifier appropriately drives an actuator (PZT) based on this electronic signal keeping the cavity on resonance.

To hold the interferometer on resonance, off resonance, or anywhere in between, the sideband's beat with the carrier light can be exploited. This method is named Pound-Drever-Hall (PDH) scheme and is mentioned in the introduction [41, 42]. The reflected light from a Fabry-Perot cavity is a mixture of sideband and carrier light. Demodulating this reflected signal with the original oscillation frequency results in a real and imaginary term also called in-phase and quadrature phase respectively. If the demodulation phase is optimized for one particular value, the complimentary demodulation term will be minimized in slope as indicated in Figure 5-13. The result is an error signal whose optimal operating point is typically at the zero crossing. Below is a basic example of the PDH locking and its application in FINESSE [33] using FINESSE's notation. Begin by assuming a plane wave electromagnetic wave has an amplitude E_0. Γ and Ω equals the phase modulation depth and modulation frequency respectively. J_k is the k[th] first order Bessel function.

$$E(x,t) = E_0 e^{i\omega t + i\Gamma \cos(\Omega t)} \tag{5.5}$$

$$= E_0 e^{i\omega t} \sum_k i^k J_k(\Gamma) e^{ik\Omega t} \tag{5.6}$$

$$= E_0 e^{i\omega t}\left[1 + i\frac{\Gamma}{2}\left(e^{i\Omega t} - e^{-i\Omega t}\right)\right].$$

5.7

The DC component of this signal is,

$$S_0 = E^* \cdot E$$

$$= \sum_j \sum_k a_j a_k^* e^{i(\omega_j - \omega_k)t},$$

5.8

where a represent the amplitude coefficients of component frequencies ω. Again, the light reflected off the cavity is a combination of carrier and sideband light. The cavity's amplitude reflection coefficient has been omitted for calculation clarity. Multiplying the DC component above by a cosine yields the demodulated signals. Here the arguments of the cosine correspond to the oscillation frequency of the local oscillator, ω_{loc}, in Figure 5-12 and the local phase of demodulation, ϕ_{loc}.

$$S_1 = S_0 \cos(\omega_{loc} t + \phi_{loc})$$

5.9

$$= \frac{S_0}{2}\left(e^{i\omega_{loc} t + i\phi_{loc}} + e^{-i\omega_{loc} t - i\phi_{loc}}\right)$$

$$= \sum_j \sum_k a_j a_k^* e^{i(\omega_j - \omega_k)t}\left(\frac{\left(e^{i\omega_{loc} t + i\phi_{loc}} + e^{-i\omega_{loc} t - i\phi_{loc}}\right)}{2}\right)$$

$$= \frac{1}{2}\left(\sum_{j=0}^{N} a_j a_j^* + \sum_{j=0}^{N}\sum_{k=1+j}^{N}\left(a_j a_k^* e^{i\omega_{jk} t} + a_j^* a_k e^{-i\omega_{jk} t}\right)\right)\left(e^{i\omega_{loc} t + i\phi_{loc}} + e^{-i\omega_{loc} t - i\phi_{loc}}\right).$$

5.10

The DC components leave the following:

$$S_{1,DC} = \frac{1}{2}\sum_j^N \sum_k^N (a_i a_j^* e^{i\phi_{loc}} - a_i^* a_j e^{i\phi_{loc}}).$$

5.11

The in-phase term corresponds to the real component or cosine term of this equation. The in-quadrature phase corresponds to the imaginary term or sine component of this equation. In this presentation, there is no time variance in phase nor has the reflectivity coefficient of an interferometer (cavity) been added. An alternate formalism inclusive of the Fabry-Perot interferometer reflectivity is given by reference [42].

Figure 5-13 depicts the mixer signal results, the demodulated terms. One can see the local phase has been set to provide maximum slope to the in-phase signal. In the other case, the in-quadrature term has been minimized in response. The resulting simulation signals are classic locking discriminants found in analytic formalisms.

Readers should notice the result here does not account for transverse amplitude distributions. When one includes higher order mode structure, the result is a corrupted locking discriminant. Chapter 8 expounds on this detail.

The FSR of the LIGO Livingston Fabry-Perot arm cavities is 37.5 kHz. The spot size on the ITMx is roughly 3.87 cm with an intra-arm waist of roughly 3.5 cm. This numbers can be computed using the cavity stability parameters. Further, they correspond quite well to the FINESSE numerical model.

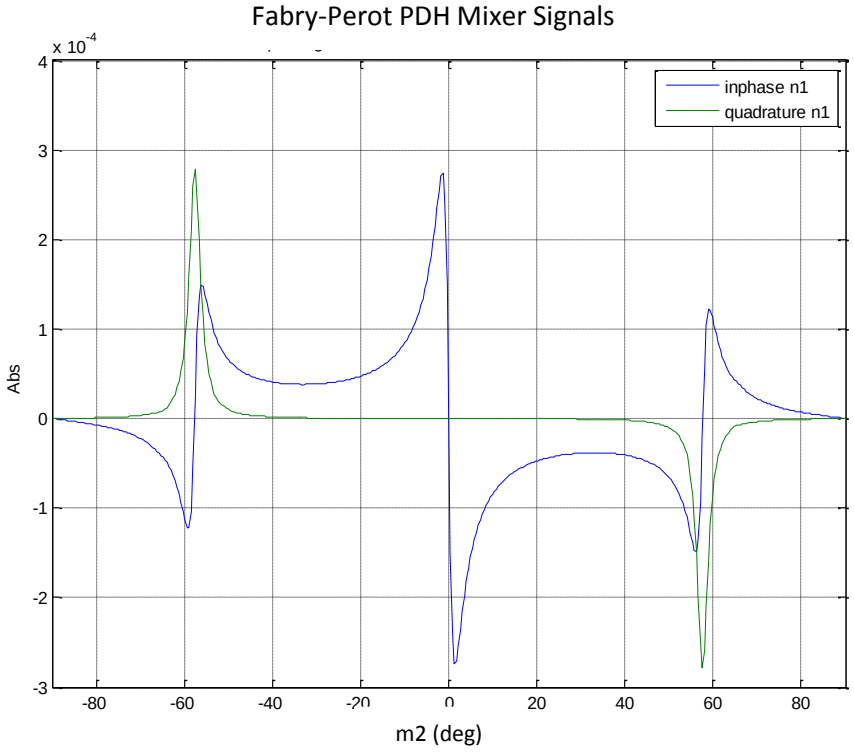

Figure 5-13: Pound-Drever-Hall demodulation signals for a simple Fabry-Perot cavity. The vertical axis is plotted in arbitrary power units. The horizontal axis plots the position of the Fabry-Perot output mirror in units of degrees. 360 degrees equals one wavelength of light. The label "n1" indicates the first node in the Fabry Perot simulation.

5.5.5 Interferometer Fringes

LIGO's Michelson consists of the two input test masses and beam splitter. A Michelson is little more than a complex mirror. LIGO's complex mirror has nuances. The primary nuance permits the "resonant" radio frequency sidebands to transmit to constructively interfere. The carrier, at the same time, is set for nearly totally destructive interference. This was the case for Initial LIGO and was essentially the case for Enhanced LIGO.

Beginning with a simple stable Michelson, the following pictures demonstrate simplistic longitudinal physics of a symmetric Michelson.

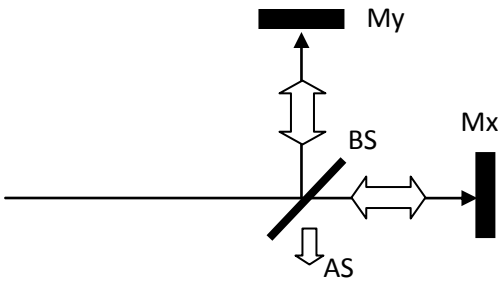

Figure 5-14: Symmetric Michelson diagram. Light enters from the left and is split by the beam splitter. Fifty percent of the total power travels to each mirror. Upon reflection of mirrors Mx and My, the light returns to the beam splitter to be recombined. If the both light beams returning have the same phase and strength they will constructively interfere and leave the Michelson at the antisymmetric port, AS. Returning beams out of phase will have less than maximum power leaving the AS port. In this latter case, constructive interference occurs on the input side and light escapes through the input port to the left.

The following model expresses the interference effect at the Michelson's antisymmetric port.

$$
\begin{aligned}
E_{AS} &= \frac{E_0}{\sqrt{2}}\left(it_{BS}r_{Mx}r_{BS}e^{ik2l_x} + it_{BS}r_{BS}r_{My}e^{ik2l_y}\right) \\
&= \frac{E_0}{\sqrt{2}}\left(it_{BS}r_{BS}\left(r_{Mx}e^{ik2l_x}\right) + it_{BS}r_{BS}\left(r_{My}e^{ik2l_y}\right)\right) \\
&= \frac{E_0}{\sqrt{2}}(it_{BS}r_{BS}r_{Mx}e^{ik(l_x+l_y)}\left(e^{ik(l_x-l_y)} - e^{-ik(l_x-l_y)}\right) \\
&= \frac{E_0}{\sqrt{2}}\left(it_{BS}r_{BS}r_{Mx}e^{ik(l_x+l_y)}\cos\left(k(l_x-l_y)\right)\right).
\end{aligned}
$$

5.12

The lengths of the Michelson arms are written as l_x and l_y, and both Mx and My reflectivities have been equalized. Equation 5.12's exponential term contains what is called "common mode" phase response. This term essentially indicates that equal changes to both arms result in no change in the interference pattern at the antisymmetric port. Changes in the "differential mode", the cosine argument, can change the brightness of the antisymmetric port. For one optical frequency, this Michelson is symmetric in response around a fringe sweep (Figure 5-15). In Figure 5-15, the vertical axis indicates absolute power amplitude as given by FINESSE. The horizontal axis indicates optic position in units of degrees. One wavelength (1064 nm) equals 360 degrees.

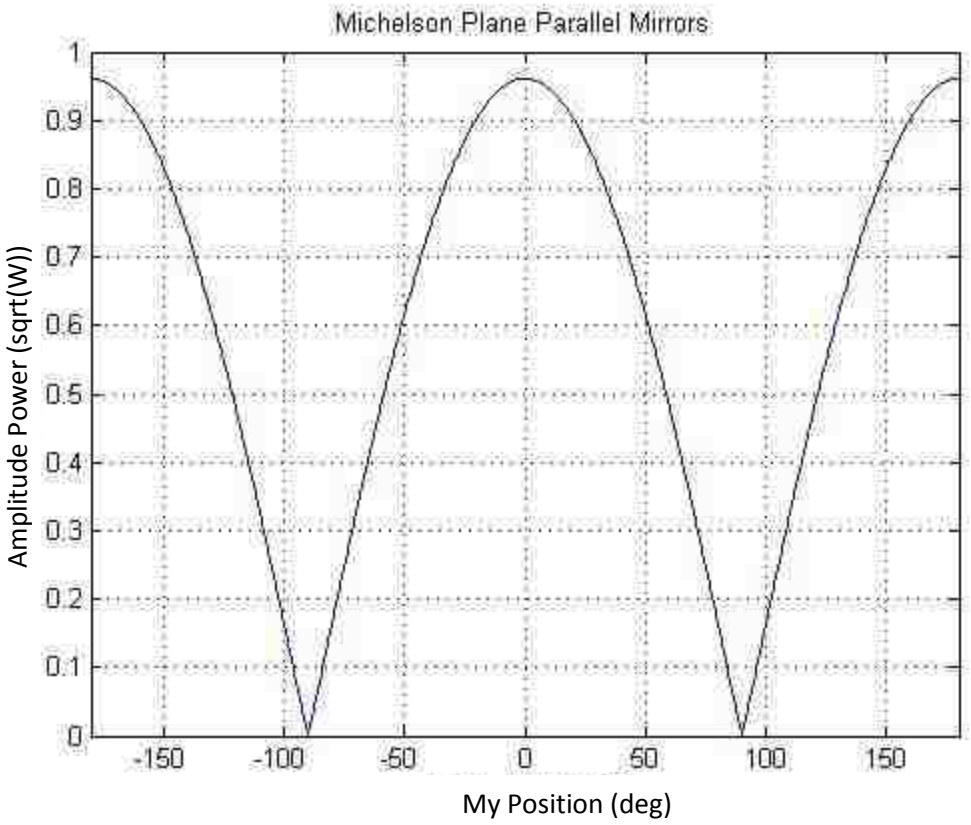

Figure 5-15: An absolute amplitude of a symmetric Michelson's antisymmetric port light plotted as a function of My mirror position in units of degrees. 360 degrees equals one wavelength of light. Notice the amplitude envelope's symmetry.

Altering the symmetry of the Michelson on the wavelength scale generates an interesting result. Simulated output demonstrates frequency favoring. Sideband favoring simply put rises from the ability of a Michelson to filter frequencies. Installing the arm asymmetry cycles through the Michelson's dispersion function as the device passes through constructive and destructive interference. Figure 5-16 demonstrates how sideband amplitudes at the antisymmetric port change as an asymmetric Michelson sweeps through a fringe. Equation 5.13 shows the behavior of a plane wave asymmetric Michelson that has no symmetry or similar mirror performances. The lack of factorability prevents symmetric behavior about the fringe.

$$E_{AS} = \frac{E_0}{\sqrt{2}}\left(it_{BS}r_{Mx}r_{BS}e^{ik2l_x} + it_{BS}r_{BS}r_{My}e^{ik2l_y}\right)$$

$$= \frac{E_0}{\sqrt{2}}(it_{BS}r_{BS})r_{Mx}r_{My}e^{-ik(l_x+l_y)}\left(\frac{1}{r_{My}}e^{ik(l_x-l_y)} + \frac{1}{r_{Mx}}e^{-ik(l_x-l_y)}\right). \quad \textbf{5.13}$$

Changing the curvature of the mirrors to that of the actual detector essentially mimics the result of a plane mirror microscopic position change Michelson to first order. This helps to explain a phenomenon referenced in chapter 6. Equation 5.14 describes the effect of adding transverse structure to the plane wave Michelson model.

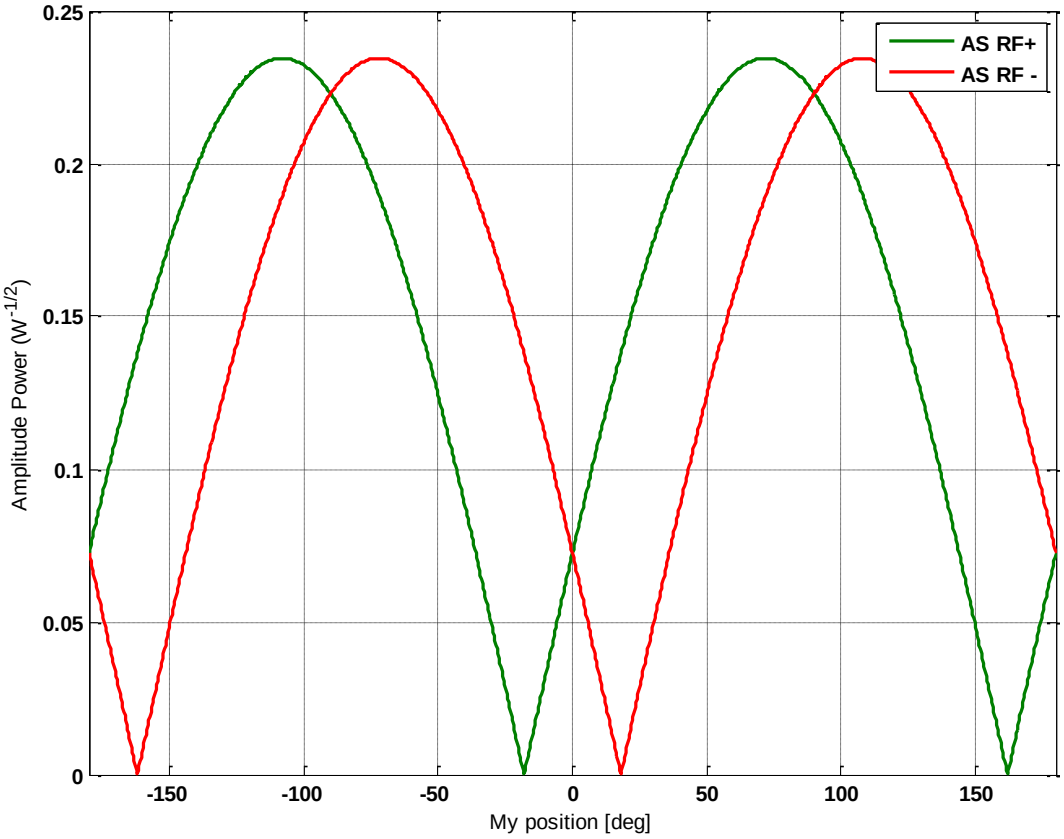

Figure 5-16: Sideband transmission at the antisymmetric port of an asymmetric Michelson interferometer. The vertical axis represents the transmitted amplitude in units of $\sqrt{\mathbf{Watts}}$. The horizontal axis indicates mirror My's position in degrees. It is clear that either the lower sideband (RF-) or the upper sideband (RF+) can dominate when the interferometer is off resonance.

$$E_{AS} = \frac{E_0}{\sqrt{2}}\left(it_{BS}r_{Mx}r_{BS}e^{ik2l_x}\psi_{Gouy,x}\psi_{in,x} + it_{BS}r_{BS}r_{My}e^{ik2l_y}\psi_{Gouy,y}\psi_{in,y}\right). \quad \textbf{5.14}$$

where ψ_{Gouy} is the Gouy phase exponential, and ψ_{in} is the transverse Gaussian structure of the reflected beam. Grouping terms yields,

$$E_{AS} = \frac{E_0}{\sqrt{2}}(it_{BS}r_{BS}r)\left(e^{-ik(l_x+l_y)}\right)\left(\psi_{Gouy,x}\psi_{in,x}e^{ik(l_x-l_y)} + \psi_{Gouy,y}\psi_{in,y}e^{-ik(l_x-l_y)}\right). \quad \textbf{5.15}$$

Here the reflectivities of the end mirrors are assumed to be identical. This equation's last term indicates that the returning fields must possess the same spatial features for perfect constructive or destructive

interference. If the fields are not identical, there will be a non-zero ambient background; this is also called the "contrast defect."

5.5.6 Power Recycled Michelson

A power recycled Michelson (PRM) inserts an optical recycling mirror at the input port of a Michelson interferometer. This additional mirror forms a peculiar resonance cavity. If a monochromatic light source in injected into the cavity, the anti-symmetric port must be kept near destructive interference while the beamsplitter-recycling mirror distance is kept at an integer number of half-wavelengths to attain optimum power build-up. Computing the circulating electric field follows math similar to that involved with a simple Fabry-Perot cavity.

The symmetric PRM has symmetric arm lengths. Both iLIGO and eLIGO were designed with an asymmetric PRM. The original concept attributed to Lise Schnupp permitted the sidebands to transmit to the antisymmetric port while the PRM builds up carrier power. This permitted the sidebands to act as local oscillators at the antisymmetric port. Equation 5.16 models light fields within the PRM as a function of PRM arm length and mirror reflectivity.

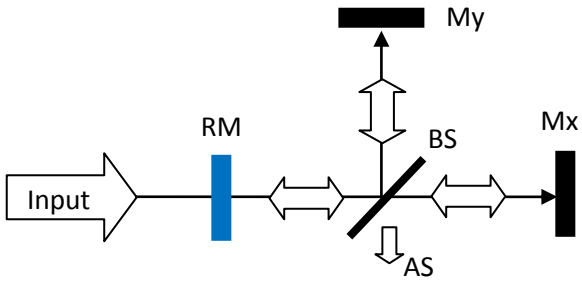

Figure 5-17: A simplified diagram of a power recycled Michelson (PRM). A recycling mirror (RM) now resides at the input port. When the Michelson (mirrors in black) is set for destructive interference at the AS port, the RM can be tuned in position to achieve resonance for a given family of frequencies.

$$E_{circ} = it_{RM}E_0 + r_{RM}r_{Mx}(it_{BS})^2 e^{-\frac{i\omega}{c}\cdot 2(l_c+l_x)}E_{circ} + r_{My}r_{RM}(r_{BS})^2 e^{-\frac{i\omega}{c}\cdot 2(l_c+l_y)}E_{circ}.$$

$$E_{circ} = \frac{it_{RM}}{1 - r_{RM}r_{Mx}(it_{BS})^2 e^{-\frac{i\omega}{c}\cdot 2(l_c+l_x)} - r_{RM}r_{M_y}(r_{BS})^2 e^{-\frac{i\omega}{c}\cdot 2(l_c+l_y)}}.$$

5.16

Where l_c represents the distance from the RM to the BS, E_{circ} represents the circulating electric field within the PRM. To determine field amplitude transmitted to the AS port, multiply by the BS amplitude transmission coefficient.

The circulating fields are intentionally written in terms of lengths of the x- and y-Michelson arm lengths. Conventionally, circulating field is written in terms of the differential and common degrees of freedom. This notation emphasizes the importance of moving one mirror, and how the two arms of the interferometer can be treated as separate cavities [43].

A simple toy model of the Livingston PRM is shown in Figure 5-17. The toy model first began with a nearly symmetric, stable PRM adjusted for power build-up. Carrier and sideband light fields were

injected into the interferometer, while a few higher order modes were tracked. The 24.5 MHz phase modulator was set to a modulation index of 0.3. The mirror curvatures differed by a nearly 6 %. Figure 5-18 shows the result of a radio frequency sideband build up in both arms as the end mirrors Mx and My are differentially moved.

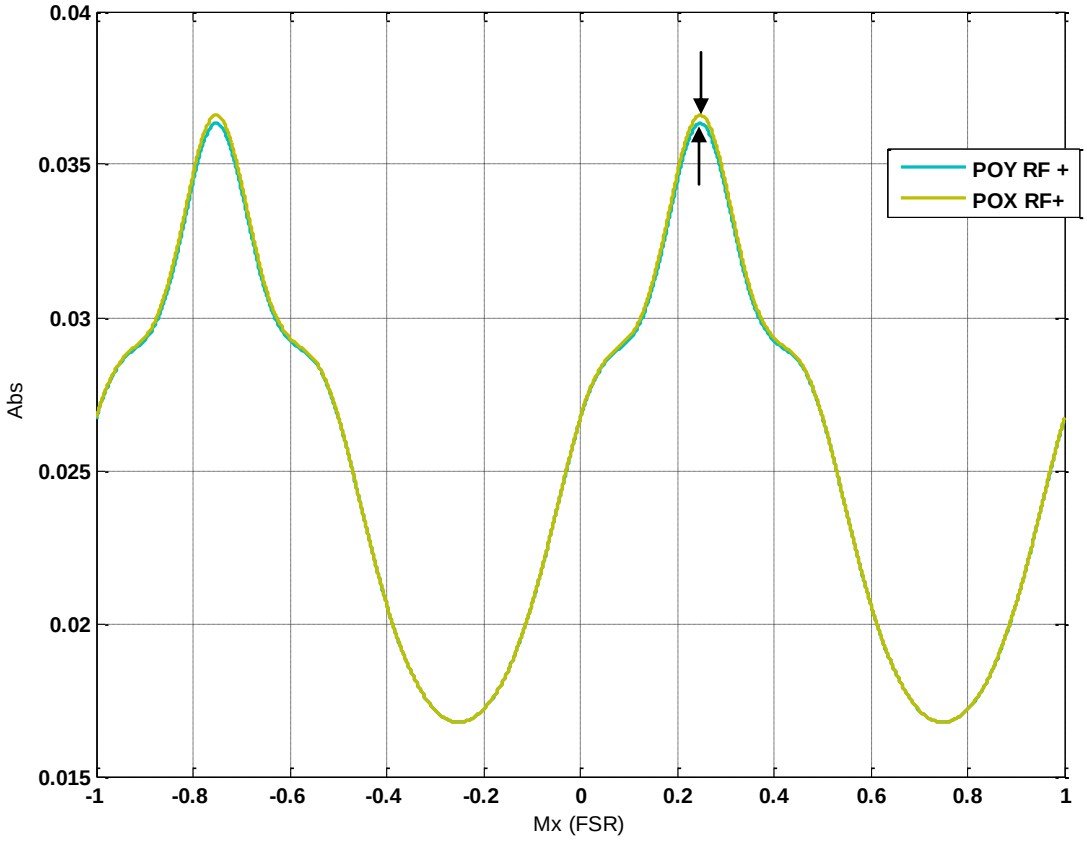

Figure 5-18: Circulating upper sideband light amplitude picked off at the end mirrors plotted versus differential end mirror position. The discrepancy comes from a slight mirror curvature mismatch.

Micro-motions of the mirrors resulted in gains in particular frequencies. Another phenomenon consistent with the separate treatment of the arms is size and shape of the sideband beam. Difference frequencies defocused at different rates. This can be observed in a model of the full interferometer. Basic tests demonstrate at least 10 percent imbalance could be induced by microscopic asymmetries (Figure 5-19). Such was the case in the iLIGO once the detector reaches a locked state. Data below, Figure 5-20, shows an occasional imbalance as great as 2. This correlates to the Schnupp asymmetry and the position of the sidebands with respect to the frequency response of the full interferometer. Additional simulations using a sub-optimally mode matched interferometer demonstrates a simulated sideband discrepancy as great as four times, Figure 5-21. This brackets the cold state of the interferometer and the heated state of the interferometer.

The author would be remiss if he did not mention the work performed by reference [44]. This work discussed the nature of dispersion in cavities more complex than a linear, two mirror Fabry-Perot.

According to reference [44]'s model, one should not automatically assume symmetric dispersion relations. Therefore, the modeled FINESSE based PRM did not tread on unfamiliar territory.

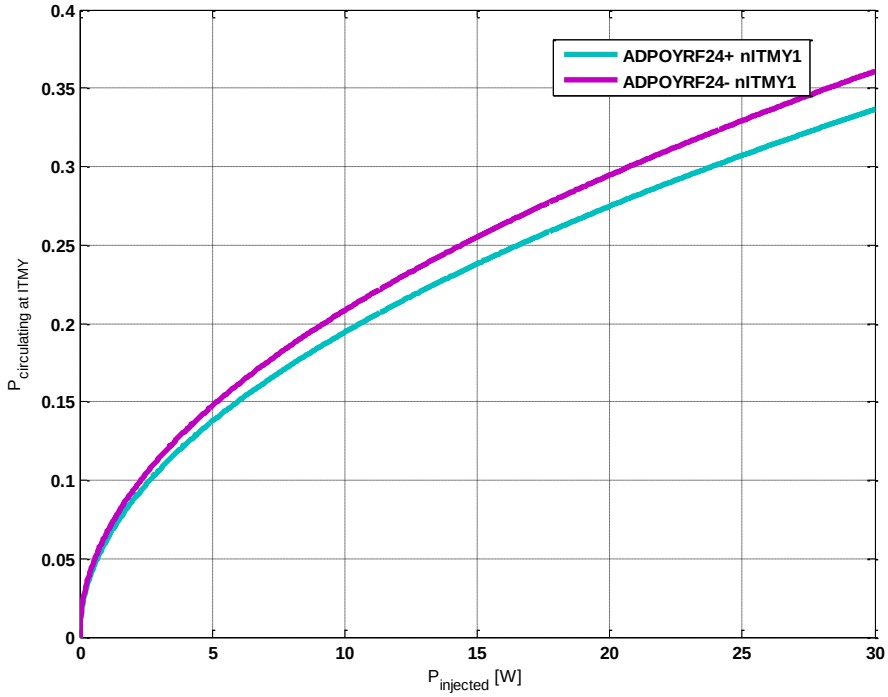

Figure 5-19: Upper and lower sideband light circulating in a simulated LIGO plotted as a function of injected power. No microscopic offsets have been placed on the ITMs. The mirrors comprising this simulation have the cold state curvatures. This demonstrates the discrepancy due to non-symmetric curvatures.

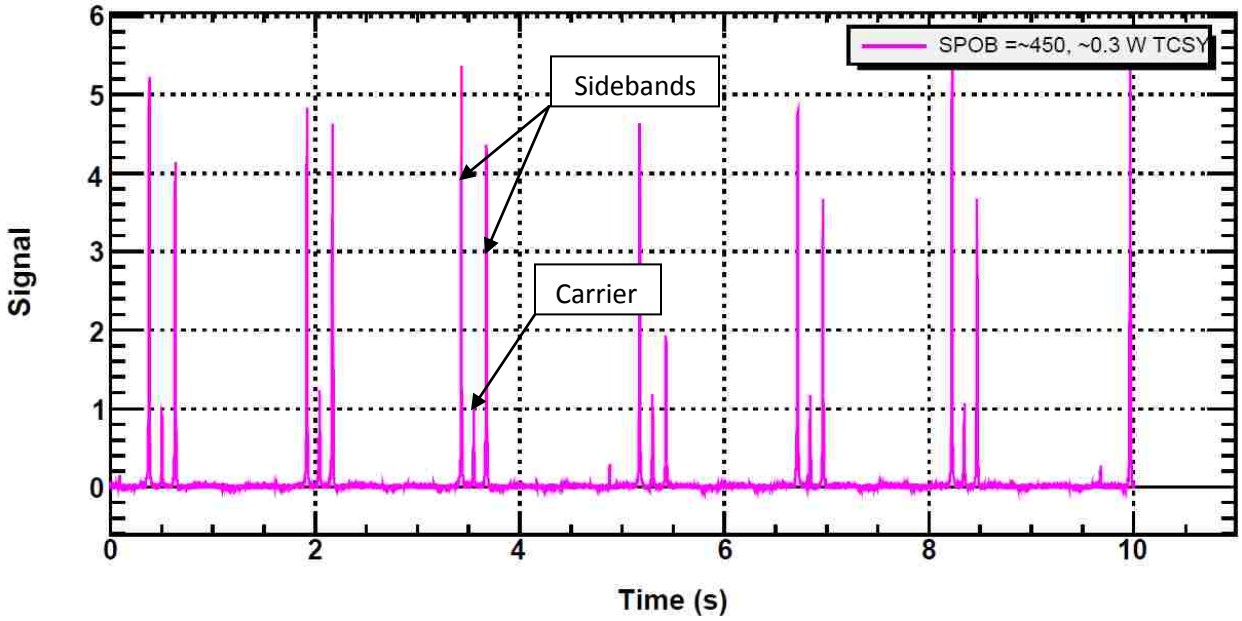

Figure 5-20: Double demodulated light from the beamsplitter in the LIGO Livingston detector indicates total sideband power in uncalibrated power units as a function of time. The interferometer's state in this picture was fully powered (8 W). The upper and lower sideband are exchanging dominance as the ITMy mirror is being heated by its auxiliary CO_2 laser. Prior to heating only one sideband dominates. Following heating, both sidebands seem to alternate dominance.

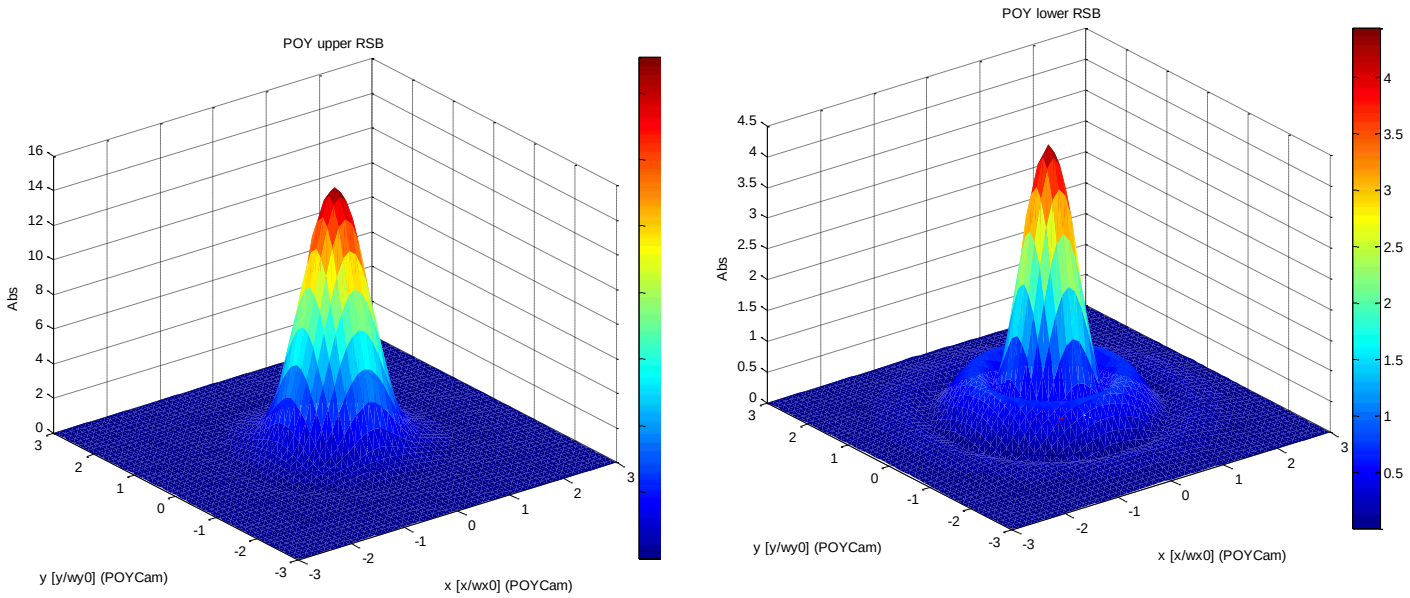

Figure 5-21: Simulated field distributions of the resonant upper and lower sidebands at the ITMy. The z-axis depicts field intensity. The xy-plane depicts the plane of a frequency selective camera. One can see that the peak of the upper sideband in this model is as great as 4 times higher than the lower sideband. Also the results of the lower sidebands presents a beam that no longer appears to be a fundamental Gaussian mode.

Reference [44] continues to indicate that sideband imbalance does not need optical element complications. Rather a simple increase in mode number can begin the complications. Increasing the number of coupled cavities results in distinct departures from symmetric dispersion.

According to their models, sideband imbalance had a ratio of roughly a factor 4 to 6 due to differences in storage time. FINESSE models leaned toward the lower value of the two (factor 4) as shown by beam size images. In reality, a cold Livingston interferometer demonstrates as much as a factor of 2 to 4 difference in sideband power.

The derivation of a plane wave Michelson interferometer suggests that only one interference quadrature component should be detected at the antisymmetric port. It was perceived that mysterious sideband imbalances resulted in in-phase demodulation signals arriving at the anti-symmetric port. Reference [44] explain the phenomena through failures in mode matching and modal corruption.

5.6 First Order Equivalence of Faux Thermal Lenses

One optical element for a proper model of iLIGO remains to be proofed. In chapter 6, the thermal model of the input test masses are described in detail. To save CPU time expense phase maps derived from FEM based models are replaced by spherical lenses.

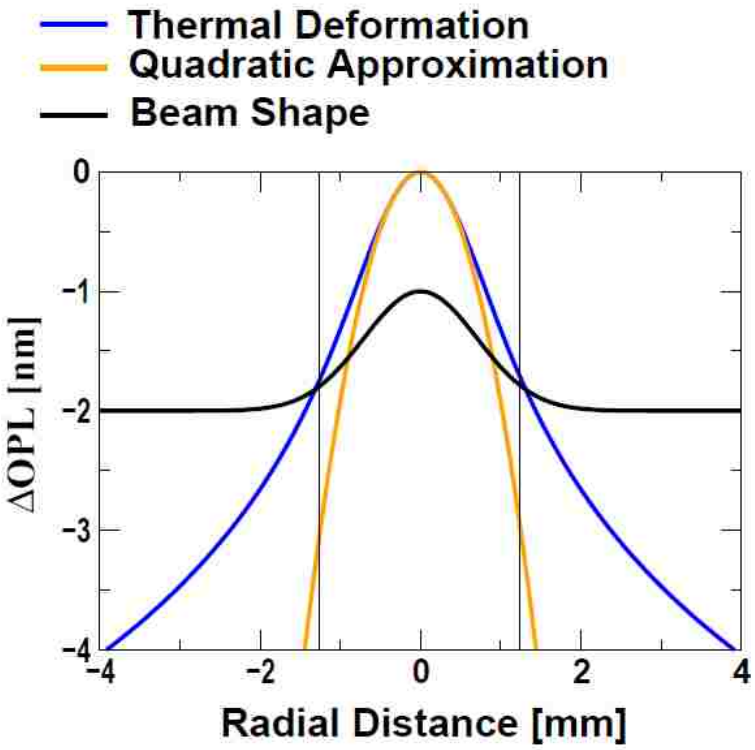

Figure 5-22: A toy plot showing change in optical path length induced by a lens (quadratic approximation) and a thermal lens (thermal deformation) as a function of radial distance from the center of propagation. Beam shape is superimposed as a reference for the effected region.

To first order, spherical lenses behave similarly to thermal lenses. The spherical approximation simulates roughly 93 to 94 % of a thermal lens's refractive capacity [23, 45]. This means the first order optical phase delay follows a parabolic delay much like that of a spherical lens (Figure 5-22). The difference in the second order comes from the "wings" induced in the optical path length. These wings can be modeled by increasing the number of representative modes as noted in references [16], [45], and [23].

Next in accepting these faux thermal lenses is to determine the level of lensing that occurs at nominal power. According to Winkler's 1991 approximation of Hello and Vinet's paper the maximum induced phase difference for a 10 mW absorption is 5 km [46]. Although this may appear large, keep in mind that the LIGO ITMs have negative lenses on the order of 10 km. This number is derived as follows:

$$\Delta OPL = \delta s$$

$$= \frac{\beta}{4\pi\kappa} P_a \qquad \textbf{5.17}$$

where β is the thermorefractive index, κ is the thermal conductivity, and P_a is the absorbed power. The lens power due to this change in optical path can be written as follows:

$$f_{therm} \approx \frac{\omega^2}{2\delta s}$$

5.18

where: f_{therm} is focal power due to the change in optical path length and ω is the spot size.

Combining equation 5.17 and 5.18 together yields focal power as a function of absorbed power.

$$f_{therm}(P_a) \approx \frac{\omega^2}{2\left(\frac{\beta}{4\pi\kappa} P_a\right)}.$$

5.19

The thermorefractive index for fused silica is roughly $1.5 \cdot 10^{-5} \frac{1}{\mathrm{K}}$. Thermal conductivity equals $1.38 \frac{\mathrm{W}}{\mathrm{K \cdot m}}$. Assuming a 5 ppm absorption ratio and a 5 kW circulating power, the approximate themal focus is 34 km.

Since the thermal lens occurs in the substrate, it is appropriate to model an interferometer in the as drawn in Figure 5-23. This permits the modeling of doubly lens affected fields in the power recycled Michelson. It also permits the modeling of mode mismatch with fields entering and leaving the arm cavities.

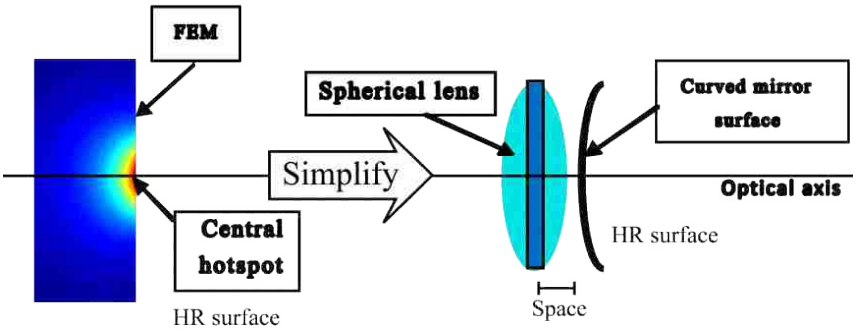

Figure 5-23: Decomposing an FEM model into a composite optical component. A profile of a simulated LIGO ITM (left) shows heat accumulation near the highly reflective surface of the optic. The thermal lens is replaced by a spherical lens placed near a mirror of constant curvature.

6 Evaluating Thermal Phenomena Using Thermal Models

6.1 Introduction

In this chapter, the FEM model assembled in chapter 5 is utilized in determining the absorption ratio of the ITMs and in diagnosing the culprit of thermally induced ASC signals. The interferometer simulation is shown to be able to simulate radio frequency images taken in 2003. The full interferometer simulator is then combined with the FEM model to reproduce interferograms taken at the AS port in 2009. Finally, an analytical based modal program is compared to modal measurements taken of the iLIGO instrument in 2007.

6.2 Measuring ITM Absorption

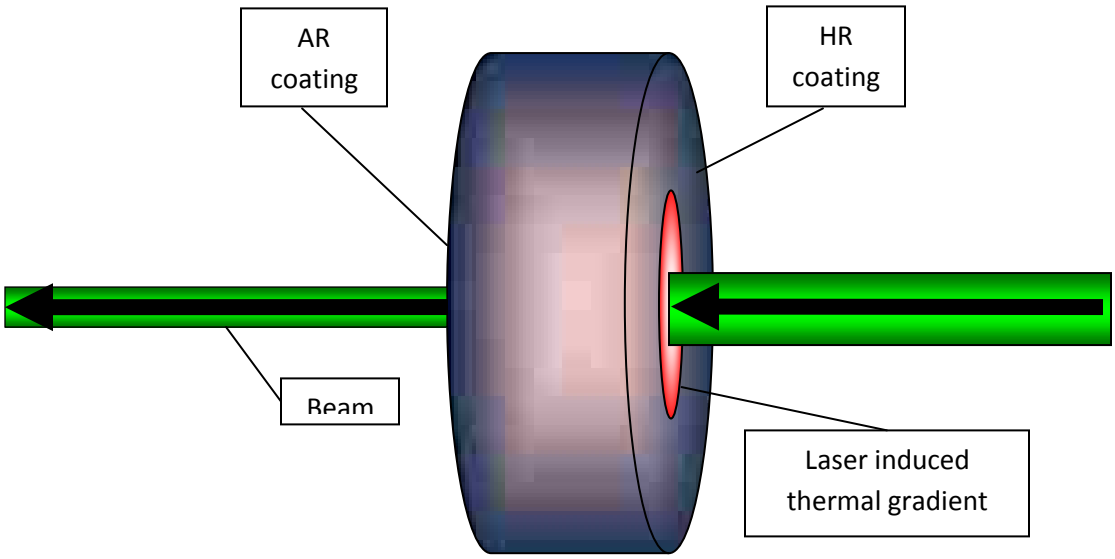

Figure 6-1 : Diagram of large optic mirror heating induced by Nd:YAG beam depicted in green.

Preceding chapters indicate that the ITMs were the largest thermal offenders. Figure 1-4 depicts these mirrors as the input couplers to the arm cavities. The large optics of LIGO were all comprised of the same material, fused silica glass. Similarly they all use tantalum pentoxide based high and anti-reflective coatings. Design substrate specifications call for mirrors to have 5 ppm/cm absorption. Most of the ITMs in LIGO's detectors are purchased from Heraeus Quartzglas and coated by CSIRO. The primary purpose of the ITMs is to delay the "carrier" light long enough to interact with passing gravitational-waves.

Unfortunately absorption across all optics was not uniform. Nor, as we demonstrate in later sections, was absorption dominated by the substrate. Lack of uniformity could be traced to manufacturing difficulty of large optics. Absorption in the coating could be driven by a number of factors including crystalline defects or hydroxyl contamination. Nevertheless, such effects could at present only be estimated and should be the motivation for following future research.

Measuring absorption of a piece of glass may be done in a variety of ways. The most simple and perhaps brute force tactic removes the optics from their vacuum chambers. In a controlled environment, a laser passes through the optics. The absorption due to the substrate and the coating would then be measured and distinguished. This type of metrology "pixelizes" the surface allowing for detailed absorption measurements of small regions.

An example shown below demonstrates how Beer's law models the reduction in amplitude of a passing laser field. Begin with a wave whose amplitude is E_0, and spatial distribution is $\psi(x, y)$.

$$E_{in} = E_0 \psi(x, y) e^{-ikz + i2\pi ft} \quad \textbf{6.1}$$

where ω represents the angular frequency, and k represents the wavenumber.

Attenuation through a linear medium follows an exponential decay as noted in references [15] [19], [33], and [22].

$$\psi_{atten} \propto e^{-\alpha z} \quad \textbf{6.2}$$

where α equals the attenuation coefficient, attenuation per unit length. The resulting field becomes

$$E_{out} \propto E_0 \psi(x, y) e^{-ikz + i2\pi ft - \alpha z}.$$

If this result is modulus squared, the oscillating terms become 1, and we are left with the following:

$$P_{out} \propto P_{in}(x, y) e^{-2\alpha z}.$$

This equation does not include losses due to scattering, and therefore one needs an integrating sphere for this experiment.

Another tactic uses a characteristic of the Fabry-Perot interferometer. When a cavity goes from zero circulating power to a resonant state, the laser light entering the cavity takes a finite amount of time to perform its roundtrip. Each roundtrip increases the amount of circulating power as injected light leaks in in-phase with the circulation until the cavity reaches a stable, statistical maximum. This step wise resonance build up is called a "ring up." This phenomenon is also true in reverse. A fully energized cavity takes a finite amount of time to "ring down." The characteristic time for both processes is called the decay time.

Decay time can be computed from measured or theoretical reflectivity [40].

$$\tau_{decay\ time} = \frac{2T}{\ln(r_1 r_2)}$$

6.3

where T is one-half the round trip time for light, and r represents the reflectivity for the Fabry-Perot's mirrors. If the mirrors abnormally scatter or absorb, decay time will not be as long.

The first method requires an invasion of the vacuum system, risks the large optics' health, and interferometer alignment. The second method lacks simple analysis due to extra resonators upstream of the arm cavity. The second method also cannot discriminate between mirrors in terms of loss or measure coating versus substrate losses.

A third option computes the absorption parametrically. In this case the body resonances of an optic are tracked. As the LIGO detector change PSL power between two values, the optics experience two levels of optically induced heat. Temperature changes in the optics change the frequency of the body mode. This occurs because of thermally dependent Young's modulus and Poisson ratios. Changes in frequency as a function of time can be fit using FEM based models. The fit parameters ultimately discern the absorption ratio. One cannot easily discern the difference between coating and substrate absorption using this technique if measured values are too noisy or optics do not have a narrow mechanical quality factor. Therefore, the result is given in units of absorbed power versus incident power.

This third option is not invasive to the detector. It does require large sample times that take away from interferometer commissioning time. It also requires knowledge of nearly everything that can inadvertently contribute heat to the mirrors.

The last statement is rather important since the temperature induced relative frequency shift can be from 10^{-5} to 10^{-4}. Nd:YAG radiation is not highly absorbed by the optics ($\alpha_{SiO_2} \sim 10^{-6}\ 1/\mathrm{cm}$). Therefore external sources can easily dominate the signal. For instance, the iLIGO LVEA would change temperature by 1 degree Celsius during a 45 minute period. Nonetheless, the third approach was utilized for absorption studies in July 2008.

6.2.1 Thermal Influence of the BSC and Beam Tubes: Accounting for Temperature Noise

The largest contributor and perhaps most visible were the beamsplitter chambers (BSCs) shown in Figure 6-2. Recall the large optics in LIGO sat suspended in the BSCs, the large vacuum tanks. Radiation rather than conduction served as the primary means of heat transport. The tank itself sat in an air conditioned environment, the LVEA and the VEAs. This does not mean that the temperature remained stable throughout the day. HVAC units activated in a step-wise fashion throughout the day.

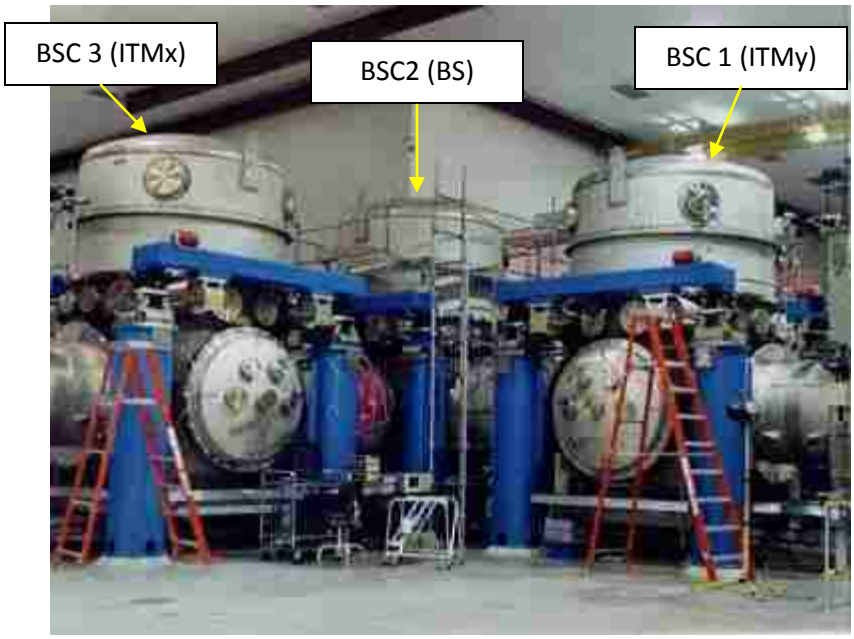

Figure 6-2 : A photograph of the three beam splitter chambers (BSCs) at the LIGO Livingston vertex in the LVEA building. The acronym BSC carries for all large optics tanks except the recycling mirror. The arrows point to particular tanks and their respective optic.

Such a problem could have been solved by either keeping trend data of the HVAC and the temperature of the whole LVEA and VEAs. One must then account for the several tons of steel to thermally equalize. A simpler approach placed thermometers on the tanks in expectation that they will only monitor the tank temperature.

A set of National Semiconductor LM34 semiconductors comprise the sensors (Figure 6-3) and readout data via a transimpedance circuits whose calibration is noted. A single sensor sits on each tank as depicted in Figure 6-4.

Figure 6-3: Internal photo of National Semiconductor LM34 based temperature sensor. The LM34 can be seen glued to the base of the metal Pomona® box with thermal epoxy.

Figure 6-4: Photograph of a thermal sensor situated on a BSC shell.

As shown in Figure 6-4 the sensors were shielded from direct airflow from HVAC vents. Pictures of the sensors suggest the thermometer measured both the air and tank temperature. Nevertheless, these devices gave reasonable results (Figure 6-5).

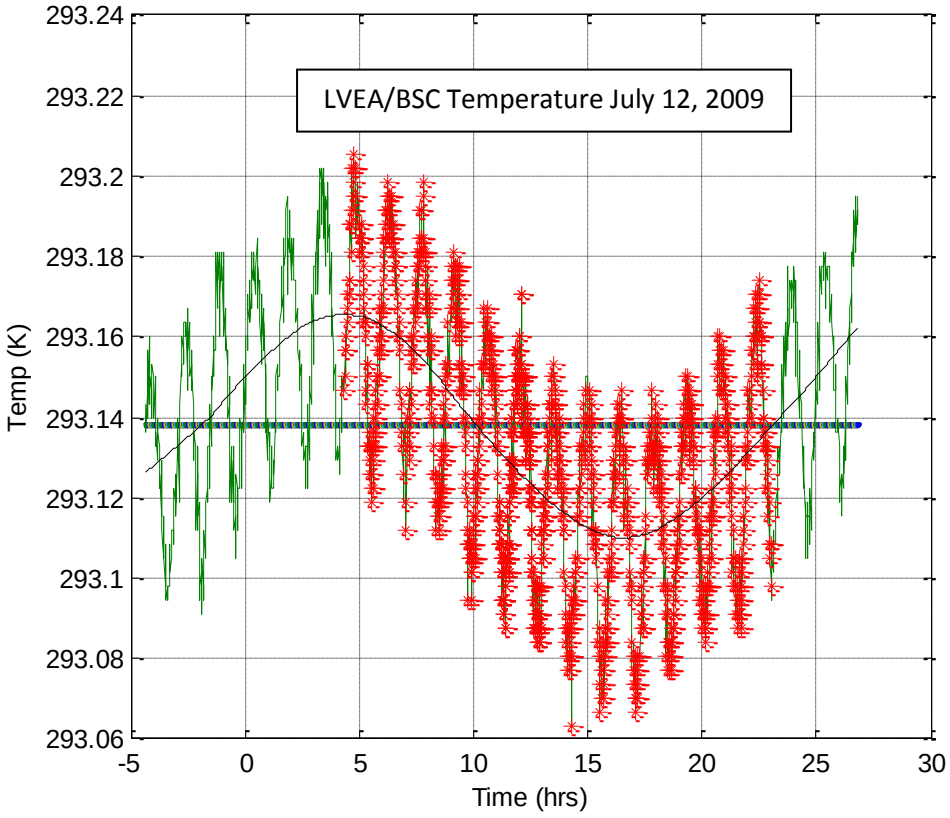

Figure 6-5: Temperature data taken from the BSC 1 plotted with respect to GPS time. Temperature data covers more than ten hours. Red adsterisks indicate datums whose frequency information has been fit.

Radiation based thermal transport models depend on the Stefan-Boltzman constant, emissivity, and the difference of the temperatures raised to the fourth power.

$$F = \epsilon\sigma\left(T^4 - {T_{amb}}^4\right),$$

6.4

where ϵ is mean emissivity of a material, σ is the Stefan-Boltzman constant, T_{amb} is the ambient temperature, and T refers to the material temperature. The emissivity of steel equals 0.54. The emissivity of fused silica equals 0.89. The sign of the result indicated if the BSC behaved as a heat sink or a heat source. FEM models implied that shielding within the BSC did not retard heat transport greatly. Convection currents around the BSC permitted the BSC to achieve thermal equilibrium almost uniformly in spite of the low thermal conductivity of steel. This assertion removed complications of stainless steel's low thermal conductance.

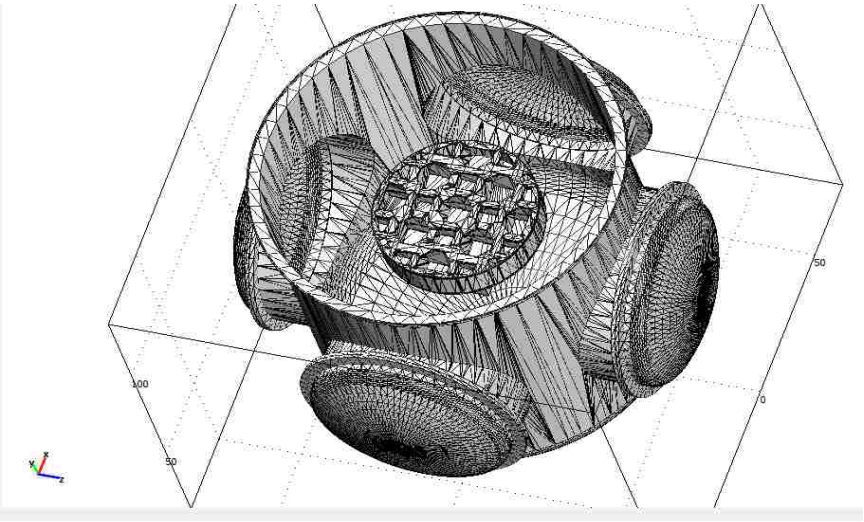

Figure 6-6: FEM mesh of the BSC and payload table. The mirror suspension cage and beam baffle are obscured by the payload table.

Another large and potentially spurious heat source came from the arms. The arms had nearly 15 km of stainless steel (Figure 6-7). They sat outside the environmentally controlled buildings. Therefore, the arms gathered heat during daylight hours and provided a heat source for the test mass during evening and night hours.

Figure 6-7: A picture of LIGO Livingston's beam tubes during construction. Photograph credit: Larry Jones (c1998).

This heat source required to be quantification. First, the view factor of the ITMs could be described as a solid angle. The beam tube sat approximately 25 meters away from the ITMs. Therefore, the angle subtended by an arm equaled 1.57 milli-steradians.

Immediately, this discouraged the involvement of the arms. Nevertheless, this hypothesis assumed the arms heat during the day and effected frequency drift measurements made at night or reduced power levels. Calculating the temperature change of an arm tube required an estimate of the thermal resistance between the heat source, the Sun, and the beam tube.

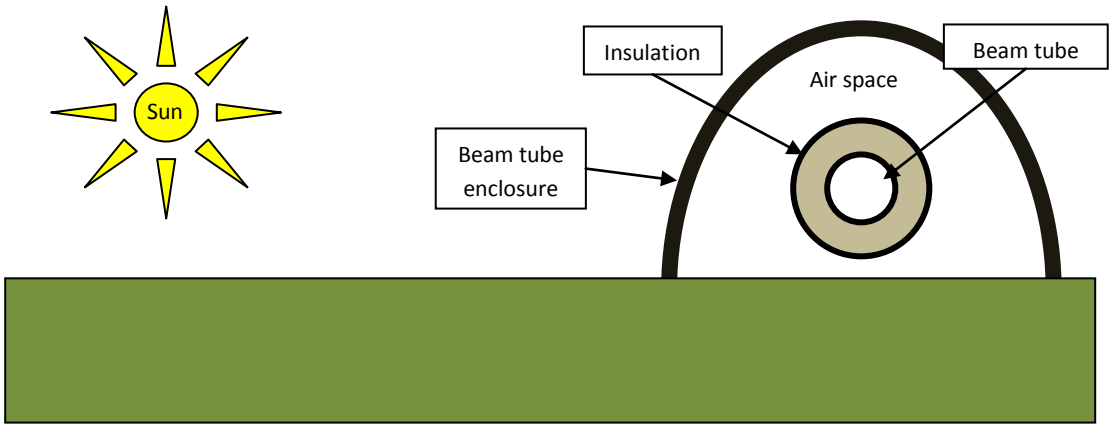

Figure 6-8: Cartoon of heat transport problem for LIGO arms. Thermal resistance includes the steel arms, fiber glass and aluminized Mylar insulation, the air space, and the concrete enclosure.

Figure 6-8 shows a diagram of an arm's heat source, the environment. The various barriers shown resisted the transportation of heat. Thermal resistance of each barrier dictated how much reached the arm. The computation begins with calculating the amount of heat transferred from the atmosphere to the concrete enclosure. Here the heat transfer coefficient, h_{air}, approximates the amount of energy per second transferred across a contact interface, and $A_{concrete}$ equals the wetted surface area of the concrete enclosure.

$$R_{\frac{atm}{concrete}} = \frac{1}{h_{air} A_{concrete}}$$

$$= \frac{1}{8 \frac{\mathrm{W}}{\mathrm{m^2 K}} \cdot 31065 \ \mathrm{m^2}}$$

$$\approx 4 \cdot 10^{-6} \frac{\mathrm{K}}{\mathrm{W}}.$$

Next compute the thermal resistance of 6 inch thick concrete.

$$R_{concrete} = \frac{L}{\kappa_{concrete} \ A_{concrete}}$$

$$= \frac{0.1524 \ m}{0.29 \frac{\mathrm{W}}{\mathrm{mK}} \cdot 31065 \ \mathrm{m^2}}$$

$$\approx 1.7 \cdot 10^{-6} \frac{\mathrm{K}}{\mathrm{W}}.$$

Now compute the resistance of the air gap.

$$R_{air \ gap} \approx 8.4 \cdot 10^{-6} \frac{\mathrm{K}}{\mathrm{W}}.$$

Finally, one can compute the thermal resistance of the steel beam tube with $\kappa \approx 16.3 \frac{\mathrm{W}}{\mathrm{mK}}$.

$$R_{steel} \approx 1.2 \cdot 10^{-8} \frac{\mathrm{K}}{\mathrm{W}}.$$

The total resistance is on the order of 10^{-8} W/K. If one assumes a moderately bright day and a 100 % energy transfer from sunlight to the atmosphere surrounding LIGO's beam tube enclosure, the temperature shift at worst is nearly 0.05 Kelvin. This estimate excludes the aluminized Mylar and fiberglass thermal blanket covering the beam tube itself as well as the stainless steel beam tube itself. This result is much smaller than the LVEA's temperature shift in one day. Therefore, such a result places the arm in the family negligible artifacts.

6.2.2 Measuring the Absorption of the ITMs Using Body Modes

Once the spurious heat sources were tracked or removed from the analysis, the absorption data acquisition and analysis was fairly straightforward. The mirror body modes tracked resonated at nearly 9.3 kHz (Figure 6-9). This particular body resonance (the drumhead mode) was the first excited mode and the mode that most readily interacted with LIGO's differential arm degree of freedom.

A fully locked LIGO interferometer was then power cycled between 1 Watt and 4 Watts. Power step duration needed to be long enough to permit the mirrors to reach laser induced thermal stability. This was roughly 90 minutes. Actual power values were held for 7200 second intervals. High speed time series data was read off using LIGO's 262144 sample per second channels. These channels were intended to monitor light leaving the anti-symmetric port phase demodulated at the primary modulation frequency (24.5 MHz) during S5.

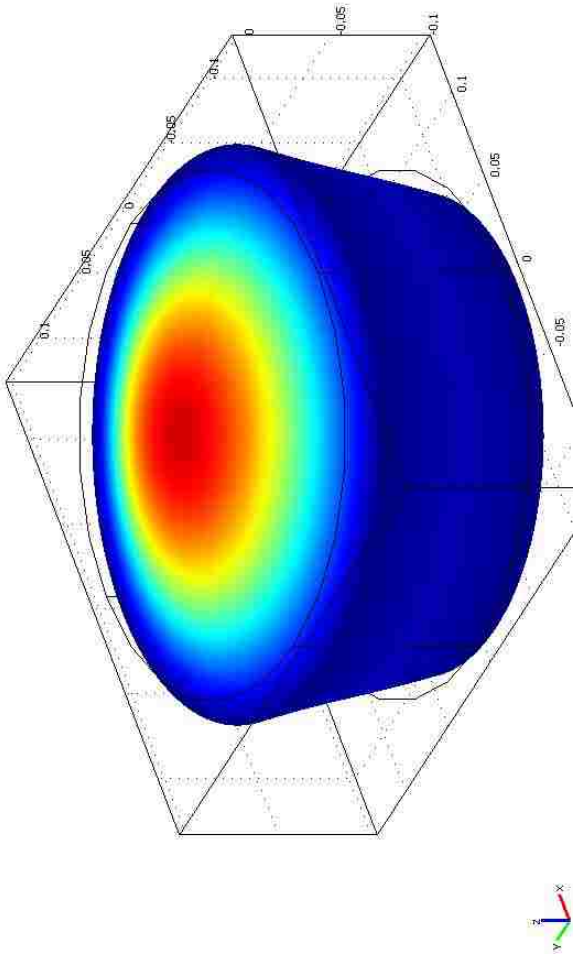

Figure 6-9: FEM model of an ITM's 9.3 kHz body mode. Color represents level of axial displacement. The black wire structure depicts the zero oscillation state of the mirror. The level of deformation has been exaggerated for illustration.

At the beginning of chapter 5, the substrate material is indicated as ultra pure fused silica. Physical constants for fused silica are shown in Table 5-1. Focus on the Young's modulus and the Poisson ratio. The first derivative describes glass as a material that grows stronger with temperature. This hardening happens only around room temperature [47].

Data acquired from the power cycles are shown in Figure 6-10:. The first plot shows temperature of the BSC 1. The second plot describes the measured frequency taken from the high speed antisymmetric demodulated in-quadrature phase signal. This is what one wishes to fit to find ITM absorption ratios.

Plot three simply documents the amount of power injected to the mode cleaner. The IOO chain from the mode cleaner was estimated to be roughly 80 % efficient.

Colored regions connote analyzed time series data. To make the data more tractable during analysis, the initial data rate was reduced by a factor of 8. The second plot was generated from Fourier transforms 256 seconds in length. The slow meander in the temperature data corresponded to the diurnal temperature variations. High speed fluctuations correlated to the HVAC activity.

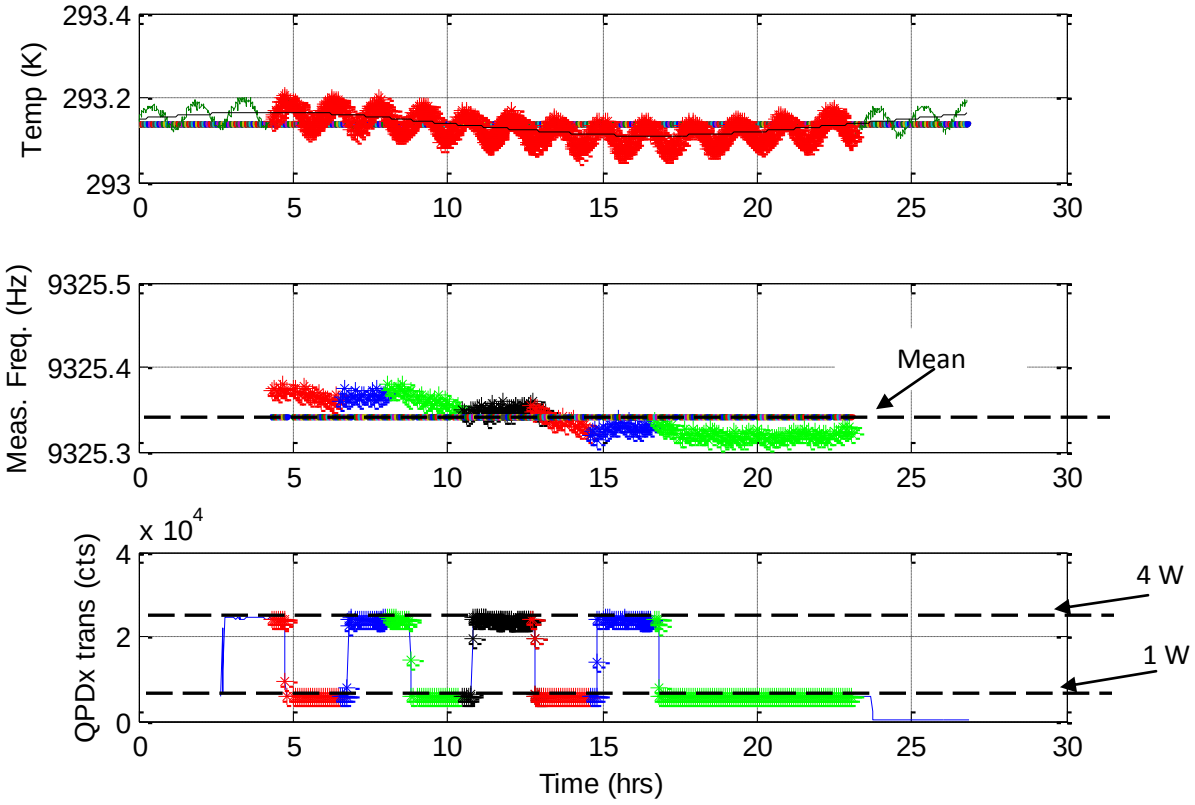

Figure 6-10: Optically induced frequency shift time series data from a July 12, 2009. Subplot 1 plots the temperature variations as measured by BSC 1's thermal sensor. The red region in subplot 1 indicates the contiguous data sample analyzed. Subplot 2 traces the frequency shift of ITMy's 9.3 kHz body mode. Subplot 3 indicates when the interferometer ran at 1 W (low level) and 4 W (high level). Subplot 2 and 3's colors correspond to each other along the time axis and indicate data segments that were analyzed. Horizontal lines in subplot 1 and 2 are mathematical means of the data.

Similar slow fluctuations were observed in the frequency shift data. This slow oscillation also correlated to diurnal temperature variation. Time shifting temperature data to align zero crossing of the frequency average yielded a rough estimate of heat transport time lag between the BSC and its respective ITM.

The empirical time results were also modeled using FEM. External heating demonstrated time constants of this order of 17000 s. This matched modestly to the empirical time shift within 2000 s. Error bars for the zero crossing were roughly 1000 seconds.

Converting frequency shift data to absorption ratio can be performed rather naively in the following fashion. Body mode frequencies of a structure depend on its Young's modulus. The thermal dependence of Young's modulus for fused silica is given in below.

$$\frac{dE}{dT} = 1.5 * 10^{-4} \frac{1}{K \cdot Pa}.$$

Since body mode frequencies typically grow as the square root of the body's linear dimensions, the relative change to body mode frequency is approximately

$$\frac{\frac{df}{dT}}{f} = \left(\frac{1}{2}\right)\left(\frac{\frac{dE}{dT}}{E}\right),$$

$$= 7.5 * 10^{-5} \frac{1}{K}.$$

Using this value in conjunction with the heat capacity of the mirrors, one could arrive at the following equation:

$$\frac{\frac{df}{dT}}{f} = \left(7.5 * 10^{-5} \frac{1}{K}\right)\left(\frac{P_{abs}}{7390 \frac{\mathrm{J}}{\mathrm{K}}} + \Delta T\right).$$

6.5

Even though this equation was not used in the final absorption its utility is found in chapter 6 [48, 49].

This equation effectively approximates the absorption to a couple of ppm (ITMx = 2.35 +/- 0.18 ppm; ITMy = 3.655 +/- 0.114 ppm). This estimate depends on the amount of data used. In this toy model, the relative frequency shift linearly depends on temperature and absorbed power. It does not correctly take into account the behavior of actual LIGO fused silica under differential thermal loading and its environment. The toy model does suggest to readers to expect 10 ppm relative frequency changes. Therefore, it would be an advantage to track body modes with higher base frequencies. However, it was discovered that the higher frequencies did not interact reliably with the 1064 nm beam.

For this type of analysis, a family of reasonable base frequency choices exists. This forces the analysis to involve the thermal history of the LIGO ITMs to correctly model the data. This was resolved by collecting data from several hours prior to the actual experiment. Three hours of lead temperature data are shown in subplot 1 of Figure 6-10. A total of seven hours was used in the thermal analysis.

A more sophisticated model for relative frequency shift is shown in equation 6.6.

$$\frac{\partial f}{f} = (T_{mean}) \left(10.5 \cdot 10^{-5} \frac{1}{\mathrm{K}}\right) + \int_{t_{\min}}^{t_{\max}} \frac{\left(10.5 \cdot 10^{-5} \frac{1}{\mathrm{K}}\right)}{17000\ \mathrm{s}} T(t') e^{-\frac{t-t'}{17000\,\mathrm{s}}} dt'$$

6.6

here T corresponds to the temperature data, T_{mean} is the mean or starting temperature. The equation's kernel accounts for the lag time (17000 s) of the thermal bath through the exponential. The factor $10.5 \times 10^{-5} \frac{1}{\mathrm{K}}$ originates from numerical analysis of fused silica substrates used to measure the Young's modulus and Poisson ratio as a function of temperature [47].

The reader should notice the distinct absence of the assumed power absorbed. This equation focuses on detangling frequency shifts due to the thermal bath. Resulting frequency information must be fit using the appropriately time evolved FEM model.

The model drawn in Figure 6-11 places the HR coating at $z = 0$. The AR coating is depicted at $z = -10\ cm$. Models that incorporate an active arm set boundary conditions that correspond to high power originating from the arm cavity.

A heated model's thermal cross section appears as shown below. One can see that the majority of the heat load affects the first few centimeters of central material. Much of the heat is down converted and radiated back into the environment at the HR surface.

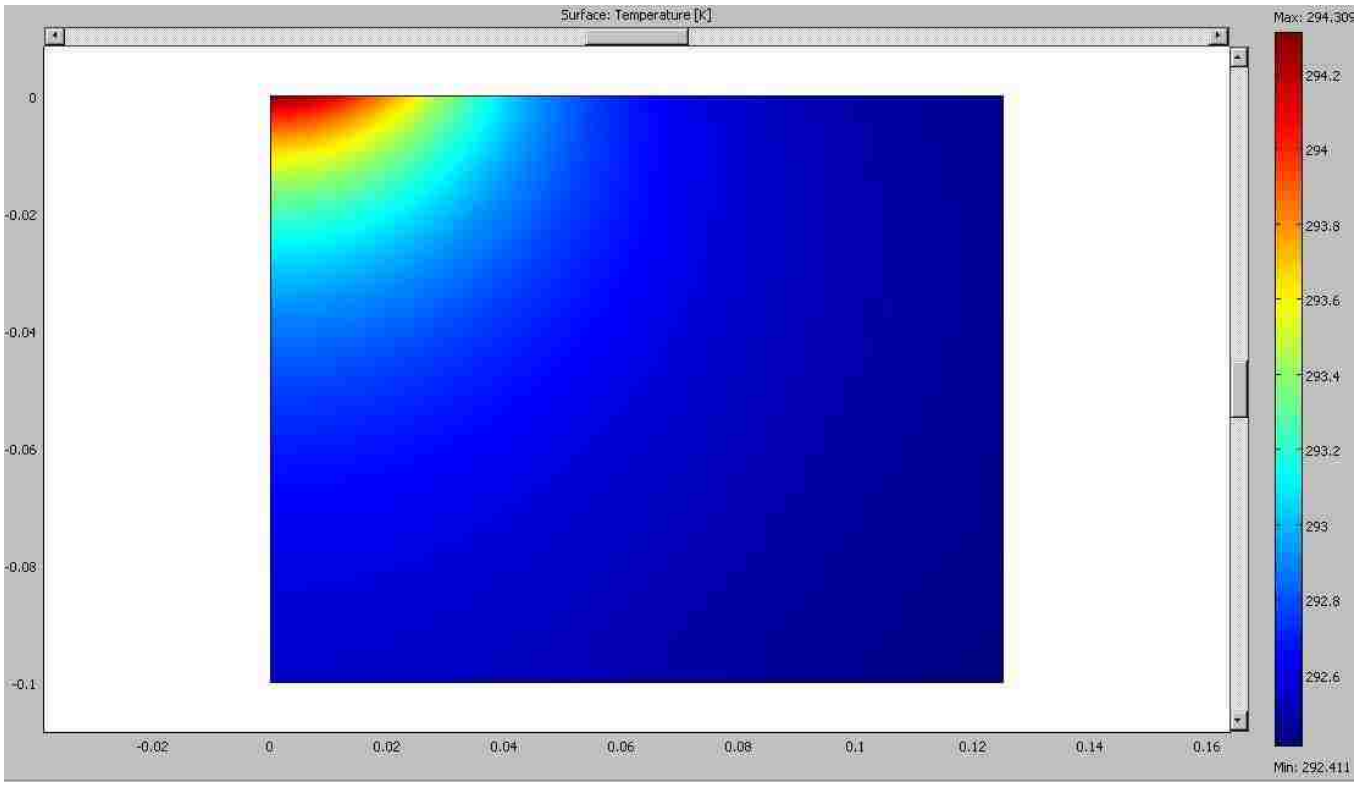

Figure 6-11: A solved 2 dimensional FEM model of a ITM under thermal load. In this model, the LIGO Livingston interferometer is fully locked an powered at 8 W. The horizontal axis represents radial distance in meters. The vertical axis represents axial distance in meters. The HR coating is located at z = 0. ITMy's center sits in the upper left of this image. From this image it is apparent that most Nd:YAG heating occurs near the HR coating.

The relative frequency shift of the data is plotted in Figure 6-10 and is further illustrated in **Error! eference source not found.**. The plot depicts rapid transitions as well as regions of "stability." Using the FEM model with time evolution with oscillating incident powers, we obtainFigure 6-12.

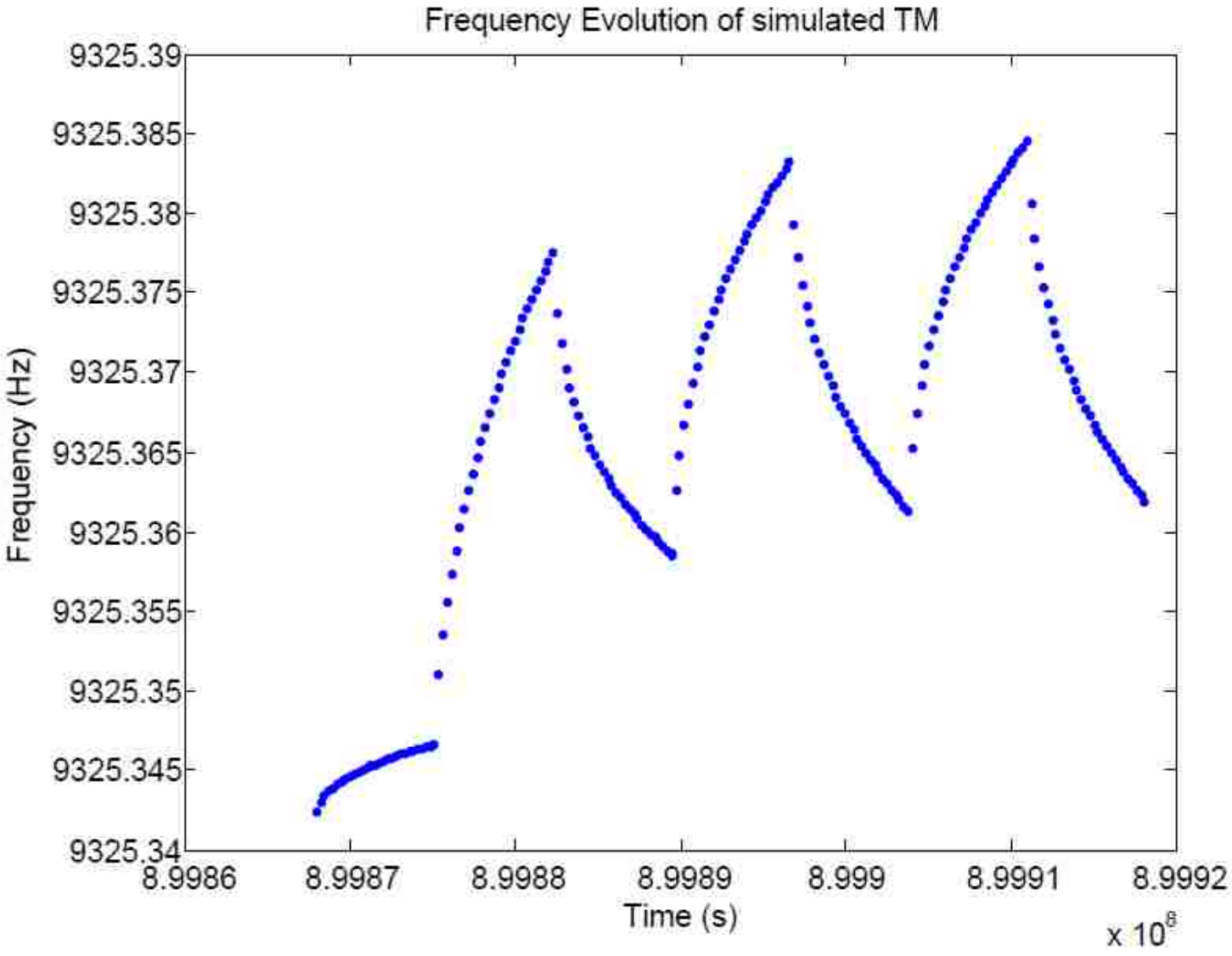

Figure 6-12: A time evolved frequency data from the FEM model with respect to GPS time in seconds. This model has incident power identical to the data plotted in subplot 3 of figure 6—11. Absorption parameters have not been adjusted in this model.

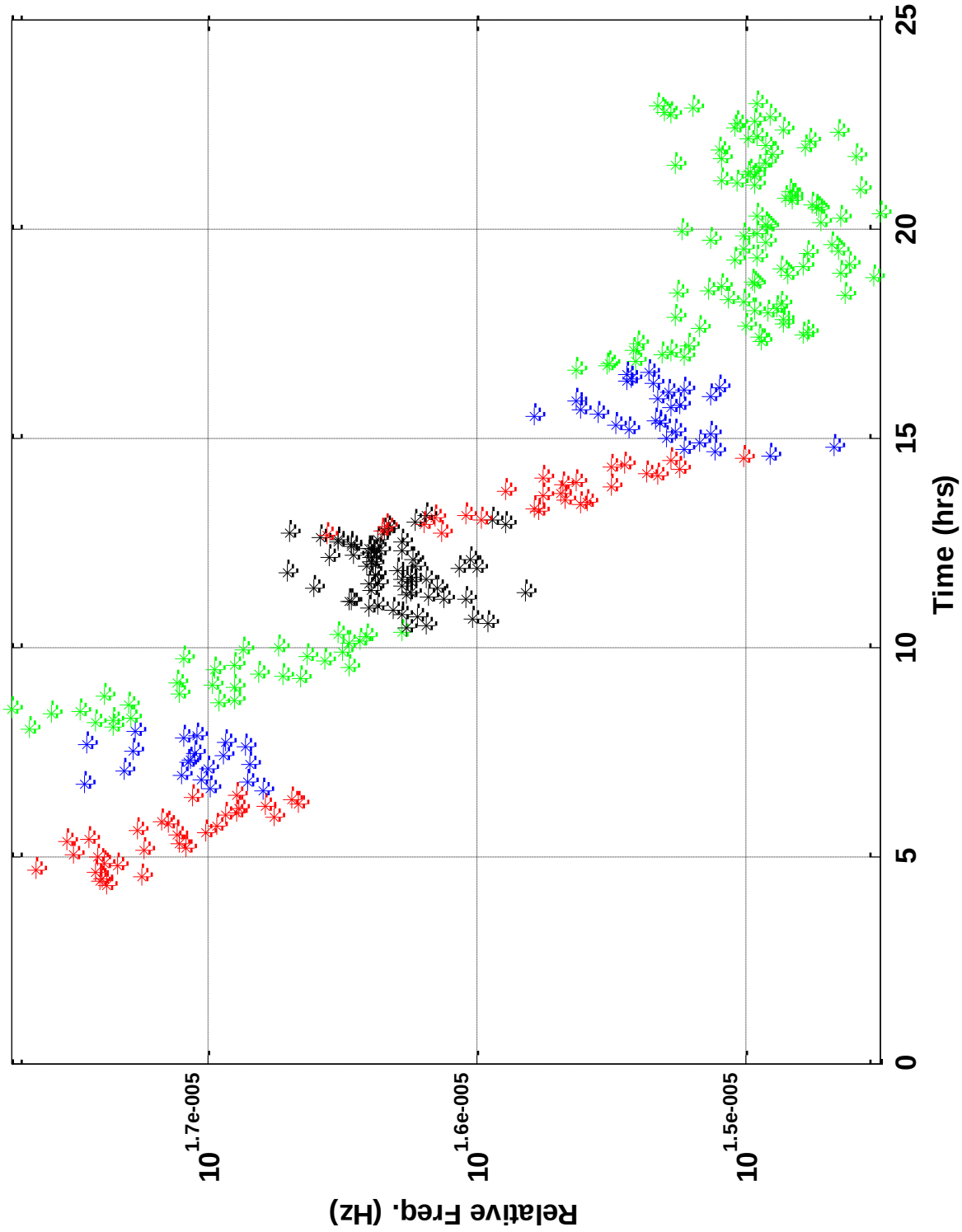

Figure 6-13: Relative frequency shift data for ITMy as a function of time. The base frequency is 9328 Hz in this analysis. The vertical axis represents relative frequency.

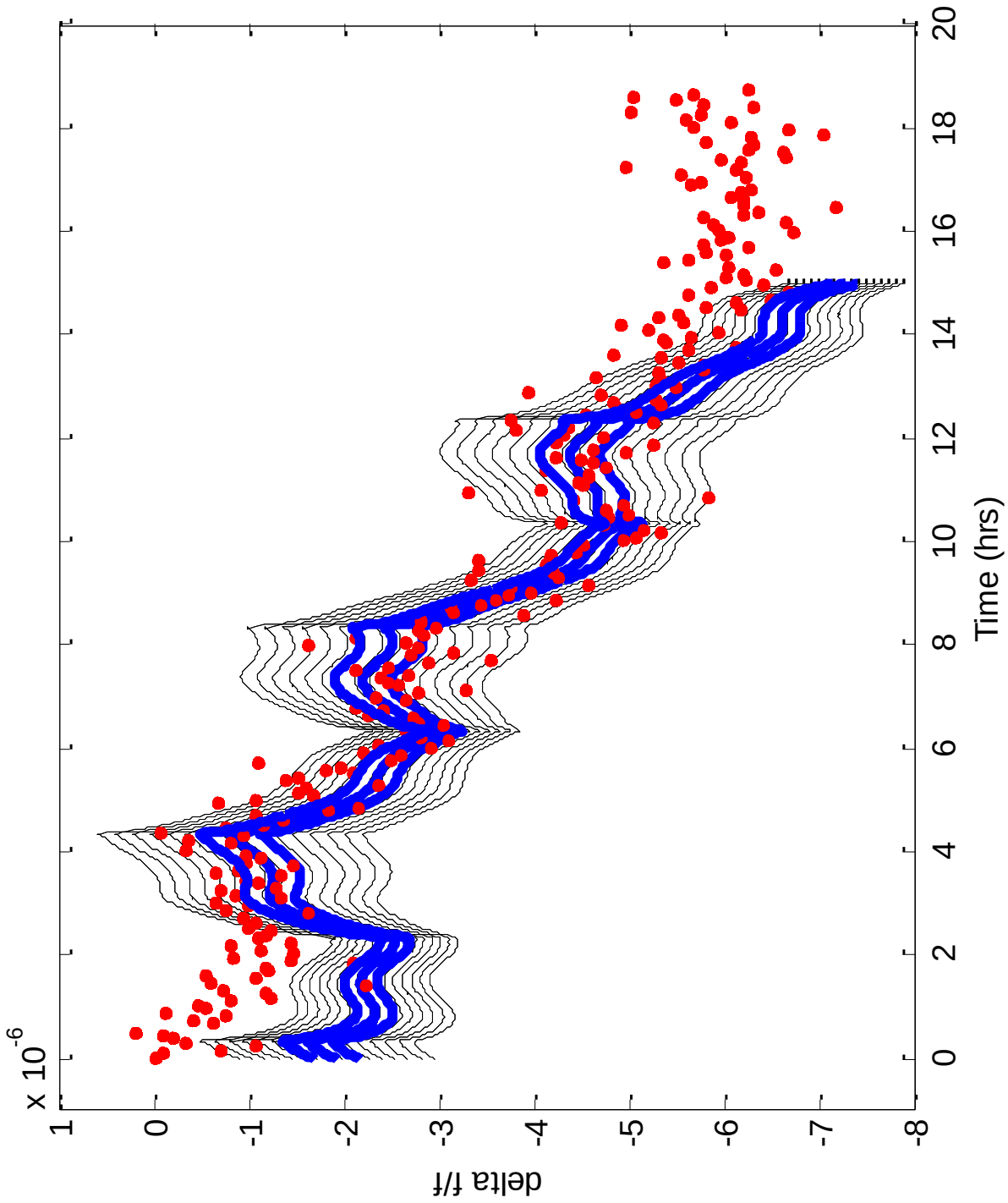

Figure 6-14: ITMx's time evolved FEM simulation is shown superimposed on relative frequency shift data. The family of curves represents results from the fitting. The two outer blue lines indicating 10 % error are plotted around the central blue best fit curve. Only the coating absorption term was used to generate this plot.

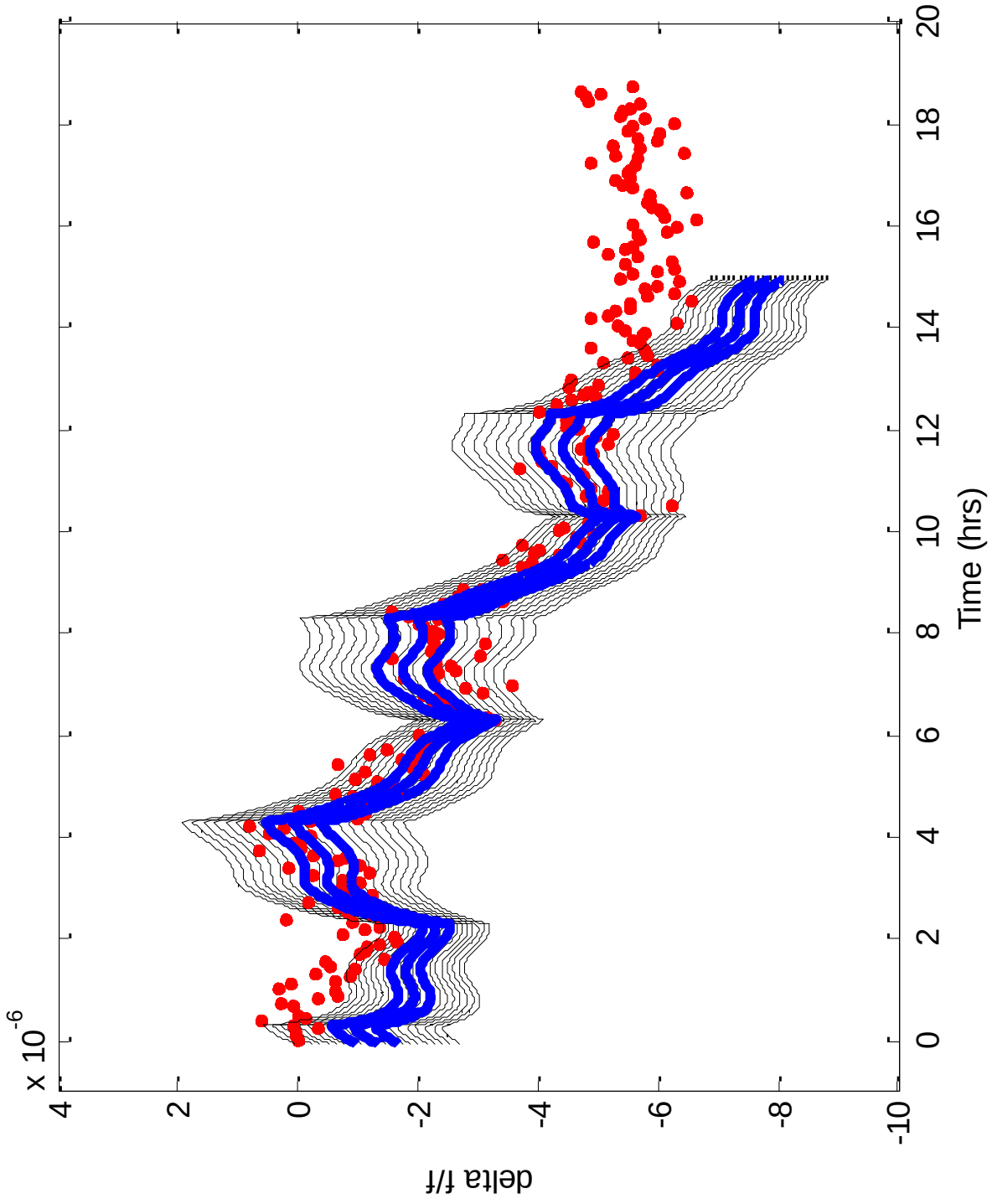

Figure 6-15: ITMy's time evolved FEM simulation superimposed on relative frequency shift data. The family of curves represents results from the fitting. The two outer blue lines indicating 10 % error are plotted around the central blue best fit curve. Only the coating absorption term was used to generate this plot.

Adding the thermal history to the time evolved FEM simulation, the best fit results are displayed in figures **Error! Reference source not found.** and **Error! Reference source not found.**. Here the best fit rves vary coating absorption, substrate absorption, and time delay. Ten percent error curves are plotted around a middle blue best fit. The aforementioned figures were constructed with ONLY the coating absorptions activated. The quality of the fit implies that almost all the absorption takes place at the coating. Table 6-1denotes the results.

The time evolved FEM program performed well through most of the periods. Initial and latter points failed due to an imprecise base frequency guess, inaccurate inclusion of thermal history, and time delay. The simulations failed at very late times because only power cycling times were simulated. The extended quiescent time was not modeled. It is however used in chapter 7.

Noise in the data shown is believed to originate from control signals near the body mode. Occasional drive from the local alignment control loops were believed to change the resonance. Limited time restricted further investigations into this hypothesis. Other possible noise sources still remain unknown. However, long time series data prevents short fluctuations from dominating the measurement.

Table 6-1: Fitted absorption ratios of the LIGO Livingston ITMs on December 2009..

Mirror	Absorption Ratio
ITMx	3.5 ± 0.35 ppm
ITMy	5 ± 0.5 ppm

6.3 Measuring ETM Absorption

For a complete thermal model, the other four core optics should also have been evaluated. Of the remaining optics, the most important were the ETMs. The analysis for the ITMs could have easily been ported for the ETMs with the appropriate frequency changes. The difficulty in determining the absorption values was the all important thermal history. The temperature sensors' power and data conversion circuits had failed prior to data acquisition. Since the ETM chambers had not been opened, quantities posted in the LIGO Livingston on-line detector group logbook have been not been verified. Most recent measurements indicate absorptions of 4 ± 2 ppm as measured in Feb 2007 [48].

6.4 ITM Integration into Simulations

In the following sections, comparisons are drawn between thermal full interferometer simulations and phenomena observed in the LIGO interferometers. The thermal simulations were hybridized FINESSE/FEM models emphasizing the ITMs. The final section of chapter 6 was observed first at LHO by LHO's TCS crew, C. Vorvick and D. Atkinson before being reproduced at LLO by the author.

The algorithm for the full interferometer code is rather simple. A MATLAB based script calls the COMSOL FEM to compute the appropriate thermally induced variations in the index of refraction. The FEM code also simulates surface expansion. The main MATLAB script calls FINESSE after making two dimensional maps to cover the face of the input mirror. FINESSE proceeds to calculate the user request. MATLAB is finally called to plot the result.

6.5 Phenomena due to Mirror Heating

6.5.1 Comparison to Phase Camera Results

Often in experimental optics, it is useful to look at or image the laser beam itself at some point in the detector. A device that directly imaged the average RF sideband field and carrier field structure inside the interferometer was called a phase camera. This device raster scanned an enlarged beam across the face of a (New Focus™ 1811) photodiode far smaller in size. The photocurrent was recorded as a function of scan position. The double demodulated signal yielded an average spatial profile of the average RF sideband field distribution. The remaining DC component represented the carrier spatial profile [10].

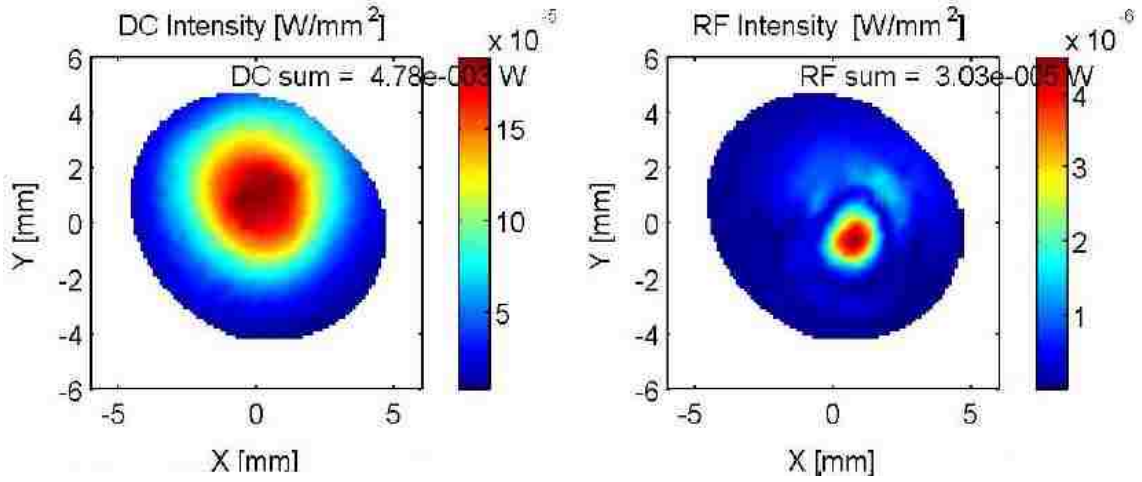

Figure 6-16: Phase camera images from Jan. 2004 taken at the ITMy pickoff port during a full interferometer lock are shown above. The images show the size of the carrier in a cold PRM (left) versus the average size of the 24.5 MHz RF sidebands (right). Notice how the sidebands appear to possess higher order modes and the sideband's average light is not centered with the carrier. Image ellipticity is due to improper alignment of the phase camera.

Reference [50] obtained measurements of RF sideband fields form the Hanford detector. Similar RF sideband measurements were made at the Livingston detector in 2003 and 2004. In both instances sideband images are characteristically smaller than their carrier components. Further, phase camera images indicate the sideband fields changed position from interferometer lock acquisition to interferometer lock acquisition [51]. This was also true from the lock acquisition to running power.

A sample of the carrier and averaged RF field distributions are shown in Figure 6-16. These images were taken with the LIGO Livingston interferometer in a fully locked state at low power [51]. The reader should notice the distinct difference in beam size between the carrier image on the left and the average RF sideband beam on the right. The sideband image shows ring structures due to higher order modes contributions. Also the centroid of the sidebands are not aligned with the carrier beam. The driving reason for the anomalies is discussed in chapter 1 and 5. The carrier beam's mode wass dominated by the beam parameters of the 4 km arm cavities. Whereas the RF sidebands were only resonant within the unstable PRM. The image ellipticity was caused by operator error. The camera was not setup normally to the incident light.

Elaborate details can be found in references [50] and [51]. These measurements were taken before installation of the iLIGO TCS. Simulations using LIGO mirror metrology and in-house Fourier based simulations indicated similar field topologies. These simulations and their agreement with experiment were also indicated in reference [52].

In the spirit of the data and intensive modeling performed for the aforementioned references, the FINESSE simulation of a full interferometer demonstrated similar nuances. Using the LIGO Livingston interferometer nominal mirror curvatures and length values, a full interferometer simulation was constructed and tested in the "cold" state. This mimicked the state of the interferometer during the phase camera experiments in 2003 and early 2004. The results of the simulation shown below appear to be in congruence with experiment.

Figure 6-17 indicates sideband favoring mentioned in chapter 5. It also indicates the intensity pattern of one of the sidebands presents a winged pattern at ITMy pick-off port. FINESSE generated camera a images of the carrier and individual RF sidebands fields at the ITMy pick-off port are shown in Figure 6-18, Figure 6-19, and Figure 6-20. Neither sideband presented the same beam spot size as the carrier. Also the lower sideband image clearly shows the presence of higher order modes. The upper sideband presents a higher order ring pattern. This is difficult to see due to the height of the central peak. This follows the image shown in Figure 6-16. Adding the simulated upper and lower sideband intensities yields the bull's eye pattern observed in the actual phase camera images.

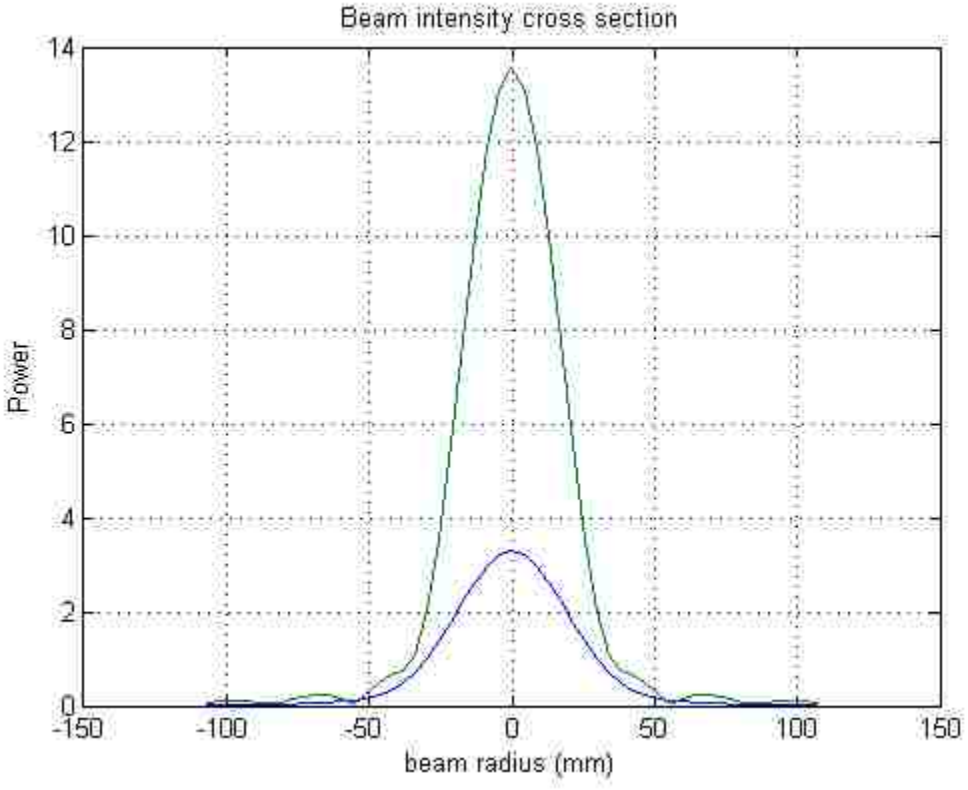

Figure 6-17: A superposition of upper (green) and lower (blue) sideband Intensity distributions as a function of one transverse spatial coordinate. Sideband favoring described in chapter 5 is apparent. Higher order spatial features are also visible in the wings of the lower sideband curve.

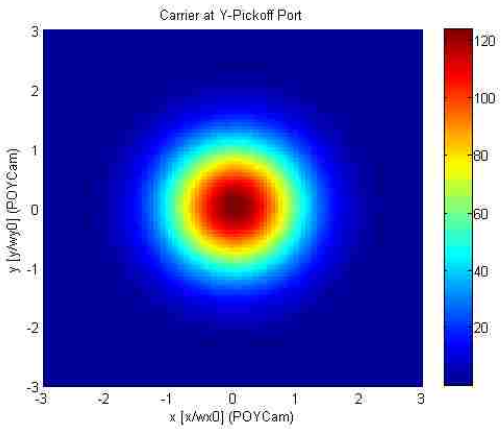

Figure 6-18: A FINESSE based simulation of the carrier beam sampled at the ITMy pick off port. The graphic assumes actual LIGO Livingston mirror curvatures, thicknesses, and distances. The results mimic the fundamental Gaussian mode seen in the January 2004 phase camera measurement. The color scale depicts intensity in units of Watts per square centimeter.

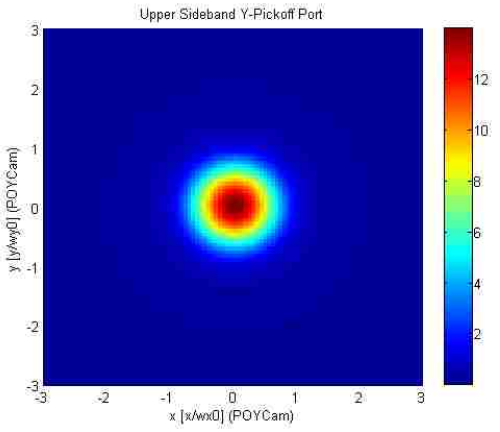

Figure 6-19: A FINESSE based simulation of the upper sideband beam sampled at the ITMy pick off port. The results describe a fundamental Gaussian-like behavior for this frequency. Higher order modes are somewhat visible as a halo around the central peak. The halo visibility suppression was the result of the height of the central peak. The color scale depicts intensity in units of Watts per square centimeter.

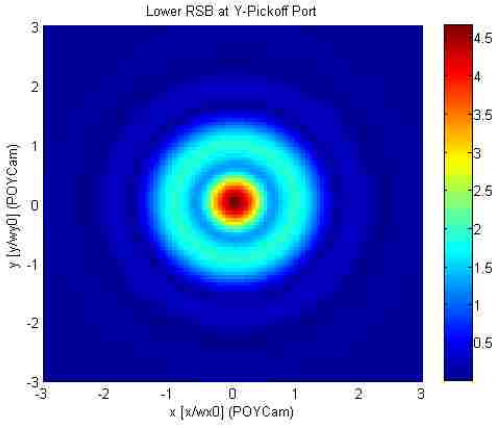

Figure 6-20: A FINESSE based simulation of the lower sideband beam sampled at the ITMy pick off port. The graphic assumes actual LIGO Livingston mirror curvatures, thicknesses, and distances. The results clearly indicate higher order modes comprising this frequency. This is in agreement with the January 2004 phase camera images. The color scale depicts intensity in units of Watts per square centimeter.

6.5.2 AS port Camera and Simulated Interferogram Comparison

Another demonstration of the hybrid interferometer simulation modeled the output of light fields at the anti-symmetric port. Data from the Hanford Observatory taken in January 2009 shows interferograms that are made with the TCSy laser incorrectly aligned. Here TCSy refers to ITMy's dedicated TCS bench. The 4 km Hanford detector was in a simple Michelson lock during this image. Matching the transverse offset in the Hanford Observatory's thermal lens lead to a similar interferogram in simulation. The lacking "light" lobe on the left is due to the grid coarseness.

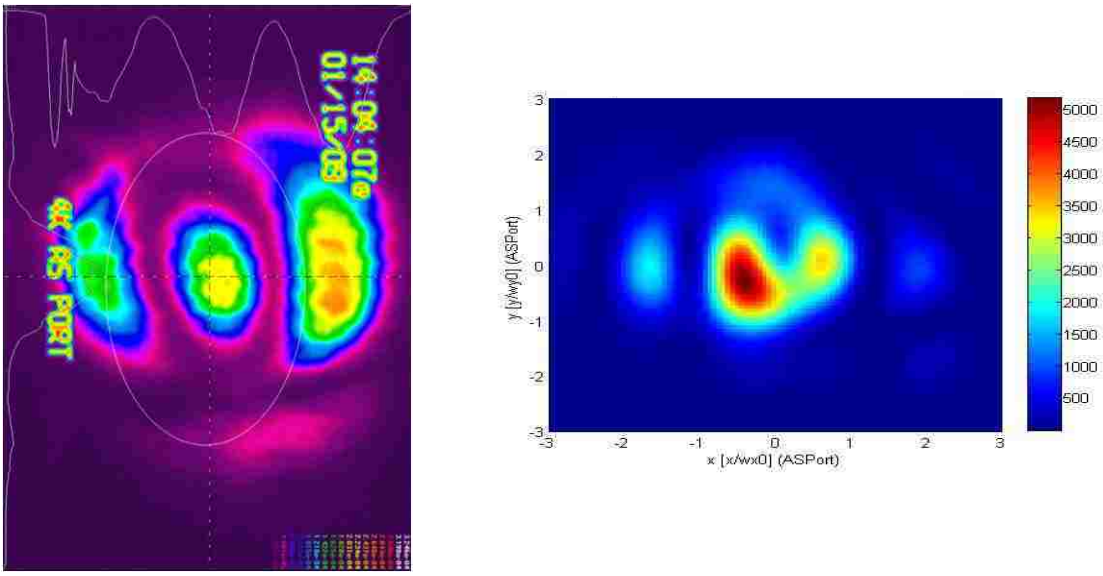

Figure 6-21: The results of a simple Michelson lock at the Hanford detector with the y-arm TCS active. Left: An interferogram taken at the antisymmetric port while the ITMy's TCS was slightly misaligned and active. Right: A simulated interferogram created under the similar circumstances. The lacking left light "lobe" is due to grid coarseness and total number of modes used. The left figure was rotated for its axes to coincide with the model's axes.

The phase map used to generate Figure 6-21 result was developed from a two dimensional axisymmetric model. In this simulation, ITMy was heated by its respective heating laser slightly off center. The resulting simulated mirror thermal aberrations were rotated to create the two dimensional phase map. The phase map was then applied to the FINESSE simulation's ITMY slightly off center. The resulting interferogram shows behavior similar to actual data. In the simulated image, an extra energy lobe is visible to the right of the three largest peaks. It is the opinion of the author that this extra lobe may have been detectable should the Hanford image have been resized appropriately.

6.5.3 Optical Lever Phenomena

Following the installation of improved TCS lasers at Hanford Observatory, a phenomenon colloquially referred to as "TCS induced tilt" appeared in November 2008 data. These phenomena were reproduced at LLO data taken in December 2008. Figure 6-22 displays optical lever data and optical shadow/electromagnet (OSEM) data that demonstrate this effect.

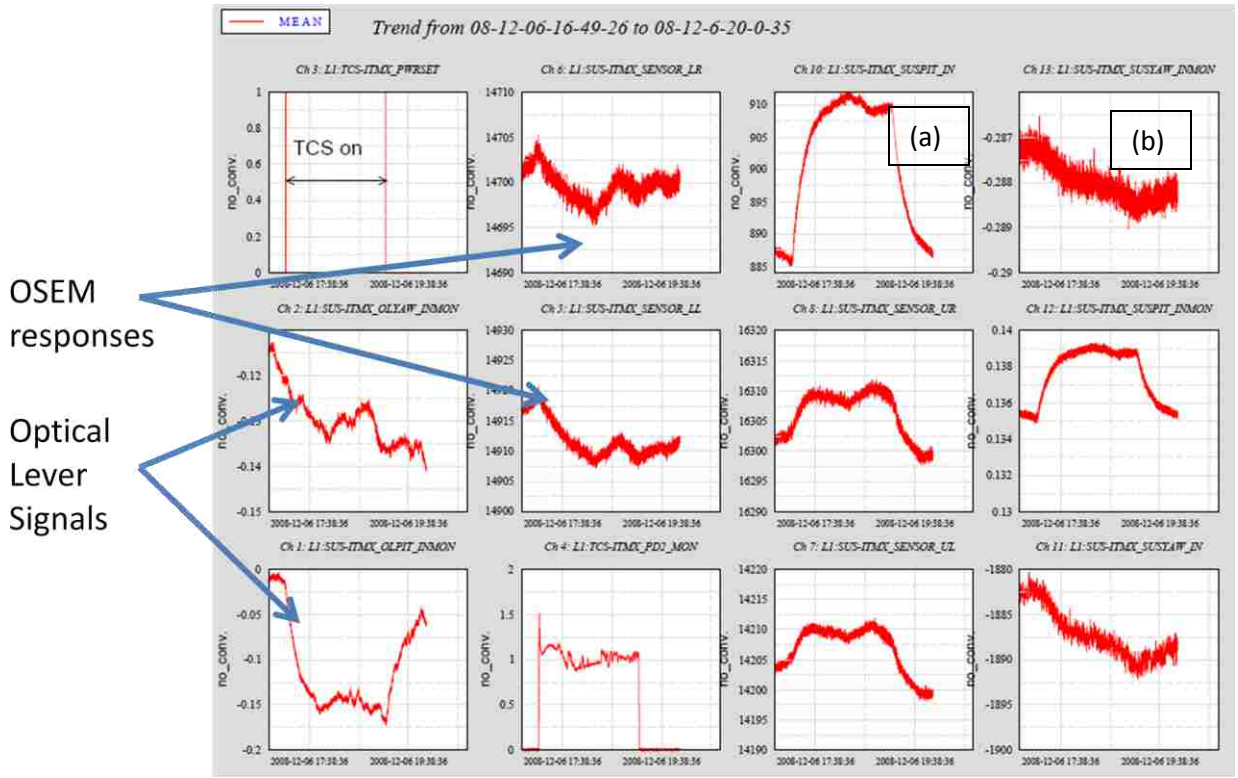

Figure 6-22: Unrefined time series data from ITMx indicating TCS induced tilt. The LIGO Livingston detector was not in any resonant state. The graphs pointed to indicate OSEM and optical lever motion during TCS activation. Similar results occur for ITMy. Notice the sudden deflections in the data after the TCS is activated. The optical levers appear to recover quickly in pitch but not in yaw. Graphs labeled (a) and (b) represent the sum of OSEM signals and demonstrate the most vivid response.

Optical levers and OSEMs were used the suspended interferometer mirrors aligned for lock acquisition. They belonged to a subsystem called angular sensing and control, ASC. A full description of the mechanics and theory of the ASC can be found in references [5] and [53]. In principle, the optical levers sent visible laser light onto the test mass (core optic). The reflected light landed on a quadrant photodiode. The currents read off the quadrant photodiode combined with the knowledge of the travel distance yielded mirror angular orientation.

The OSEMs were used as a local and crude alignment device. Their primary role was to damp unintentional pendulum motion of the optics. Most often their utility was observed during earthquakes or lock loss induced oscillations. OSEMs use LEDs and photodiodes to detect the position of mirror magnets. Because they rely on shadow limited voltage, OSEMs do not have the ability to resolve high precision angular motions compared to the optical levers.

The enhanced thermal compensation system did not generate enough radiation pressure at minimum power to generate this level of tilt. Therefore, the phenomenon could not be that of the optic actually tipping in its suspension. Rather a combination of effects conspired to generate the apparent tilt.

The first effect corresponded to an imperfectly centered optical lever laser spot on the ITM. Optical levers reflected of a point near mirror center. This means they reflected off the curved surface of the mirror. Heating from the thermal compensation system resulted in the mirror surface recurving due to

surface expansion. A perfectly static mirror, therefore, generated a pseudo-tilt signal as the mirror surface deflected.

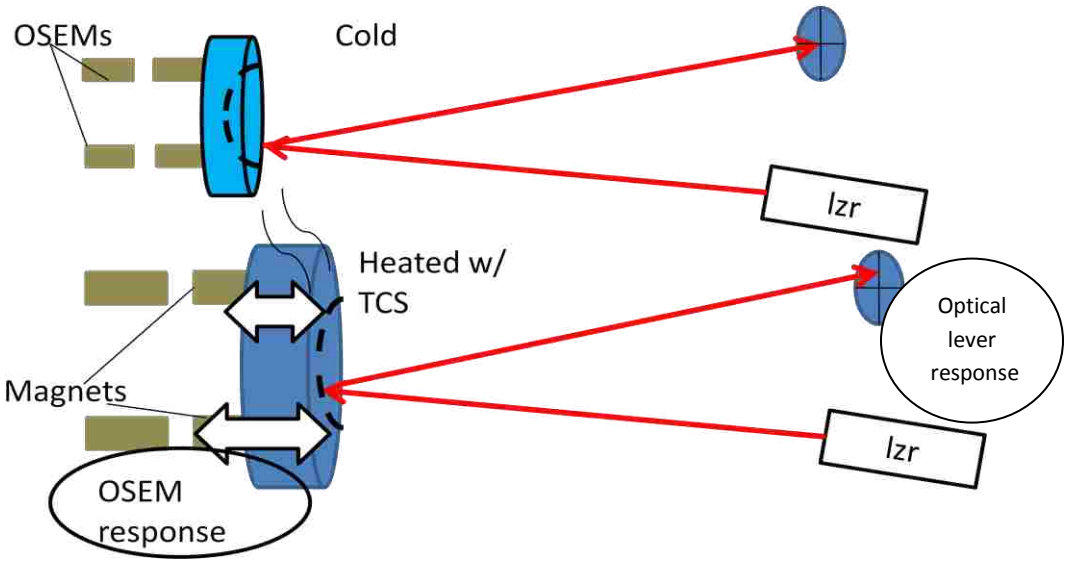

Figure 6-23: Top: A diagram of an optical lever. A visible laser travels 30 m reflects off the mirror and returns to a quadrant photodiodes for angular interpretation. Bottom: A depiction of the optical lever and OSEM deflection following mirror heating.

OSEMs were also responding to this false signal. The actual suspended optic tilted due to the ASC loops reacting to the false optical lever signal. This lead to an average tilting noted in the signals. However, the OSEM signals indicate a differential component between the sensors that did not correspond to the optical lever deflection. This differential effect was attributed to differential expansion of the optic.

Measurements made at LLO for each ITM are recorded in Table 6-2. The detector was set in a powered down condition. Both TCS benches were set to deliver a 1 W annulus pattern beam. After 40 minutes of heating, the data recorded was converted using known optical lever calibrations.

Table 6-2; Measured TCS pitch and yaw induced deflections

	ITMx	ITMy
Pitch	4.4 μrad	2.4 μrad
Yaw	2.6 μrad	0.5 μrad

Thermal models based on absorption measurements suggested the optic could expand by roughly 4 microns. Using the thickness of the mirror, an order of magnitude estimate can be made for angular deflection of the optical lever beams. The result of 10 micro-radians overestimates the measured values by at best a factor of two. According to a second model composed by P. Willems at California Institute of Technology, the differential expansion detected by the OSEMs was roughly 0.2 μm [54]. This induced a possible 5 μrad of tilt counter optical lever deflection. The difference of these two predicted plots comes within 12 percent of the largest measured value.

7 Error Signals for the Thermal Compensation System

7.1 Introduction and Review

This chapter examines a hypothetical means to monitor the thermal lensing with a LIGO detector. Predictable monitoring signals would permit commissioning teams to install control servos that command the thermal compensation systems promoting detector sensitivity. During S5, LIGO Livingston's thermal compensations system was the only subsystem not controlled by the detector's computers. Rather, the Livingston commissioning team manually charted the thermal lensing parameter space. This tuning method was limited by the signals available.

Chapter 1 mentions the special position of the ITMs in the detector. Not only do they contribute to the power build up in the arm cavities, they serve as intracavity lenses promoting stability in the PRM and mode matching between the arms and PRM. It also informs the reader of attempts to passively contend with thermal lensing including the pre-curvature of the ITMs and the initial LIGO TCS.

During the commissioning of initial LIGO, system identification performed during reference [9]'s research indicated two interferometer derived signals that could track the average focal length of the ITM (common mode lensing) and the focal length difference (differential mode lensing). Common mode lensing was monitored by the strength of the beamsplitter pickoff light doubly demodulated at 24.5 MHz. This signal was known as sideband power on the beamsplitter (SPOB). The differential mode was tracked via the antisymmetric port light demodulated in-phase with the 24.5 MHz RF signal.

At LHO, a third means of monitoring the average mode matching based on University of Florida's RF concentric photodiode was used[55]. This scheme measured the amount of first order Laguerre-Gauss excitation (the "Bull's eye" mode) in the PRM via heterodyne techniques. For technical reasons, these spatially sensitive detectors were not installed at the Livingston detector.

7.1.1 Enhanced LIGO's Complications

Exploration of eLIGO's operating parameter space during the post-S5 commissioning period demonstrated nonlinearity in detector derived common lensing and differential lensing signals. When PSL power exceeded iLIGO design point or the TCS was not appropriately tuned, SPOB ceased to respond as initially understood. A larger SPOB did not necessarily lead to a more stable and better performing interferometer. ASi also followed unintuitive trajectories. Managing ASi also did not necessarily improve detector performance or remove perceived differential lensing [56, 57]. This prevented commissioning teams from correctly estimating the focal powers of the ITMs, and therefore appropriately setting the TCS. According to current understanding the ASi was caused by sideband amplitude imbalance. Recall, chapter 5 , chapter 6, and reference [44] suggest that simple amplitude imbalance was not the only source of ASi. Following the installation the OMC, the ASi signal was no longer available during eLIGO operation. This chapter focuses on finding candidate signals, "focus discriminants," to monitor both degrees of freedom at iLIGO and potentially eLIGO operating states.

7.1.2 The Derivation of the ASi Signal

The nature of the ASi has been somewhat mysterious for the reader. It has been referenced in chapter 5 and references [5], [9] and [50]. Here a second layer of detail is put forth to explain the generation of ASi at the LIGO detectors' output (AS) port. The ASi signature originates from essentially two points in the detector. The non-optical source was induced within the RF distribution network. Incorrect phasing of the two 24.5 MHz signals at the photodetector's mixer inadvertently generated ASi and ASq. The optical component originates from mode overlap issues in the PRM between the carrier and 24.5 MHz sidebands. This phenomena was measured at LHO and is noted in reference [9]. An electronic servo mitigated this issue within the RF photodiodes at the AS port during S5. Below a basic mathematical treatment is shown demonstrating the optical generation of ASi. An extension to this analysis is given in appendix C.

Begin by assuming a fundamental Gaussian beam is incident on the RM. Also assume the injected beam has a Gaussian beam parameter "q."

$$E_{in} = E_0\{J_0(\Gamma)[TEM_{00}]e^{-i\omega t} + J_{-1}(\Gamma)[TEM_{00}]e^{-i(\omega-\Omega)t} + J_1(\Gamma)[TEM_{00}]e^{-i(\omega+\Omega)t}\}. \quad \textbf{7.1}$$

Here

$$TEM_{00} = \frac{1}{q(z)}e^{-\frac{ik(x^2+y^2)}{q(z)}}.$$

A more general variant of the Gaussian modes using beam parameters is written in appendix A.

Since all injected terms have the same spatial profile, the weighting coefficient is the first order Bessel function. It derives from the physics of phase modulation. Reflected fields from the cavity are affected by the cavity's reflection parameter, $F(\omega)$.

$$F(\omega) = \frac{r_1 r_2\left(e^{i\phi} - 1\right)}{1 - r_1 r_2 e^{i\phi}}. \quad \textbf{7.2}$$

Here $\phi = 2\pi f L/c$, and r_1 and r_2 are the reflectivity amplitudes of the RM and the ITMs.

If the reflected fields are comprised of only fundamental Gaussian modes then we can express the result as follows:

$$E_{refl} = E_0[TEM_{00}]\{F(\omega)J_0(\Gamma)e^{-i\omega t} + F(\omega+\Omega)J_0(\Gamma)e^{-i(\omega+\Omega)t} + F(\omega-\Omega)J_0(\Gamma)e^{-i(\omega-\Omega)t}\}. \quad \textbf{7.3}$$

As written in reference [50], the demodulated power can be determined by the following integral modulo the impendence of free space.

$$P_{refl,i} = \int_0^{2\pi/\Omega} E_{refl}\, E_{refl}^{*} \cos(\Omega t)\, dt.$$

$$= |E_0|^2\big((A_c A_{s+}^* + A_c^* A_{s-}) - (A_c A_{s+}^* + A_c^* A_{s-})\big).$$

7.4

If the sidebands are the same amplitude, this integral is zero.

Extending this to higher order modes, the reflected result is shown. Now assume that the cavity reflects the first higher modes of the sidebands.

$$E_{refl} = E_0\{F(\omega;00)J_0 e^{-i\omega t}[TEM_{00}]c_{00,c}$$

$$+F(\omega+\Omega;00)J_1 e^{-i(\omega+\Omega)t}[TEM_{00}]c_{00,s+} + F(\omega-\Omega;00)J_1 e^{-i(\omega-\Omega)t}[TEM_{00}]c_{00,s-}$$

$$+F(\omega+\Omega;10)J_1 e^{-i(\omega+\Omega)t}[TEM_{10}]c_{10,s+} + F(\omega-\Omega;10)J_1 e^{-i(\omega-\Omega)t}[TEM_{10}]c_{10,s-}.$$

7.5

$$E_{refl} = E_0\{A_{00,c} + A_{00,s+} + A_{00,s-} + A_{10,s+} + A_{10,s-}\}.$$

7.6

The reflection coefficient is both frequency and mode dependent. This is shortened to be included in the reflection's amplitude coefficient. Weighting coefficients have been introduced have been for energy conservation. Demodulating these terms results in an integral similar to equation 7.4. This integral must be modified by a spatial overlap integral to correctly compute power. The result has an imbalance attributable to the extra spatial modes being larger than the carrier.

7.2 Simplified Model

Ideally one would track the evolution of field spatial geometries using Shack-Hartmann detectors or several more "Bull's eye" wavefront sensors. At the writing of this paper, the Advanced LIGO is being designed to incorporate Shack-Hartman devices into its monitoring scheme. Enhanced LIGO was limited in its ability to measure wavefront deformations to high precision and to the number of available output ports in the physical detector. This was the same difficulty found in iLIGO.

To model the interferometer, a few simplifications are made. These restrictions are necessary to retain model validity and to reduce overall CPU time and memory load. The first assertion made for the model is that both iLIGO and eLIGO were optimally sensitive to gravitational waves when they were entirely mode matched to the injected beam. Perfect mode matching is computed by computing the fundamental mode set by the RM and ETMs. Nominal mirror curvatures and distances of the Livingston detector are used. ITM curvatures are set to match the fundamental mode at their respective coordinates.

The model concentrates on (the dominant) spherical aberrations due to thermal lensing. For such a low order effect, the thermal lenses used in chapter 6 are summarily dismissed. Instead spherical lenses were paired with curved mirror surfaces to portray the ITMs. The level of similarity of a spherical lens on a transmissive Gaussian wavefront is noted in chapter 5. Using lenses native to FINESSE permitted

faster simulation times due to lower CPU and memory loads. For the rest of this chapter, the spherical lenses are referred to as "faux" thermal lenses.

The operational state of the model is designed to mimic initial LIGO's S5 operational state. The iLIGO detectors represent the prototypical power recycled Michelson Fabry-Perot topology. While eLIGO was already operational during the writing of this dissertation, its upgrades did not affect the core optics. Therefore, the numbers of complications including eLIGO's new output filters are reduced.

As with preceding models in this dissertation, the LIGO faux thermal lens model is constructed in FINESSE. An assertion is made that the dead band servos in FINESSE would correctly simulate detector length locking servos. LLO and LHO's detectors maintain mirror separation necessary for low-noise operation via its four linear (time based) servo control loops [5]. FINESSE's servo subroutines operate in the frequency basis. This meant that user-prescribed mirrors were iteratively moved to minimize user provided control signals; this is noted in chapter 4 and reference [33]. This zero finding procedure essentially behaved like a simple control loop with an integrator. Accuracy thresholds for these "servos" control signals indicated the region where a FINESSE control loop failed. Actual RMS fluctuations of the length degrees of freedom are taken from reference [5] and encoded as control loop accuracy thresholds. Prior to implementation, each discriminant signal's demodulation phase is carefully tuned to its length degree of freedom. This tuning scheme is also true in practice. In the end, it improved length servo response and interferometer lock fidelity.

7.2.1 Computing the Replacement the Thermal Lenses

A pair of additional steps is required to replace the FEM based thermal lens phase maps with compound thermal lenses. The FEM shown in Figure 5-23 indicates that the heated zone sits rather closely to the highly reflective coating. A simulated compound lens therefore should have very little distance between the thin fixed curvature mirror and its faux thermal lens. The amount of distance between a spherical lens and its partner thin mirror cannot be zero. This violates program rules in FINESSE. Since the Rayleigh range of the LIGO beam is on the order of kilometers, placing the weak faux thermal lens adjacent the ITM AR coating has no significant effect on the results.

Table 7-1: Mirror Parameters

Mirror diameter	0.25 m
Empirical auxiliary beam annulus thickness	0.0254 +/- 0.002 m
Nd:YAG spot size on an ITM (calculated)	0.0387 m

Second to correctly model the thermal lens, the number of modes must be high enough to sample the thermal lens. This begins with writing down the mirror parameters. A few important items are relisted in Table 7-1. The smallest term is the TCS annulus thickness, entry #2. This term sets the limit on the mode order. Estimating the number of modes is shown in equation 7.7.

$$\text{Spatial Period} = \frac{4\omega}{\sqrt{n}}. \tag{7.7}$$

Now, one can solve for the number of modes.

$$\sqrt{n} = \frac{4 \cdot 3.87\ \text{cm}}{2.50\ \text{cm}}$$
$$n \approx 38 - 39\ \text{modes}.$$

A maximum spatial mode set of $n + m = 12$ yields a spatial resolution limit of ≈ 4.47 cm. A one centimeter resolution requires a maximum mode number of 240. This level of mode number becomes the domain of the FFT or SIS models.

The locking routines of FINESSE were required to operate rapidly, robustly, and routinely throughout the examination process. This requirement permitted me to reduce the maximum number of modes from 12 to 8. Precision is not greatly affected in this model regime as shown in convergence tests. Time to solution is, however, reduced from 2-6 hours to 10-30 minutes..

7.2.2 iLIGO Model Configuration

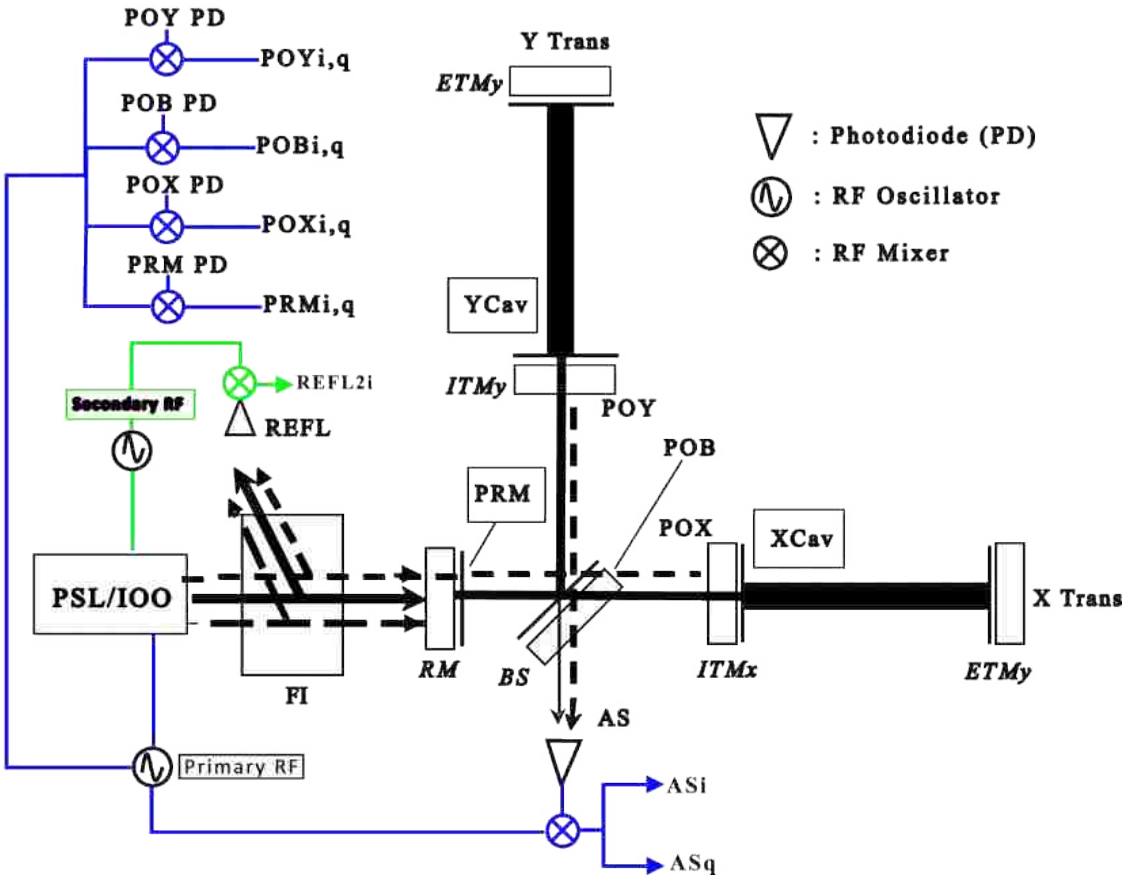

Figure 7-1: A schematic of the initial LIGO configuration with optical pickoffs. The mirrors are labeled in italic font. Vertical lines adjacent mirrors indicate which side is highly reflective (HR). The carrier and sidebands are shown as solid or dashed black lines. The primary sideband light leaks out the antisymmetric (AS) port due to an asymmetry in the ITM to BS distance. Light pickoff (PO) ports are drawn close to their nominal positions. The boxed pickoff ports (XCav, YCav, and PRM) are ports used for diagnostic purposes and signal fidelity. Primary and secondary RF oscillators in the lower left provided both RF excitations for phase modulations and demodulation at photodiode mixers. AS port light demodulated quadrature signals are shown. Demodulated signals are noted with their port name in capitals and the quadrature in lower case. Demodulated signals generated from the secondary RF are noted by a "2." Other demodulated signals are shown in the upper left for diagrammatic simplicity.

Figure 7-1 again depicts the initial LIGO interferometer. Mirrors, labeled in italics, are shown with secondary black lines indicating the high reflective surfaces. Optical pickoffs are labeled in normal font.

Pickoffs whose names are boxed were used for diagnostic purposes or used to satisfy FINESSE. Colored lines and associated oscillators indicate RF signals that were used to both excite sidebands and demodulate the optical signals. For clarity, only five 24.5 MHz (primary) demodulation and one 61 MHz (secondary) signal pairs are shown. One should understand that all optical pickoff ports are demodulated at both radio frequencies. Length control error signals are set to resemble the actual detector as closely as possible.

7.2.3 Simulated Tests and Sifting Through Results

As implied, only two mirror's focal powers are altered in the simulated experiments. Therefore, only two experiments are required. Pure common lensing is induced by identically changing the focal lengths of both ITM's faux lenses. Differential lensing is induced by setting both ITMs lenses to equal but opposite focal powers. In both scenarios, only the ITMx's focal power is recorded for plotting. In all simulations run, the abscissa zero represents perfect mode matching. Each test consists of nearly 2000 data points, and results are plotted in units of demodulated optical power or DC intensity versus focal power in units of diopters. Unlike the common lensing experiment, the differential lensing experiment could not begin at ITMx focal powers beyond $-5 \times 10^{-5}\text{diopters}$. This is explicitly due to the lack of interferometer stability at the starting point.

Since the simulations generate a variety of signals, stipulations are needed to determine which signal might be a viable candidate for actual LIGO detectors. These requirements are listed below.

1) The most important restriction requires signals to be acquired from light pickoff ports easily implemented in the LIGO detectors. Non-existant light ports would require costly changes to the vacuum system.
2) Although sensors that employ spatial phase measurement have been developed [9], in this work we seek simpler signals derived from DC light intensity, RF light intensity, or RF signal phase.
3) Both common and differential lensing signals must be usable in the presence of length sensing and control servo action. The length sensing and control system can corrects small changes in optical phase delay induced by ITM motion. The focus discriminants must depend on ITM focal values only.
4) Discriminants are ideally linear with respect to their degree of freedom near the desired operating point. Signals that do not cross zero at perfect mode matching or non-linear need not be excluded in this study, since a linear servo may not be necessary.

7.2.4 Restricting the Solution Abscissa

Not only must the solutions be sorted into viable candidates, the solutions must be limited. A large focal parameter range is examined. Therefore, the results need to be restricted to focal powers that are physically plausible during LIGO operation.

The most coarse abscissa restriction for both common and differential lensing simulations are influenced by arm power loss. The focal power values are analyzed until the interferometer simulations are not able to retain power within the arm cavities. For both simulations, the focal power chosen was $5 \times 10^{-5}\ \text{m}^{-1}$. At this focal value, arm cavity circulating power drops by nearly one percent.

This larger range envelopes the focal power perturbation estimated from the measured absorption of the ITMs as noted in chapter 6. Combining the more absorptive ITM's absorption ratio with equation 5.19 corrected for coating absorption, the resulting thermal focal strength is $2.1 \times 10^{-5}\ \mathrm{m}^{-1}\ \pm 3\ \%$. Using FEM simulation and a prediction also based on relative frequency changes yields an estimated focal power of $1 \times 10^{-5}\ \mathrm{m}^{-1}$. Using the lesser of the two yields a more conservative result.

7.2.5 Results

The summary of all the candidates are listed in Table 7-2. To our misfortune, no signal behaves like a prototypical discriminant. Instead particular patterns pointed to associated focal powers and their signs. Note that all beamsplitter pickoff signals do not include the attenuation of the BS AR coating.

Table 7-2: Candidate Signals for Thermal Lens Monitoring

Signal Candidate	Characteristics
(Common Mode)	
Beamsplitter Pickoff Light Double Demodulated at the Primary Sideband RF	Maximum Excursion: 1.5 W (at BS AR coating) Slope at Operating Point: $\approx -4 \times 10^{-6}\ \frac{\mathrm{W}}{\mathrm{diopter}}$
Beamsplitter Pickoff Light Demodulated In-Phase with the Primary Sideband RF	Maximum Excursion: 1.5 W (at BS AR coating) Slope at Operating Point: $253\ \frac{\mathrm{kW}}{\mathrm{diopter}}$ DC offset: -0.4 W.
Antisymmetric Port Secondary Sideband Light's TEM22 Mode	Maximum Excursion: $10^{-4}\ \sqrt{\mathrm{W}}$ Slope at Operating Point: 0 (zero) DC offset at Operating Point: 0
(Differential Mode)	
Beamsplitter Pickoff Light Demodulated in Quadrature Phase with the Secondary Sideband RF	Maximum Excursion: 10^{-3} W (at BS AR coating) Slope at Operating Point: $33.84\ \frac{\mathrm{W}}{\mathrm{diopter}}$ DC Offset at Operating Point: 1×10^{-5} W

The table clearly indicates that common mode signals were more available then differential mode signals. Differential mode RF signatures present at end station transmission ports would increase the number of differential mode focus discriminants. Nevertheless, the lack of signal strength and lack of RF hardware at the end stations removed these discriminants from the table.

The candidate focus discriminants are plotted below. For those plots that show RF signal data, the plots are split into five subplots. Each plot in the first (top) position represents the candidate signal's behavior. The following subplots denote the activity of the four length control loop demodulated optical signals as labeled in reference [5]. Once more the plotted length control signals are as follows:

- Differential Fabry-Perot Arm Length (DARM) → ASq
- PRM → PRMi
- Michelson → POBq
- Common Arm Fabry-Perot Arm Length → REFL2i

The superimposed dotted lines indicate accuracy thresholds for each signal. The uncontrolled quadratures are also plotted for completeness. No control signal plotted exceeds their prescribed

thresholds. Rapid fluctuations in control signals are indicative of FINESSE's servo scripts functioning correctly.

Signal #1

SPOB has already been in use. Figure 7-2 describes the behavior of SPOB in units of Watts versus focal power. Although this signal was first introduced as being erratic, a simulated sweep of focal power reveals that perfect mode matching does not coincide with maximum power. Rather perfect mode matching coincides with nearly with a local minimum. At first this result is confusing and unsettling. However, the behavior of SPOB can be understood in the following sense. A perfectly mode matched interferometer resonates on only one mode. All other modes are suppressed. If the modal content of a Fabry-Perot cavity is increased the total power encapsulated between the mirrors rises. More levels of excitation means a greater capacity to store optical power. The asymmetric response of the SPOB around perfect mode matching is a result of the geometric losses and asymmetric "dispersion" of the LIGO interferometer. This is discussed in chapter 5. The central peak sits $-1\ \mu\text{diopters}$ from the point of perfect mode matching. The closest corner of the positive lensing plateau sits approximately $1 \times 10^{-5}\text{diopters}$. This is the edge of the conservative focal power threshold set above. To the benefit of commissioning team, though, finding the closest edge of maximum SPOB still places an interferometer close to perfect mode matching.

Signal #2

The second common mode signal that gives true discriminant-like behavior is the beamsplitter pickoff light demodulated in-phase at 24.5 MHz, POBi. Shown in Figure 7-3, the signal crosses zero albeit with an offset. This offset results in the x-intercept equaling $1 \times 10^{-6}\ \text{diopters}$ and a y-intercept of $-0.39\ \text{W}$. A servo that simply nulled the POBi signal would keep the interferometer well within the region of optimal power build up. Since SPOB and POBi are acquired from the same pickoff, the signals may be combined. The point that the two signals describe opposite derivatives would also be within optimal operating parameters. POBi's primary drawback is its current involvement in the length sensing and control of the PRM [5]. If the PRM control signal can be extracted from another port, for example the POY or POX, POBi could be a worthwhile investment.

Signal #3

The third signal is an unexpected surprise requiring special attention if it is to be implemented. The 61 MHz upper and lower sideband's HG_{22} component can be detected using a scanning non-degenerate Fabry-Perot cavity. The ratio of upper to lower sideband strength is a function of common mode lensing. A perfect mode matching the ratio is exactly one. Although this signal's fidelity is far cleaner than preceding signals, it has two detractions. The first and perhaps most obvious issue is the strength of the 61 MHz HG_{22} mode. Plotted in Figure 7-4 are the sideband amplitudes (units of square root Watts). To convert to units of detectable Watts, one would square the plotted results. A signal this small would be overwhelmed by adjacent peaks. The second issue with this signal is its reliance on a scanning Fabry-Perot cavity. Such devices are prone to back scattering light into the LIGO interferometer. This has an immediate effect on sensitivity and was observed during preliminary OMC tests in 2007.

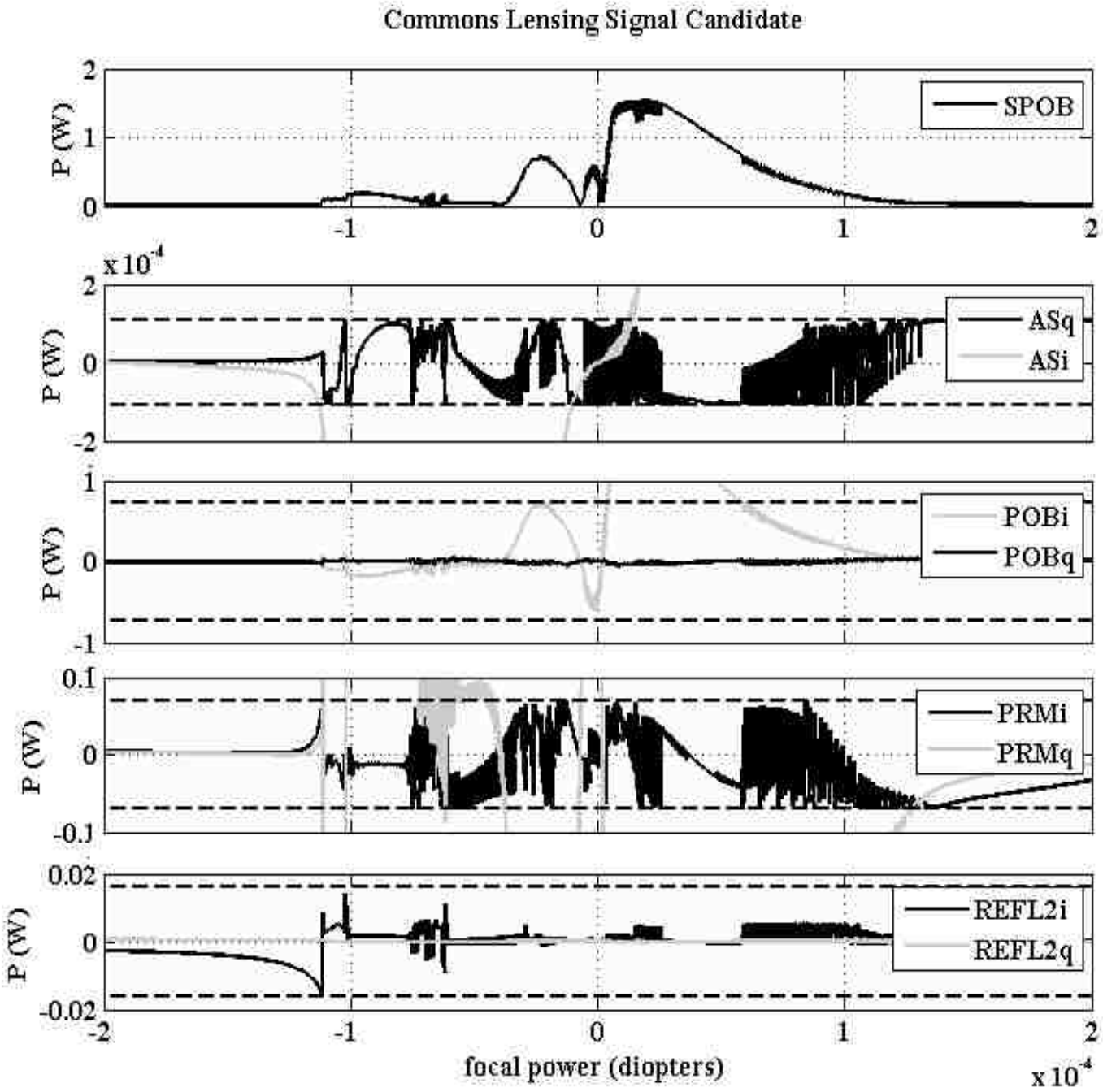

Figure 7-2: Common lensing signal candidate #1 and control signals. The top trace plots the behavior of beamsplitter pickoff light doubly demodulated at 24.5 MHz (SPOB) as a function of common focal power. In the following traces, the letters "i" and "q" refer to the demodulated phase quadrature. The following traces, in order, correspond to the various degree of freedom error signals: ASq = differential arm control; POBq = the Michelson; PRMi = the common motion of the arm cavities; and REFL2i = the common motion of the power recycled Michelson. The red and blue lines correspond to the locking accuracy threshold or RMS motion of a specific length degree of freedom. Beyond these thresholds, the respective servo fails. It is clear in that the servos remain stable throughout the operating region from -$5*10^{-5}$ diopters to $5*10^{-5}$ diopters. Through this region the amount of sideband power on the beamsplitter (SPOB) has two minima and three maxima. The minima at perfect mode matching, zero diopters, is due to the increasing number of modes contained within the PRM. Asymmetry in the SPOB around zero diopters is attributed to the asymmetries in the interferometer.

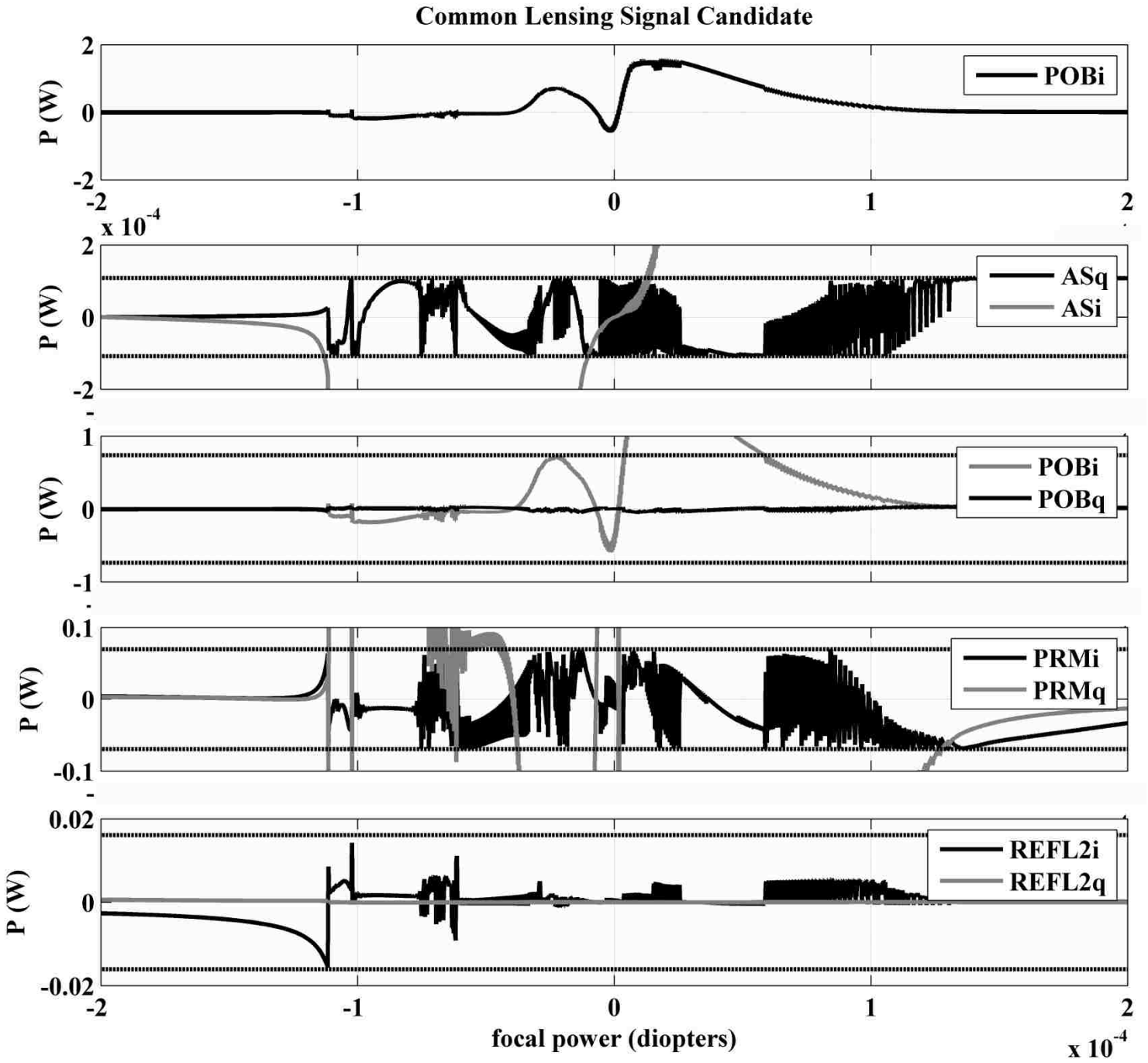

Figure 7-3: Common lensing signal candidate #2 and control signals. The top trace plots the behavior of beamsplitter pickoff light demodulated in-phase at 24.5 MHz (ASi) as a function of common focal power. In the following traces, the letters "i" and "q" refer to the demodulated phase quadrature. The zero crossing in POBi occurs at $\mathbf{1 \times 10^{-6}}$ diopters. This is below the simulation's resolution for arm power failure. If the interferometer is held on perfect mode matching, the POBi y-intercept is roughly -0.39 W. This assumes the demodulation is conducted without optical attenuation of the BS AR surface.

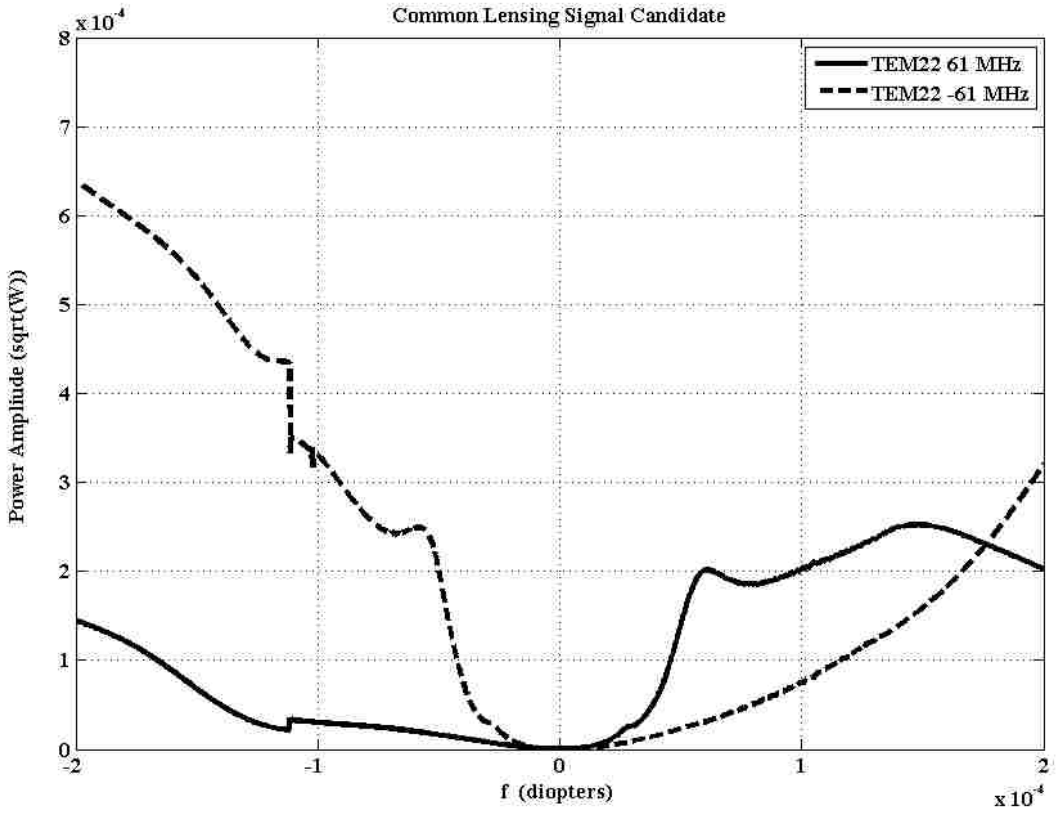

Figure 7-4: Common lensing simulation #3 is taken from the same simulation as the previous simulations. Traces represent the amplitude of the TEM_{22} mode of the POB light separated from the carrier by 61 MHz. The advantage of this signal is clear as the two sidebands cross at perfect mode matching. However, small amplitudes $10^{-4}\sqrt{W}$ imply the signal's lack of viability.

Signal #4

Differential lensing may be monitored using the beamsplitter pickoff light demodulated in quadrature phase with the 61 MHz RF (POB2q). Figure 7-5 shows the traces of this signal as a function of ITMx's focal power. Tuning the demodulation phase of the 61 MHz photodetector's mixer improves the response of the signal. The slope of the response from nearly flat around the point of perfect mode matching to $33.84\ \mathrm{W/diopter}$ when the differential lensing exceeds 2.5×10^{-5} diopters. A seemingly flat response around perfect mode matching is likely the result of the differential length servos performing their task. Small optical phase changes between the light fields returning from the arms to the beamsplitter can be interpreted as either differential thermal lensing or differential mirror displacement. Slopes build as the number of modes in the PRM increases. Higher order transverse modes lift power from the fundamental Gaussian modes reducing the power available for sensing. Like the common mode signals, this signal also has its difficulty. The PRM was designed to suppress the 61 MHz sidebands. The total amount of circulating power in the PRM was modeled to be milliwatts (with 1 W injected on the RM). This can be compared to the 37 W of carrier power with 1 W injected on the recycling mirror.

Although this may not be of academic concern, it is of practical concern. The anti-reflective surface of the beamsplitter would reduce overall beam intensity by 10^{-4}. Relay optics would reduce the power further. The ratio of 61 MHz sidebands to carrier would not change. However, the modulation's detectability would diminish beyond that of most available photodetectors.

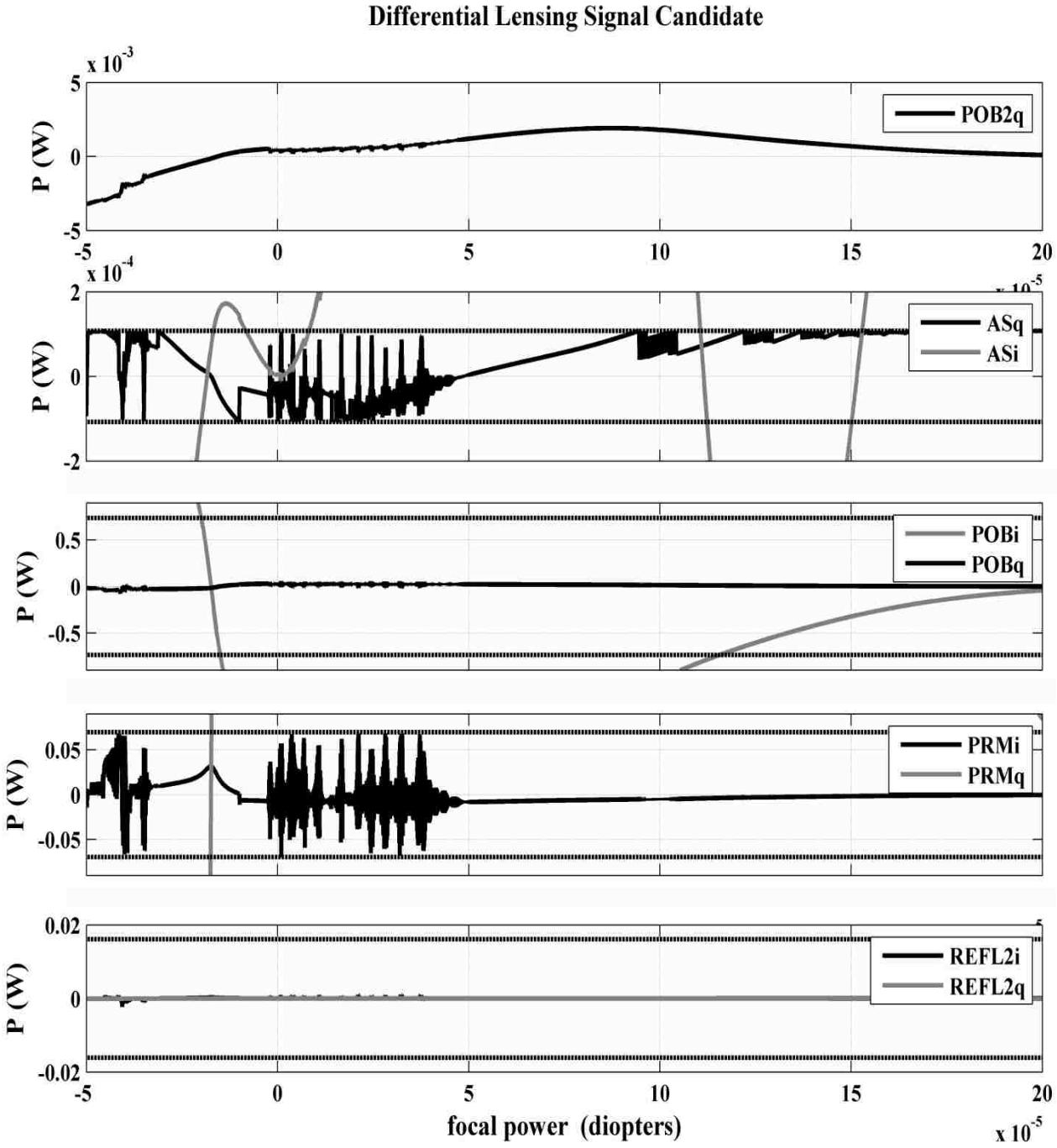

Figure 7-5: Differential lensing and control signals: The first trace shows the behavior of the beamsplitter pickoff light demodulated in the quadrature phase at 61 MHz. The signal reaches a slope of 33.84 W/diopter near $5*10^{-5}$ diopters. Somewhat flat behavior around perfect mode matching suggests that a servo may wander out to +/- $2*10^{-5}$ diopters. This wander is negligible since this is within the plateau of maximum arm power. The point of perfect mode matching is offset in these plots compared to the common mode plots.

7.3 Controlling the Thermal Lensing

The focus discriminants presented form a combination of channels capable of monitoring ITM lensing without the installation of excessive amounts of hardware. Using these channels as error signals, one could now construct a linear servo to manage perturbations in the ITMs' thermal lensing. Simple servos that would be unconditionally stable and present a $1/\text{frequency}$ response would work only once the intereferometer is in the operating regime. In order for this to occur, the interferometer must be deliberately forced from it cold state of roughly -1×10^{-4} diopters to a point microdiopters from perfect mode matching. Otherwise the discriminants will point away from perfect mode matching. For the rest of the section, the TCS benches themselves are assumed to operate well within noise requirements of iLIGO and eLIGO.

To begin, the average level of motion in terms of the ITMs' focal lengths must be determined. This sets the high water mark that needs to be suppressed. Average motion in an ambient background is referred to as the root mean square (RMS) noise. The square root of the bandwidth limited integral of the sensor signal voltage noise, $v(f)$, divided by signal gain, dv/dD, squared yields RMS fluctuation. The signal gain converts sensor voltage into units that correspond with the degree of freedom.

$$D_{RMS} = \sqrt{\int_{f_1}^{f_2} df \left(v(f) \frac{dD}{dv} \right)^2}. \tag{7.8}$$

D_{RMS} represents the diopter RMS value.

The requirement to determine the voltage noise from simulation and/or archived S5 data can be allayed by using chapter 6's raw absorption measurement data. The ITM absorption experiment yielded time series frequency data in both a driven state as well as a quiescent state. During the quiescent state the interferometer ran at 1 W injected into the mode cleaner for an excess of 6 hours. Using the coarse approximation from equation 6.5, one can convert frequency evolution into focal length.

$$f_{thermal} = \frac{2\pi\kappa\omega^2}{\frac{dn}{dT}\left(\frac{7390}{7.5 \times 10^{-5}}\right)\left(\frac{\frac{df}{dt}}{f_0}\right)}. \tag{7.9}$$

From this time series data, a power spectral density (PSD) can be computed and integrated over the spectrum to yield focal power RMS noise for an ITM. For this exercise, the more absorptive ITMy was chosen. It was expected to respond more quickly to positive changes in thermal state. With respect to the coarse approximation's validity, it computes ITM absorption to nearly 0.5 ppm of the numbers obtained from chapter 6's fitting solutions.

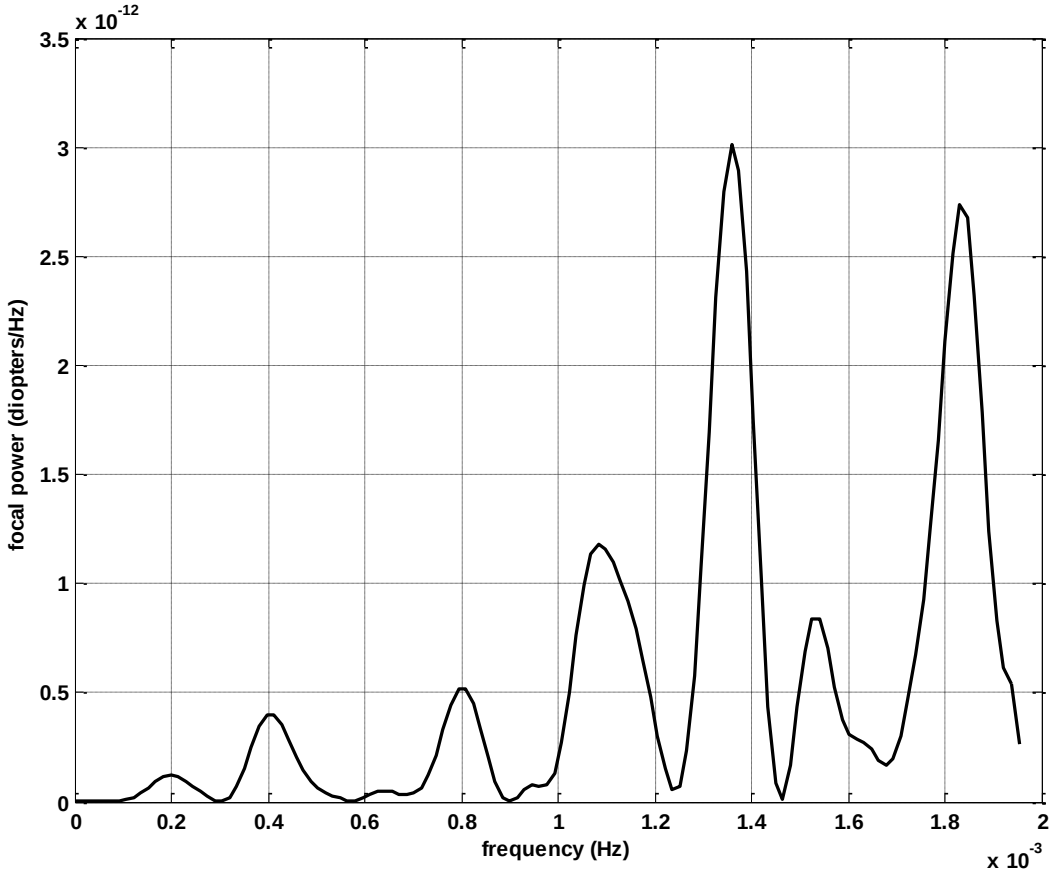

Figure 7-6: PSD of ITMY's thermal lens behavior during quiescent lock period on July 2008 data. The vertical axis presents power density in units of diopters per Hertz. The horizontal axis represents frequency out to 2 mHz.

The PSD for ITMy's thermal lens behavior during a quiescent lock is shown in Figure 7-6. The ordinate represents focal length in units of diopters. The abscissa represents frequency in millihertz. A set of dominant peaks can be seen at 1.4 and 1.8 mHz. The 1.8 mHz peak corresponds to the 10 minute heating time for the mirror coating. The pair of peaks around 1.4 mHz has not yet been identified but corresponds to a 710 second time constant.

The resulting RMS focal length from the above PSD equals approximately 3×10^{-8} diopters. Taking into consideration possible errors in computation, this level of RMS noise is too small to affect the interferometer's performance. With TCS disengaged, this number correlates to the DC and low frequency fluctuations in the main laser's intensity stabilization servo. This servo's performance in the Initial LIGO laser system (mid-2008) stabilized the relative intensity noise to $10^{-8}\ 1/\sqrt{\mathrm{Hz}}$ below 10 Hz . One can thereby surmise that the main laser intensity stabilization servo contributes the majority of quiescent noise. For LIGO Livingston, this was undoubtedly the reason Initial LIGO was able run TCS based on a table of settings.

Without the need for a servo in quiescent times, the only need for a servo occurs during power steps. Large power steps for both LIGO configurations take place during transitions between initial locking and operational power levels. These power steps can also occur when the detectors transition from a

reduced sensitivity to increased sensitivity or vice versa, for example during day/night mode switch. Without a suppression servo in place to tender to the mirrors' thermal profile, LIGO would require 30 minutes to 2 hours to improve its overall sensitivity. This delay between power transition and sensitivity was consistently observed during S5 [58].

7.4 Suggested TCS Operation

At the writing of this dissertation, the LIGO interferometers used two heating patterns in thermal compensation. The switch gate—a flipper mirror—changed the heating pattern in a few seconds. The logic for having either heating pattern permitted iLIGO to cope with either excessive or deficient lensing. The most important issue with the ITMs was the retention of their thermal gradients. Therefore, another operation state for TCS may be proposed.

In this new operational scheme, the ITMs are heated by both the central and annulus heating patterns. As the interferometers transition to a low power lock, the central heating pattern reduces in intensity to compensate. The central heating is reduced to compensate for the transition to LIG operational power. Throughout this time, the annular pattern is maintained at a constant level to retain the overall thermal profile. In this fashion, the ITMs are always optimized irrespective of power level. The singular drawback will be the upper limit for main laser power. The TCS heating patterns must first be tuned for maximum operating power.

7.5 Other Monitoring Schemes

Other means of monitoring thermal lensing in LIGO could be implemented with effort and introduction of new channels. One of these techniques, the Shack-Hartmann wavefront sensors, has already been mentioned. These sensors were being incorporated into the design of Advanced LIGO—the second generation variant of LIGO. Laser holography could be another means to monitor the thermal lenses of the ITMs. This would require a secondary laser to be directed onto a photodiode coaxial with the interferometer's AS light. As the secondary laser's frequency changes, higher order spatial modes and longitudinal frequencies would be resolved as intensity beats. A CCD with a low pass filter would ease the acquisition of spatial mode information. If a CCD is not available, a photodiode could also conduct the survey. The immediate drawback of this method is the introduction of the second precision laser. An extra light source risks backscatter directly into the interferometer. A third method of tracking the ITMs thermal lensing state would involve the introduction of a mode matched non-degenerate Fabry-Perot cavity. Continually measuring the POB or AS port fields would directly indicate the number of higher order modes circulating. As the interferometer approaches perfect mode matching, the number of higher order peaks will fall. This task would require an automated data acquisition and fitting routine to perform its task. This scheme also poses the risk of retroreflecting light if measures are not taken to isolate the scanning cavity. Another means of observing the lensing state of the ITMs and the field profile was discussed in J. Betzweiser's dissertation [50]. The complication with the phase camera would be its strength to detect average profiles of the sidebands. The phase camera at present cannot distinguish between upper and low phase modulated sidebands. This capacity would serve useful by if sideband balancing or differential lensing modes need to be studied. It also does not permit rapid decomposition of modal structure without some computational fitting routines. Nevertheless, several phase camera type sensors based at various pick off ports could feasibly detect differences in field

spatial profiles. Other approaches will be reserved for further study and future gravitational wave detectors.

8 Conclusions

The simulations detailed in this dissertation demonstrate the viability of a thermal model based only on the thermal behavior of the ITMs. It has been shown that sidebands imbalance in the LIGO detectors is attributable primarily to the topology of the detector. Absorption ratios of the mirrors were found be careful modeling and inclusion of the experiment hall (LVEA) temperatures. More over it has been demonstrated that absorption of the ITMs occurs mainly at the surface. This implies that the driving loss component of LIGO Livingston mirrors was caused by poor or contaminated coatings. The true evolution of the coating while in LIGO's vacuum chambers is indeterminate due to the lack of studies. This dissertation also demonstrated that the combination of thermal lens phase maps with A. Freise's FINESSE program yields results identifiable with interferograms and beam propagation patterns at LIGO Livingston and LIGO Hanford. Incidentally, phenomena relating TCS coupling to angular sensing and control can be simulated.

8.1 Further Research

Future improvements to the thermal model should by all means include absorption measurements for the four remaining mirrors. While the simulation algorithm remains the same, the overall fidelity of the simulation should be improved. Acquiring the other mirrors' absorption ratios would also add statistics to whether or not they share the coating absorption behavior found in the ITMs.

Finally, one would like to empirically determine the viability of the focus discriminants found. It would also be useful to estimate the level of improvement that LIGO would have observed during S5 and S6 if the ITMs had been correctly lensed.

One can make an educated guess based on the estimated range of the LIGO detectors to a 1.4:1.4 solar mass binary neutron star in-spiral recorded during scientific (astronomical) data collection. For the LIGO Livingston detector the estimated range over the S6 science run has varied between 12-13 Mpc. The majority of the estimated range values vary for each "science segment" (the time segments when astronomical data is collected). However, within individual segments the estimated range varies at the beginning. This variation or gradual rise in range takes place over 30-60 minutes in some cases. Recall the TCS stabilizes the interferometer behavior at non-design powers by supporting the ITM thermal lens.

Assuming that all scientific data segments spanning Sept 29, 2009 to March 31, 2010 were influenced strictly by improper TCS settings, than the majority (>60 %) of multi-hour science segments show a gradual change in range of the first 30-60 minutes of scientific data collection, see Figure 8-1.

Hanford shares the same type of transient behavior with the Livingston interferometer but for fewer science segments. The difference between Hanford's range transients and Livingston's range transients is the overall time. Estimated range transients lean towards the 30 minute mark. This may be induced by a variation in either TCS operating procedures or due to interferometer operators waiting longer periods of time before marking data as scientifically valuable.

Only a more detailed study will truly determine the attributes of correctly setting the TCS via the focus discriminants suggested.

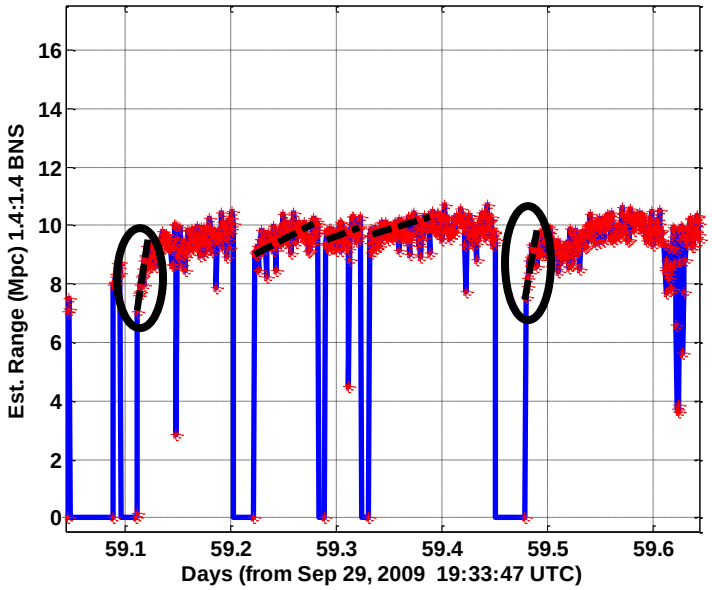

Figure 8-1: Data representing LIGO Livingston's estimated sensing range for 1.4:1.4 solar mass binary star in-spirals. The blue trace denotes datum steps. Red stars denote the beginning or end of science data collection segments including the differential datums between zero and operation. The black dashed lines indicate transients that may be induced by improper thermal lensing. Circled black dashed regions indicate typical start-up transients. These slow hour scale transients occur for most multi-hour science segments.

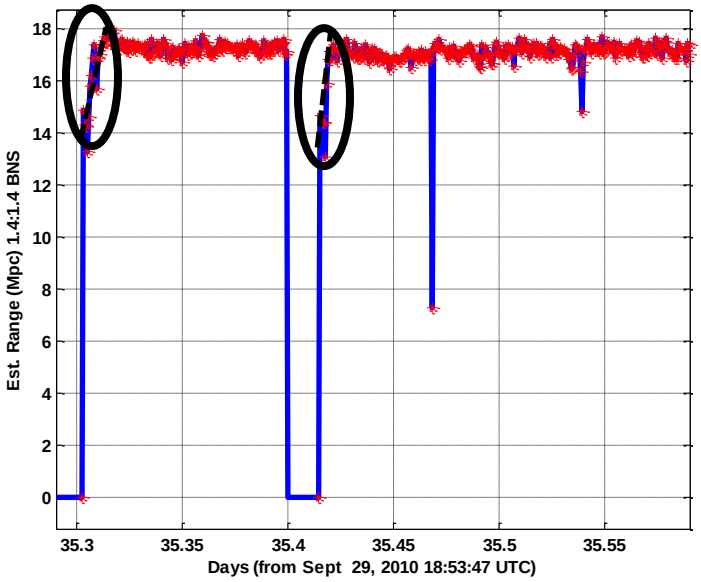

Figure 8-2: Data representing LIGO Hanford's estimated sensing range for 1.4:1.4 solar mass binary star in-spirals. The blue trace denotes datum steps. Red stars denote the beginning or end of science data collection segments including the differential datums between zero and operation. The black dashed lines indicate transients that may be induced by improper thermal lensing. Circled black dashed regions indicate typical start-up transients. These half hour scale transients occur for few science segment data segments.

Epilogue

During my time at LSU and at the LIGO Livingston Observatory, I have had a fantastic time. I have really enjoyed the company of my classmates, my professors, and the all too good tech crew at LIGO. With respect to LSU's Department of Physics and Astronomy, I only once before have seen such department wide enthusiasm for students and their interests. This was at my undergraduate institution, Florida Institute of Technology. It seemed quite plain at LSU that the professors were there to foster the achievement of the students as well as their successors. There were no clichés or group specific behavior. If you were remotely interested in a subject or just making friends, you were included—professor and student alike. This is something that other schools can learn from.

As for the LIGO, I have only one thing to tell the tech and administrative staff, it was real and it was fun. I got the chance to work at a national facility with good people; I got to travel and work at prestigious schools such as MIT and CIT. But most of all, the Livingston tech crew made it worthwhile to come in and hang out before getting some work done. The tech staff rarely had a miserable day and knew how to coax me to focus, without going out for a root beer. I honestly would have liked to work with this good a team until I retire, but change is for the better and for my good.

Mind you, I am also grateful for having met Rai Weiss. This guy is one those professors that everyone would like to have. A grandfatherly figure with the tongue of a sailor, he is able to speak on nearly every subject with ease. I will really miss working with him and for him. I just hope that he does not think that I am ignoramus as I am told.

As for my advisor, Joseph Giaime, sometimes I wish that CalTech would have given me more time to work with you instead of without you. In my electronic logbook I took the pen name "Spectre." This hails from the from a video game "MechWarrior IV" where I played the battle group "Spectre Lance"—The Ghost Battalion. Sometimes I really felt like I was on my own and without clear direction; sometimes I felt as though you had given me license for huge support, but every time it was from a distance. I know it is too much to ask a professor to check up on a student every few days. I retrospect it just toughened me. I am sure I could have learned more from you if I met you earlier. In the end, I hope Caltech loosens its restraints on your time; you are an advisor and mentor after all. And by the way, I hate simulations. Thanks for making me do this.

LIGO itself is a fantastic adventure and project for new students. Unfortunately the amount of background knowledge can easily overwhelm new students. I was fortunate to have met a couple of post docs and research scientists who helped me over this hurdle. However, I have all too often seen occasions where post-docs and induhviduals use this knowledge to taunt students. They do not feel it necessary to sit down and educate or understand. Rather they merely tell visitors how students must need to be to be baby sat. Confining information to a few key players ensures job security, but you aren't supposed to do that. Playing games at the expense of students' knowledge only gives students the idea that these induhviduals are conceited or scared. For me, I am glad I met the right people at the right time. People who helped me learn new things and gave me feedback on my own ideas. If LIGO is to succeed, false charity must be removed.

References

1. Smith, J., *The path to the enhanced and advanced LIGO gravitational-wave detectors.* arXiv:0902.0381v2 [gr-qc], 2009.

2. Saulson, P.R., *Fundamentals of Gravitational Wave Detectors*. 1994, Singapore: World Scientific.

3. Abbott, B.et al., *LIGO: The Laser Interferometer Gravitational-Wave Observatory.* Reports on Progress in Physics, July 2009. **72**(7).

4. Abbott, B.et al., *Detector Description and Performance for the First Coincidence Observations between LIGO and GEO.* Nuclear Instruments and Methods in Physics Research A, 2003. **517**(1-3): p. 154-179.

5. Adhikari, R., *Sensitivity and Noise Analysis of 4 km Laser Interferometric Gravitational Wave Antennae*. 2004, Massachusetts Institute of Technology (Dissertation).

6. Lawrence, R., *Active Wavefront Correction in Laser Interferometric Gravitational-wave Detectors*. 2003: Massachusetts Inst. of Technology (Dissertation).

7. Lawrence, R., M. Zucker, and P. Fritschel, *Active correction of thermal lensing through external radiative thermal actuation.* Optics Letters, 2004. **29**(22): p. 2635--2637.

8. Ballmer, S., et al., *Thermal Compensation System Description (LIGO DCC T050064-00-R)*. 2005.

9. Ballmer, S.W., *LIGO interferometer operating at design sensitivity with application to gravitational radiometry*. 2006, Massachusetts Inst. of Technology (Dissertation).

10. Gretarsson, A.M., et al., *Effects of mode degeneracy in the LIGO Livingston Observatory recycling cavity.* 2007. **24**(11): p. 2821-2828.

11. Smith, M., et al., *Heating Beam Pattern Optical Design CO2 Laser Thermal Compensation Bench (LIGO DCC T040057-01-D)*. 2004.

12. Zucker, M., D. Ottaway, and K. Mason, *Thermal Compensator Retrofit for LIGO 1 (LIGO-T030062-03-D)*, in *LIGO DCC*. 2003, CIT.

13. MacDonald, M.P., et al., *Reducing thermal lensing in diode-pumped laser rods.* Optics Communications, 2000: p. 383-393.

14. Mansell, J., et al., *Evaluating the effect of transmissve optics thermal lensing on laser beam quality with a Shack-Hartmann wave-front sensor.* Applied Optics, vol. 40, 2001: p. 366-370.
15. Fowles, G.R., *Modern Optics*. 1989, New York: Dover Publications.

16. Amin, R.S., *A Technique for Passively Compensating Thermally Induced Modal Distortions in Faraday Isolators for Gravitational Wave Detector Input Optics*. 2002, University of Florida: Gainesville.

17. Kittel, C., *Introduction to Solid State Physics*. 1996, New York: John Wiley and Sons, Inc.

18. Kogelnik, H. and T. Li, *Laser Beams and Resonators.* Applied Optics, 1966: p. 1550-1566.

19. Siegman, A.E., *Lasers*. 1986, Sausilito, CA: University Science Books.

20. Hodgson, N. and H. Weber, *Optical Resonators: Fundamentals, Advanced Concepts, and Applications*. 1997, London: Springer-Verlag.

21. Koechner, W., *Solid-State Laser Engineering, 6th Rev.* 2006, New York: Springer.

22. Svelto, O., *Principles of Lasers, 4th ed.* 1998, New York: Springer.

23. Mueller, G., et al., *Method for compensation of thermally induced modal distortions in the input optical components of gravitational wave interferometers.* J. Classical and Quantum Gravity, 2002: p. 1793-1801.

24. Davis, C.C., *Lasers and Electro-Optics: Fundamentals and Engineering*. 2000, Cambridge: Cambridge University Press.

25. Haus, H.A., *Waves and Fields in Optoelectronics*. 1984, Englewood Cliffs: Prentice-Hall.

26. Walther, A., *The Ray and Wave Theory of Lenses*. 1995, Cambridge: Cambridge University Press.

27. Thorne, K.S.e.a. *Gravitational Waves*. [course work and video] 2002 [cited 2008 May]; Available from: http://elmer.tapir.caltech.edu/ph237/.

28. Merzbacher, E., *Quantum Mechanics, 3rd ed.* 1998, New York: John Wiley & Sons, Inc.

29. Hello, P., Vinet, Jean-Yves, *Analytical models of thermal aberrations in massive mirrors heated by high power laser beams.* J. Physique France, 1990. **51**: p. 1267-1282.

30. COMSOL, *COMSOL Multiphysics*. 1998-2008, COMSOL AB: Burlington, MA (URL: http://www.comsol.com).

31. Mathworks., *MATLAB*. 2007, The Mathworks Inc. (URL: http://www.mathworks.com/).

32. A. Freise, et al., *Frequency domain interferometer simulations with higher-order spatial modes.* Classical and Quantum Gravity, 2004. **21**(5): p. S1067-S1074.

33. Freise, A., *Frequency domain INterferomEter Simulation SoftwarE v.0.99.8* <*http://www.gwoptics.org/finesse/*> 2009: Birmingham, U.K.

34. K.S. Kundert and A. Sangiovanni-Vincentelli. *SparseA Sparse Linear Equation Solver, University of California, Berkeley*. www.netlib.org 1988 [cited 2010 Jan. 25].

35. Davis, T.A., *CSparse, CXSparse, KLU, and BTF: Direct Methods for Sparse Linear Systems.* SIAM, 2006.

36. Bayer-Helms, F., *Coupling coefficients of an incident wave and the modes of a spherical optical resonator in the case of mismatching.* Applied Optics, 1984. **23**(9): p. 1369-1380.

37. Hello, P., Vinet, Jean-Yves, *Analytical models of transient thermoelastic deformatios of mirrors heated by high powercw laser beams.* 1990. **51**(20): p. 2243-2261.

38. Coyne, D. *Test Mass Modes*. 2000 [cited 2008 Sept 25]; Available from: http://www.ligo.caltech.edu/~coyne/IL/COC/TM_modes/TM_modes.html.

39. Yamamoto, H., *SIS (Stationary Interferometer Simulation) manual (LIGO DCC T070039-v1)*, in *LIGO DCC*. Dec. 2008, California Institute of Technology.

40. Rakhmanov, M., *Dynamics of Laser Interferometric Gravitational Wave Detectors*. 2000, California Institute of Technology (Dissertation). p. 271.

41. R. W. P. Drever, et al., *Laser Phase and Frequency Stabilization Using an Optical Resonator.* Applied Physics B, 1983. **31**: p. 97-105.

42. Black, E., *Notes on Pound-Drever-Hall technique (LIGO DCC T980045- 00-D)*. 1998, California Institute of Tehchnology.

43. Yamamoto, H., *Personal communication during March LVC 2009 meeting*. 2009: Arcadia, CA.

44. D'Ambrosio, E. and W. Kells, *Carrier mode selective working point and side band imbalance in LIGO I.* Physical Review D, 2006. **73**(122002).

45. Strain, K.A., et al., *Thermal lensing in recycling interferometric gravitational wave detectors.* Physics Letters A, 1994. **194**(1-2): p. 124-132.

46. Winkler, W., et al., *Heating by optical absorption and the performance of interferometric gravitational-wave detectors.* Physical Review A, 1991: p. 7022-7036.

47. Willems, P. p.c., *Re: Empirical fitting of fused silica's Young's modulus and Poisson ratio using EGO group data*. 2008.

48. Willems, P. *Analysis of the ETM frequency shifts*. 2007 [cited 2008 June 17]; Available from: http://ilog.ligo-la.caltech.edu/ilog/pub/ilog.cgi?group=detector&date_to_view=02/11/2007&anchor_to_scroll_to=2007:02:12:08:12:22-willems.

49. Willems, P. *The TCS-induced frequency drifts are about what they should be*. 2007 [cited 2008 June 17]; Available from: http://ilog.ligo-la.caltech.edu/ilog/pub/ilog.cgi?group=detector&date_to_view=02/11/2007&anchor_to_scroll_to=2007:02:12:03:16:04-willems.

50. Betzwieser, J., *Analysis of spatial mode sensitivity of a gravitational wave interferometer and a targeted search for gravitational radiation from the Crab pulsar*. 2007, Massachusetts Institute of Technology (Dissertation).

51. Gretarsson, A.M. *Report on Power Increase Work*. 2004 [cited 2009 November]; Available from: http://ilog.ligo-la.caltech.edu/ilog/pub/ilog.cgi?group=detector&date_to_view=01/22/2004&anchor_to_scroll_to=2004:01:22:05:43:29-andri.

52. Gretarsson, A.M., et al., *Effects of mode degeneracy in the LIGO Livingston Observatory recycling cavity.* J. Opt. Soc. Am. B, 2007. **24**(11): p. 2821-2828.

53. Mavalvala, N., *Alignment Issues in Laser Interferometric Gravitational-Wave Detectors*. 1997, Massachesetts Institute of Technology (Dissertation).

54. Willems, P., *TCS Weekly Teleconference: Discussion regarding TCS induced tilt*. Dec. 9, 2008.

55. Mueller, G., et al., *Determination and optimization of mode matching into optical cavities by heterodyne detection.* Optics Letters, 2000. **25**(4): p. 266--268.

56. Dooley, K. *Studying effect of TCS on full ifo lock*. 2009 [cited 2009 March 16, 2010]; Available from: http://ilog.ligo-la.caltech.edu/ilog/pub/ilog.cgi?group=detector&date_to_view=04/02/2009&anchor_to_scroll_to=2009:04:02:03:45:07-kate.

57. Dooley, K. *Working towards high power DC locking*. 2009; Available from: http://ilog.ligo-la.caltech.edu/ilog/pub/ilog.cgi?group=detector&date_to_view=04/05/2009&anchor_to_scroll_to=2009:04:05:06:03:09-kate.

58. Johnson, W., *Personal Communiqué: Glitch rates during start of science times*, R. Amin, Editor. 2009: Baton Rouge.

59. Adhikari, R., et al., *Input Optics Final Design (LIGO DCC T980009-01-D)*. 1998, University of Florida.

60. Adhikari, R., et al., *Input Optics Preliminary Design (LIGO DCC T970144-00-D).* 1997.

Appendix A.

The Gaussian Beam Parameter

Gaussian beams possess a few characteristics [19]. The first is a Gaussian electric field amplitude across the entire wavefront. The second characteristic is one-half the collimation distance, called Rayleigh range, z_R.

$$z_R = \frac{\pi\omega_0^2}{\lambda}.$$

A.1

Here
ω_0 = the beam waist, the narrowest beam radius in a region defined by a particular beam parameter;
$\lambda =$ optical wavelength.
Related to the Rayleigh range is the expansion of the beam radius as a function of propagated distance from the beam waist location.

$$\omega(z) = \omega_0\sqrt{1 + \left(\frac{z - z_0}{z_R}\right)^2}.$$

A.2

There $z_0$equals the beam waist location. At z_R from the a Gaussian beam's waist, the beam radius increases by $\sqrt{2}$. The final characteristic is the nature of the radius of curvature, R_C, of a Gaussian beam's wavefront as a function of distance from the waist.

$$R_C = z - z_0 + \frac{z_R^2}{z - z_0}.$$

A.3

For Gaussian beams, the radius of curvature equals infinity at the waist and at infinite distance. At the z_R, the radius of curvature reaches a global minimum.

Combining these terms, any Gaussian laser beam can be represented by a single value called the Gaussian beam parameter, q. Anywhere along a beamline, the beam parameter is defined as follows:

$$\frac{1}{q(z)} = \frac{1}{R_z(z)} - \frac{i\lambda}{\pi\omega^2(z)}.$$

A.4

At the reference plane, $z = 0$, the beam parameter reduces to the Rayleigh range, z_R times i.

$$q_0 = iz_R = \frac{i\pi\omega_0^2}{\lambda}.$$

A.5

Using the beam parameter, Gaussian transverse field distributions can be written as follows [19]:

$$u(x,y,z) = \frac{1}{q(z)} e^{-\frac{ik\left(x^2+y^2\right)}{q(z)}}.$$

A.6

Higher order mode solutions can be written as using this notation [19]. Below is an equation for a single transverse mode dimension.

$$u_n(x,z) = c_n \left(\frac{2}{\pi}\right)^{\frac{1}{4}} \left(\frac{1}{2^n n!\,\omega_0}\right)^{\frac{1}{2}} \left(\frac{q_0}{q(z)}\right)^{\frac{1}{2}} \left(\frac{q_0}{{q_0}^*}\frac{q^*(z)}{q(z)}\right)^{\frac{2n+1}{4}} H_n\left(\frac{\sqrt{2}x}{\omega(z)}\right) exp\left[\frac{-ikx^2}{2q(z)}\right].$$

A.7

Here
c_n = weighting coefficient;
n = one dimensional transverse mode number;
H_n = normalized Hermite polynomial;
k = optical wave number.
To represent a proper two dimensional Hermite-Gauss distribution, a second similar higher order mode set for the y-axis is simply multiplied through.

$$u_{nm}(x,y,z) = u_n(x,z)u_m(y,z).$$

A.8

As the beam is propagated using Gaussian ABCD techniques shown in chapter 5, the waist and radius of curvature can be represented using the propagated beam parameter respectively.

$$\omega^2(z) = \frac{\lambda}{\pi}\frac{|q|^2}{\mathrm{Im}(q)}.$$

A.9

$$R_C(z) = \frac{|q|^2}{\mathrm{Re}(q)}.$$

A.10

Appendix B. FINESSE

The following is a summary of four FINESSE local scattering matrices alluded to in chapter 4. FINESSE treats each optic as a scattering matrix in order to solve how fields travel through an optical layout. These matrices are written for plane wave relations [33].

B.1.1 Space

The space component simply adds a phase a phase shift to the light fields passing through

$$\begin{pmatrix} Out_1 \\ Out_2 \end{pmatrix} = \begin{pmatrix} 0 & s_1 \\ s_2 & 0 \end{pmatrix} \begin{pmatrix} In_1 \\ In_2 \end{pmatrix}$$

The variables s_1 and s_2 are equal to the difference in offset frequency, Δf.

$$s_1 = s_2 = e^{-\frac{i2\pi fnL}{c}} = e^{-\frac{i2\pi (f_0 - \Delta f)nL}{c}} = e^{-\frac{i2\pi (\Delta f)nL}{c}}.$$

This is due to the macro-lengths in FINESSE are always assumed to be in resonance unless otherwise noted. Here the default frequency, f_0, is encoded to be 1064 nm for this dissertation.

B.1.2 Beamsplitter

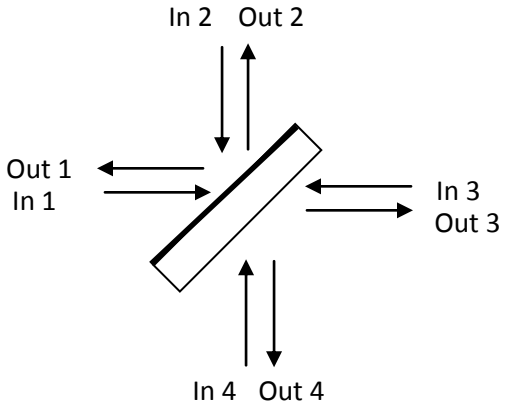

Figure B-1: Illustration of beamsplitter formalism. The bold line indicates the reflective surface. The numbers represent connecting nodes for a beamsplitter.

Since one has 4 input ports and 4 output ports, the field amplitudes are connected by writing the input and output fields as shown.

$$\begin{pmatrix} \text{Out1} \\ \text{Out2} \\ \text{Out3} \\ \text{Out4} \end{pmatrix} = \begin{pmatrix} 0 & b21 & b31 & 0 \\ b12 & 0 & 0 & b42 \\ b13 & 0 & 0 & b43 \\ 0 & b24 & b34 & 0 \end{pmatrix} \begin{pmatrix} \text{In1} \\ \text{In2} \\ \text{In3} \\ \text{In4} \end{pmatrix}$$

Now it is rather simple to see how sources can be linearly connected to their pending output ports. For the matrix,

$b_{12} = b_{21} = re^{\frac{i2\phi\omega}{\omega_0}cos(\alpha)}$;

$b_{13} = b_{31} = it$;

$b_{24} = b_{42} = it$;

$b_{34} = b_{43} = re^{-\frac{i2\phi\omega}{\omega_0}cos(\alpha)}$.

Here:
ϕ = user inflicted subwavelength position tuning (in radians);
r = amplitude reflectivity;
t = amplitude transmissivity;
f = beam optical frequency plus any offsets;
f_0 = incident beam optical center (carrier) frequency;
α = angle of incidence with respect to node 1;
i = square root of -1.

B.1.3 Mirror

A mirror only requires two nodes. In reality, a tilted mirror is a beamsplitter. In simulation, a mirror and a beamsplitter are distinctly separate objects. All mirrors in FINESSE are represented as ideal thin mirrors. Practical mirror models must be ganged with other mirrors spaces possessing indices of refraction greater than 1. The mirror's reflection coefficients change the incident field's amplitudes and phases for reflection and transmission, respectively.

$$E_{refl} = re^{(i\varphi)}E_{in}.$$

$$E_{trans} = itE_{in}.$$

Where:
r = amplitude reflectivity;
t = amplitude transmissivity;
φ = phase shift acquired on reflection from a mirror with micro-tuning lengths invoked (radians);
i = square root of -1.
E_{in} = incident electric field.

The scattering matrix for a mirror is shown below. The associated numbers indicate node positions.

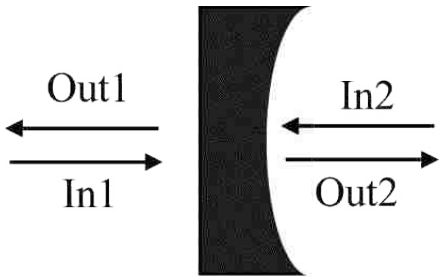

Figure B-2: An illustration of beamsplitter formalism. The mirror is treated as a thin mirror. The numbers represent connecting nodes for a mirror.

$$\begin{pmatrix} Out_1 \\ Out_2 \end{pmatrix} = \begin{pmatrix} m_{11} & m_{12} \\ m_{21} & m_{22} \end{pmatrix} \begin{pmatrix} In_1 \\ In_2 \end{pmatrix}.$$

$m_{12} = m_{21} = it$

$m_{11} = re^{i2\phi\frac{f}{f_0}}.$

$m_{22} = re^{-i2\phi\frac{f}{f_0}}.$

Where:

r = amplitude reflectivity;

t = amplitude transmissivity;

f = beam optical frequency plus any offsets;

f_0 = incident beam optical center (carrier) frequency;

i = square root of -1.

The ϕ relates to the microscopic length tuning as invoked by the user.

B.1.4 Lens

A thin lens does not scatter light, nor does it add phase.

$$\begin{pmatrix} Out_1 \\ Out_2 \end{pmatrix} = \begin{pmatrix} 0 & 1 \\ 1 & 0 \end{pmatrix} \begin{pmatrix} In_1 \\ In_2 \end{pmatrix}.$$

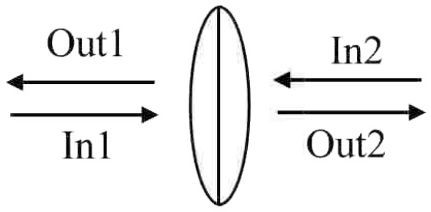

Figure B-3: An illustration of a lens scattering matrix.

Appendix C. Derivation of the ASi

Begin with the simple plane wave solution noted in equation 5.6.

$$E_{in} = E_0 e^{i\omega t} \sum_k i^k J_k(\Gamma) e^{ik\Omega t}.$$

Let's now expound on the solution final solutions by first writing the DC field using the Hermite-Gauss basis.

$$E^* \cdot E = \sum_{ij} \sum_{nm} \sum_{n'm'} \left(\begin{matrix} c_{nm}\, c_{n'm'} (2^{n+m+1} n!\, m!\, \pi)^{\frac{-1}{2}} \left(2^{n'+m'+1} n'!\, m'!\, \pi\right)^{\frac{-1}{2}} \left(\frac{1}{\omega(z)}\right)^2 e^{i\left((n+m+1)\Psi(z) - (n'+m'+1)\Psi(z)\right)} \times \\ H_n\left(\frac{\sqrt{2}}{\omega(z)}\right) H_m\left(\frac{\sqrt{2}}{\omega(z)}\right) H_{n'}\left(\frac{\sqrt{2}}{\omega(z)}\right) H_{m'}\left(\frac{\sqrt{2}}{\omega(z)}\right) e^{\frac{-ik(x^2+y^2)}{2R(z)} - \frac{x^2+y^2}{\omega^2(z)} + i\frac{k(x^2+y^2)}{2R(z)} - \frac{x^2+y^2}{\omega^2(z)}} e^{i(\omega_i - \omega_j)t} \end{matrix} \right). \quad \text{C.1}$$

where n, m are spatial mode numbers, c_{nm} refers to the amplitude weighting coefficient for each Gaussian spatial mode, H is the Hermite polynomial, $\omega(z)$ is the spot size as a function of axial position, k is the wave number, $\Psi(z)$ is the Gouy shift, and the indexed ω's are the longitudinal frequencies of the fields being multiplied. The demodulated signal, S_1 can be written as follows:

$$S_1 = \frac{1}{2}\left[\sum_{ij} \sum_{nm} \sum_{n'm'} \left(\begin{matrix} c_{nm}\, c_{n'm'} (2^{n+m+1} n!\, m!\, \pi)^{\frac{-1}{2}} \left(2^{n'+m'+1} n'!\, m'!\, \pi\right)^{\frac{-1}{2}} \left(\frac{1}{\omega(z)}\right)^2 e^{i\left((n+m+1)\Psi(z) - (n'+m'+1)\Psi(z)\right)} \times \\ H_n\left(\frac{\sqrt{2}}{\omega(z)}\right) H_m\left(\frac{\sqrt{2}}{\omega(z)}\right) H_{n'}\left(\frac{\sqrt{2}}{\omega(z)}\right) H_{m'}\left(\frac{\sqrt{2}}{\omega(z)}\right) e^{\frac{-ik(x^2+y^2)}{2R(z)} - \frac{x^2+y^2}{\omega^2(z)} + i\frac{k(x^2+y^2)}{2R(z)} - \frac{x^2+y^2}{\omega^2(z)}} e^{i(\omega_i - \omega_j)t} \end{matrix} \right) \right] \cdot \left(e^{i(\omega_{loc} t + \phi_{loc})} + e^{-i(\omega_{loc} t + \phi_{loc})}\right) \quad \text{C.2}$$

This penultimately turns into the demodulated signal C.3.

$$S_{1,DC} = Re \cdot \left(\sum_{ij} \sum_{nm} \sum_{n'm'} \left(\begin{matrix} c_{nm}\, c_{n'm'} (2^{n+m+1} n!\, m!\, \pi)^{\frac{-1}{2}} \left(2^{n'+m'+1} n'!\, m'!\, \pi\right)^{\frac{-1}{2}} \left(\frac{1}{\omega(z)}\right)^2 e^{i\left((n+m+1)\Psi(z) - (n'+m'+1)\Psi'(z)\right)} \times \\ H_n\left(\frac{\sqrt{2}}{\omega(z)}\right) H_m\left(\frac{\sqrt{2}}{\omega(z)}\right) H_{n'}\left(\frac{\sqrt{2}}{\omega(z)}\right) H_{m'}\left(\frac{\sqrt{2}}{\omega(z)}\right) e^{\frac{-ik(x^2+y^2)}{2R(z)} - \frac{x^2+y^2}{\omega^2(z)} + i\frac{k(x^2+y^2)}{2R(z)} - \frac{x^2+y^2}{\omega^2(z)}} e^{i(\omega_i - \omega_j)t} \end{matrix} \right) \right) \quad \text{C.3}$$

One can observe from the complication of spatial terms that the magnitude of the sideband field is not the only important issue. It is necessary also that they overlap correctly in modal space. This means that higher order modes in the power recycling cavity result in DC offsets and spatially resolved beats at the anti-symmetric port.

Appendix D. Similarity of Thermal Lensing to Mirror Displacement

Most results in this dissertation refer to the effects of higher order modes complicating interferometer behavior. For example, the generation of the ASi signal or the PRM instability is voiced starting from chapter 1. Around perfect mode matching, an analytical solution can be rendered. This transfer function relates only optical behavior at the beamsplitter AR surface; length control servo response is not included.

$$T_{00}(k) = \frac{E_{circ}}{E_0} = \frac{t_{RM} t_{BS} e^{\frac{i}{2}\phi_{prop\ ,r}}}{1 - r_{RM} r_{ITMx} t_{BS}^2 e^{i\phi_{prop\ ,x} + \frac{i2\pi}{\lambda}\Delta OPL_x} - r_{RM} r_{ITMy} r_{BS}^2 e^{i\phi_{prop\ ,y} + \frac{i2\pi}{\lambda}\Delta OPL_x}} \quad \text{D.1}$$

$$\phi_{prop\ ,(x,y)} = 2k\left(l_c + l_{(x,y)}\right) + 2\pi\left(\frac{m+n}{\pi} arccos\sqrt{g}\right) \quad \text{D.2}$$

$$\Delta OPL_{(x,y)} = 2k\left(\frac{\omega^2}{2}\left(\frac{1}{f_{(x,y)}} - \frac{2}{\rho_{(x,y)}}\right)\right) \quad \text{D.3}$$

where:
$T_{00}(k)$: amplitude transfer function;
E_{circ}: circulating electric field;
E_0: Input electric field;
λ: optical wavelength;
k: axial wave number
ω: beam spot size;
m, n: mode numbers in Hermite-Gauss basis;
t_{RM}; amplitude transmission coefficient of the RM mirror;
t_{BS}: amplitude transmission coefficient of the BS mirror;
$\phi_{prop\ (x,y)}$: propagation phase corresponding x- or y-ITM;
r_{RM}: amplitude reflection coefficient of the RM;
$r_{ITMx,y}$: amplitude reflection coefficient of the ITMx or ITMy respectively;
t_{BS}: amplitude transmission coefficient of the beamsplitter;
$\Delta OPL_{(x,y)}$: change in optical path length due to ITMx or ITMy's lens respectively;
$f_{(x,y)}$: focal length of ITMx or ITMy respectively;
$\rho_{(x,y)}$: radius of curvature of ITMx or ITMy respectively;
$l_{(x,y)}$: geometric length from the BS to corresponding x- or y-ITM;
l_c: geometric length from the RM to the BS;
g: cavity stability parameter.

An average cavity stability parameter, g, between the ITMs and the recycling mirror is assumed. The ITMs are allowed to have identical reflectivity as in reality. This simplifies separation of variables.

$$T_{00}(k) = \frac{t_{RM} t_{BS} e^{ikl_c}}{1 - r_{RM} r_{ITM} r_{BS}^2 e^{i2kl_c} e^{ik(l_x+l_y)} e^{i(\xi_x+\xi_y)} \cos\left(k(l_x - l_y) + (\xi_x - \xi_y)\right)}$$

D.4

Here $\xi_x = k\left(\frac{1}{f_x} - \frac{2}{\rho_x}\right)\frac{\omega^2}{2}$, and $\xi_y = k\left(\frac{1}{f_y} - \frac{2}{\rho_y}\right)\frac{\omega^2}{2}$. This description suitably denotes how both differential lensing and common mode lensing affect the circulating fields at the beamsplitter pickoff. This transfer function can be extended to higher order TEM modes as shown in equation D.5 without considering the complications of excessive lensing.

$$T_{mn}(k) = \frac{t_{RM} t_{BS} e^{ikl_c} e^{\frac{i}{2} 2\pi\left(\frac{m+n}{\pi} arccos\sqrt{g}\right)}}{1 - r_{RM} r_{ITM} r_{BS}^2 e^{i2kl_c} e^{i\,2\pi\left(\frac{m+n}{\pi} arccos\sqrt{g}\right)} e^{ik(l_x+l_y)} e^{i(\xi_x+\xi_y)} \cos\left(k(l_x - l_y) + (\xi_x - \xi_y)\right)}$$

D.5

Appendix E.

Determining Mode Cleaner Effects

During the analysis of the sideband PRM sideband imbalance, the author's first approach was to determine if the sideband attenuation was caused by equipment upstream of the detector. Several thermally susceptible devices were installed in the IOO chain. The Faraday isolator and electro-optic modulators were refitted with equipment designed for the eLIGO PSL powers. However, the mode cleaner had not been altered. If thermal aberrations change the mode cleaner's transverse mode suppression, then the cavity's mode may change. This change would then alter the amount of both sidebands transmitted to the core optics. This appendix subsection estimates the level of thermal aberration induced in the suspended mode cleaner.

The practical solution was fairly straightforward. The model was similarly simple to analyze. Physical characteristics of the cold interferometer mode cleaners can be found in numerous dissertations [5, 9, 59]. At eLIGO power levels, circulating power had been expected to cross 10^4 W. This was in excess of arm cavity gain. Table E-1 shows physical parameters of the mode cleaner as specified by the University of Florida in their LIGO technical document LIGO-T970144-00D and T980009-01-D [59, 60].

Table E-1: Optical parameters of the LIGO suspended mode cleaner.

Parameter Name	Value	Error Margin
Mirror material	Fused SiO_2	
Plane mirror transmittance	0.002	+/- 100ppm
Plane mirror reflectance	0.998	+/- 100ppm
Curved mirror transmittance	$1 \cdot 10^{-5}$	+0, -10ppm
Rear surface AR coating	>99.8%	+0.2%,-0
Mirror absorbance/scattering each	<0.00010	
Finesse	1550	
Free spectral range	12.246 MHz	
Cavity full width/half max	7.83 kHz	
Cavity full width/half max	0.342 nm	
Cavity optical half-length	12240 mm	
Curved mirror radius of curvature	17250 mm	+250,-350 mm
Cavity Stability Parameter, g	0.290	
Waist size	1.629 mm	
Raleigh range	7.83 m	
Beam divergence	208 μrad	
1 ppm intensity, curved mirror	15.9 mm	
100 ppm intensity, curved mirror	13.0 mm	

To be conservative, let us assume thermal conductivity, κ, is high and emissivity approximately approaches unity. With the specifications above, one can estimate the lower bound time for mode cleaner mirrors take to reach thermal equilibrium.

$$\frac{\Delta T}{< P_a >} = \frac{1}{4\eta A\sigma T_0^3}$$

$$\approx \frac{1}{4 \cdot 1 \cdot 0.0206\, m^2 \cdot \left(5.67 \cdot 10^{-8} \frac{\mathrm{W}}{\mathrm{m^2 K^4}}\right)^3}$$

$$\approx 7.9273 \frac{\mathrm{K}}{\mathrm{W}}.$$

E.1

$$T_{equilibrium} = M_{optic}\, C_{optic}\, \frac{\Delta T}{< P_a >}$$

$$\approx (0.243\ kg)\left(745 \frac{\mathrm{J}}{\mathrm{kg\ K}}\right)\left(7.9273 \frac{\mathrm{K}}{\mathrm{W}}\right)$$

$$\approx 0.4\ \mathrm{hrs}$$

E.2

where:
ΔT : change in temperature,
A : surface area,
$< P_a >$: absorbed power,
η : radiation absorption efficiency,
σ : Stefan-Boltzmann's constant,
T_0 : initial temperature,
M_{optic} : small optic mass,
C_{optic} : small optic heat capacity.

Because the high intensity light only sees the highly reflective coating of the mirrors, thermal lensing is not an issue. The surface expansion according to a COMSOL based finite element model yields approximately 2 nm for 987 W of circulating light. Here the absorption is assumed to be in the coating.

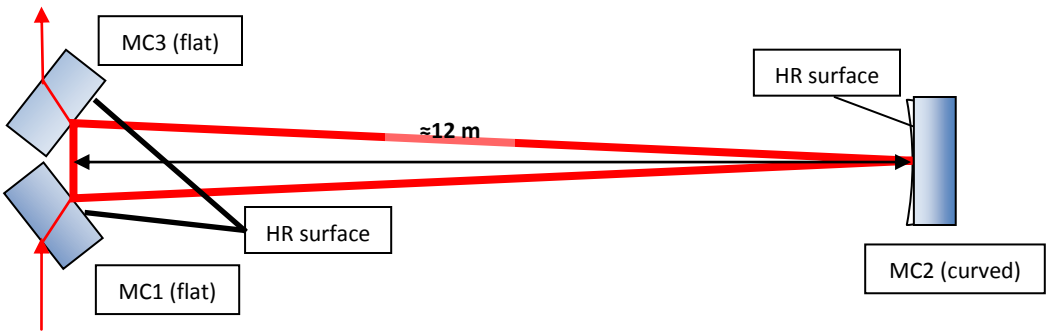

Figure E-1: Diagram of the suspended 12 meter mode cleaner. MC1 serves as the input coupler. MC3 serves as the output coupler. MC2 is the only curved mirror. This apparatus serves as the primary spatial mode filter and the final low pass intensity noise filter before the interferometer. Primary attention is paid to the curved mirror due to the specular effects observed under out of vacuum

The curvature of the curved mirror changes as shown below using the basic Hello-Vinet approximation [46] and [37].

$$\alpha = 5.5 \cdot 10^{-7}.$$
$$\beta \sim 10^{-5}\frac{1}{\mathrm{K}}.$$
$$\kappa = 1.38\frac{\mathrm{W}}{\mathrm{m\,K}}.$$

Sagitta can be computed as spot size squared divided by twice the radius of curvature.

Again the audience is reminded that absorbed power can be written as $P \approx KA\Delta T \approx 2\pi\kappa{\omega_m}^2\frac{\delta T}{\omega_m}$.

$$\delta s \approx \alpha\omega_m\frac{\delta T}{2},$$
$$\approx \frac{\alpha}{4\pi\kappa}P_a.$$

E.3

Roughly the spot size gives a sagitta of 65.2 nm. The change in sagitta results in the following power dependent equation.

$$\delta s \approx \frac{5.5 \cdot 10^{-7}}{4\pi \cdot 1.38\frac{\mathrm{W}}{\mathrm{m\,K}}}P_a.$$

E.4

Now we determine the level of absorbed power. The effective number of round trips can be estimated from the cavity finesse, $\mathcal{F}$ [45].

$$N_{eff} \approx \frac{2\mathcal{F}}{\pi}$$
$$\approx 987.$$

E.5

Table E-2: A table of injected powers, corresponding circulating powers, absorbed power, and the corresponding curvature change to mode cleaner mirror MC2.

P_{in} (W)	P_{circ} (W)	P_a (W)	δs (m)
1	986.76	0.098676	$3.13\cdot10^{-9}$
10	9867.6	0.98676	$3.13\cdot10^{-8}$
15	14801.4	1.48014	$4.70\cdot10^{-8}$
20	19735.2	1.97352	$6.26\cdot10^{-8}$

More recent finesse measurements yields an estimated 868 roundtrips. The direction of this result only reduces the total circulating power. Ultimately the result is so small that we should not notice a

significant change in either the beam parameters or the filtering characteristics. Measurements made by the University of Florida input optics group show no measurable change in the beam parameters. Analytical changes in the sagitta are noted in Table E-2.

Analytical approximations indicated a 3 % change in sideband strength. Measurements were made using a degenerate optical spectrum analyzer in January 2009. Actual values indicated between a 6 % and 8 % change between 1 W injected and 26 W injected. This would imply that the flat mirrors would have also been involved thermal expansion or the curved mirror presented a greater coating absorption than suspected. Adding these mirrors should bracket the actual measurements with an upper limit.

Vita

Rupal Shashikant Amin was born in Leeds, England, in May 1977. His parents soon relocated to the northeastern U.S. During his childhood, Rupal's father taught him about different methods of looking at the world. Although this was biased towards chemistry, Rupal's father let him enter the fields of engineering. Rupal entered Florida Institute of Technology's aerospace engineering program in 1995. Two years later, he transferred to the physics department and never looked back. There he found his first three advisors, Ryne Raffaelle (now at Rochester Institute of Tech.), Hamid Rassoul (Fl Tech), and Mark Moldwin (now at UCLA). These three professors wasted no time in showing Rupal how research was conducted, and how original thinking helped advance science in general. They guided him down a path of numerical analysis and experiment. Classes at NASA and projects with the space program also cultivated a ideal of "the sky's not the limit."

After graduating from Florida Tech, Rupal entered University of Florida's graduate program. A difficult first year suddenly showed Rupal that physics was not for the faint of heart. Professors David B. Tanner and David Reitze accepted Rupal as their graduate student in the LIGO laborartory at the University of Florida. Under the direction of Guido Müller, he learned the art of precision laser experiments. These experiments ended in a master's thesis, presentations, and eventually employment at the LIGO Livingston Observatory. (He was charged with aiding the commissioning crew and setting up the high power laser lab.)

While at the observatory, Rupal re-entered graduate school under the advisement of Joseph Giaime. This was an honest effort to obtain better employment and take care of his family. It was also a promise to himself to achieve a doctorate, something missed at the University of Florida.

For the past four years, Rupal has been in earnest trying to obtain a doctorate. Honestly, Rupal also thought such a task could be done sooner as he had already received his master's degree from the University of Florida. Following two previous experiments, Rupal was given the chance to work with the thermal compensation group, TCS. This was a chance he relished as he already knew of Phil Willems and was colleagues with Aidan Brooks. His time in the group and at the LIGO Livingston detector has culminated in this dissertation as well as a paper submitted to the Journal of Classical and Quantum Gravity.